

# Analysis of Quench Detection and Protection of a Nb<sub>3</sub>Sn CCT Technology Demonstrator Dipole for FCC

Présentée le 23 juillet 2020

à la Faculté des sciences de base  
Laboratoire de physique des réacteurs et de comportement des systèmes  
Programme doctoral en énergie

pour l'obtention du grade de Docteur ès Sciences

par

**Jiani GAO**

Acceptée sur proposition du jury

Dr P. Ott, président du jury  
Prof. A. Pautz, Dr B. Auchmann, directeurs de thèse  
Dr E. Ravaoli, rapporteur  
Dr T. Salmi, rapporteuse  
Prof. M. Seidel, rapporteur



Nothing in life is to be feared,  
it is only to be understood.  
Now is the time to understand more,  
so that we may fear less.  
— Marie Curie

To my family.





# Acknowledgements

First of all, I would like to thank Professor Andreas Pautz for serving as the thesis director, and for always having found time to discuss the thesis progress despite a very busy schedule. I am grateful for his enthusiastic support of the research and assistance with doctoral school's requirements. I would like to thank Bernhard Auchmann for serving as the thesis co-director, for explaining to me essential concepts in the field, for guiding me through the period of my research, and for his thorough editing of the thesis. I would also like to thank Dr. Peter Ott, Professor Mike Seidel, Dr. Emmanuele Ravaoli, and Dr. Tiina Salmi for serving on the committee and for their valuable feedback.

The work for this project was carried out in the magnet section at Paul Scherrer Institut (PSI). I would like to thank Stéphane Sanfilippo for inviting me to the superconducting magnet group, for supporting me to take courses and attend workshops, for always being open to new ideas and conversations, and for his kind advice and suggestions on both technical and practical sides during the thesis. I would like to thank and acknowledge everyone in the group who contributed to this work, making this thesis possible. Thanks to Ciro Calzolaio and Giuseppe Montenero for discussing technical issues with me. Thanks to Carolin Zoller for her assistance on the cryogenic infrastructure. Thanks to Alexander Gabard and Serguei Sidorov for their support on the technical drawings. Thanks to Philippe Lerch for teaching me how to use the measurement devices correctly. Thanks to Roland Felder and Christoph Hug for the preparation of samples. Thanks to Roland Deckardt for the help in the lab. Thanks to Marco Negrazus for producing the magnetic field maps in Opera. And thanks to Martin Paraliev for his kind assistance on the noise reduction for my subscale experiment.

I would also like to thank other scientists involved in this project, for their help and support coming outside of PSI. I would like to thank our colleagues working on CCT magnets at Lawrence Berkeley National Laboratory (LBNL). Thanks to Lucas Brouwer for his valuable help and input on ANSYS modeling. Thanks to Maxim Marchevsky and Marcos Turqueti for sharing their experience on the CCT instrumentation. Finally, I would like to thank Federico Scurti from North Carolina State University for his work on the fiberglass test.

This work was supported by the Swiss State Secretariat for Education, Research and Innovation SERI.

*Brugg, 30 April 2020*

Jiani Gao



# Abstract

From 2016, Paul Scherrer Institut (PSI) started an activity related to developing design, construction and testing of the superconducting magnets. My thesis work is part of this activity and mainly concerns the design and construction of an innovative high-field superconducting magnet of the Canted-Cosine-Theta (CCT) type - a possible candidate for the Future Circular Collider (FCC) 16 T dipole magnet design. The unique mechanical structure intercepts the accumulated forces lowering the stress on the windings, constituting intrinsic stress management in the high-field Nb<sub>3</sub>Sn accelerator magnets. However, this structure also constitutes a barrier for heat to quickly propagate in case of a quench. To succeed in the CCT-type magnet design and construction, quench protection is a challenging task that requires a detailed investigation of the electrothermal behavior of this magnet.

In this thesis, the potential detection and protection concepts are studied by the multiphysics simulations on a two-layer short model built at PSI and also in a subscale experiment. The 2D User-Defined Elements (UDEs) developed at Lawrence Berkeley National Laboratory (LBNL) in ANSYS Mechanical APDL, which support multi-dependence material properties and include the effect of inter-filament coupling currents, are adapted and used in the coupled electrothermal, electrodynamic, and electrical-circuits calculations for a two-layer CCT-type magnet with different protection methods, such as Coupling-Loss Induced Quench (CLIQ) and Energy-Extraction (EE) system. A first-of-a-kind CCT-type magnet protection study using UDEs is presented. The generic model method is validated through the test data of CCT4, a model magnet constructed at LBNL, protected by an energy-extraction system. The simulation predictions are the first steps of the conceptual design and feasibility validation of the construction of a fast and efficient quench protection system for CCT-type magnets to be operated in an accelerator. These calculations are to be compared to the experimental data in the near future on the PSI's first 1-m long two-layer CCT-type model magnet, CD1. Furthermore, these studies lay the ground for the four-layer CCT protection concepts for FCC.

*Keywords: superconducting magnets, Canted-Cosine-Theta (CCT), Future Circular Collider (FCC), quench detection, quench protection, numerical methods, multiphysics simulation, circuit modeling, CLIQ.*



# Résumé

Depuis 2016, l'Institut de Paul Scherrer (PSI) développe une activité liée à la conception, la construction et les tests d'aimants supraconducteurs. Mon travail de thèse fait partie de cette activité de recherche liée au développement d'un aimant supraconducteur à champ élevé avec une géométrie de type Canted-Cosine-Theta (CCT), candidat possible pour les aimants dipolaires 16 T du Futur Collisionneur Circulaire (FCC). La structure mécanique unique de ce type d'aimant intercepte les forces électromagnétiques accumulées et réduit les contraintes sur les enroulements. La gestion intrinsèque des contraintes est constituée pour maintenir les performances à champ élevé des aimants supraconducteurs de type CCT utilisant du Nb<sub>3</sub>Sn. Cependant, cette structure constitue également un obstacle pour une propagation rapide de la chaleur en cas de transition brutale de l'aimant de l'état supraconducteur vers l'état résistif (quench). Une protection efficace d'un aimant de type CCT pour éviter toute dégradation est une tâche difficile qui nécessite une étude détaillée du comportement électrothermique de ce type d'aimant.

Dans cette thèse, des concepts de détection et de protection potentiels sont étudiés par des simulations numériques multiphysiques sur un modèle court à deux couches construit au PSI et certains paramètres vérifiés expérimentalement dans des petits échantillons de câble supraconducteur. Les éléments définis par l'utilisateur (UDE) à deux dimensions développés par le laboratoire Lawrence Berkeley National Laboratory (LBNL) dans le logiciel ANSYS Mechanical APDL prennent en charge les propriétés des matériaux utilisés dans la modélisation. Ils incluent l'effet des courants de couplage inter-filamenteux, et utilisés dans les calculs des circuits électrothermiques, électrodynamiques et électriques couplés. Ils ont été utilisés pour un aimant de type CCT à deux couches avec différentes méthodes de protection, comme le Coupling-Loss Induced Quench (CLIQ) et le système d'extraction d'énergie (EE). La méthode et les résultats du modèle généré ont été validés par les données provenant du test à température cryogénique d'un aimant modèle (CCT4) construit au LBNL et protégé par un système d'extraction d'énergie. Les résultats de ces simulations sont les premières étapes de la conception et de la faisabilité d'un système de protection efficace contre les effets d'un quench pour les aimants de type CCT. Ces calculs doivent être comparés aux données expérimentales lors du futur test à température cryogénique du premier aimant modèle de type CCT (CD1), modèle à deux couches de 1-m de long construit au PSI. En outre, cette étude est une base solide pour le développement du système de protection des aimants CCT à quatre couches pour FCC.

## Acknowledgements

---

*Mots-clés : aimants supraconducteurs, Canted-Cosine-Theta (CCT), Futur Collisionneur Circulaire (FCC), détection de quench, protection contre les quenches, méthodes numériques, simulation multiphysique, modélisation de circuits, CLIQ.*

# Contents

|  |             |
|--|-------------|
| <b>Acknowledgements</b>  | <b>v</b>    |
| <b>Abstract (English/Français)</b>                                       | <b>vii</b>  |
| <b>List of figures</b>   | <b>xix</b>  |
| <b>List of tables</b>  | <b>xxii</b> |
| <b>1 Introduction</b>  | <b>1</b>    |
| 1.1 Future Circular Collider project . . . . .                           | 1           |
| 1.2 CCT-type magnets . . . . .   | 2           |
| 1.3 CCT program at PSI . . . . .   | 5           |
| 1.4 Critical surface and load line . . . . .                             | 8           |
| 1.5 Magnet quench and protection . . . . .                               | 10          |
| 1.6 Detection and protection methods . . . . .                           | 12          |
| 1.6.1 Detection methods . . . . .  | 13          |
| 1.6.2 Protection methods . . . . .                                       | 17          |
| 1.7 Thesis objectives . . . . .  | 20          |
| <b>2 Simulation Methods</b>  | <b>23</b>   |
| 2.1 Overview . . . . .   | 23          |
| 2.2 MIITs adiabatic calculation . . . . .                                | 25          |
| 2.2.1 MIITs calculation . . . . .  | 25          |
| 2.2.2 Time budget estimation . . . . .                                   | 27          |
| 2.2.3 Current decay expression . . . . .                                 | 28          |
| 2.2.4 System inductance . . . . .  | 28          |
| 2.3 Adiabatic integrator . . . . .                                       | 30          |
| 2.4 Magnetostatic and electrothermal finite-element model . . . . .      | 30          |
| 2.4.1 Model geometry and general settings . . . . .                      | 31          |
| 2.4.2 Material properties and homogenization . . . . .                   | 31          |
| 2.4.3 Critical current fit function . . . . .                            | 34          |
| 2.4.4 Magnetic-field map implementation . . . . .                        | 35          |
| 2.5 Electrothermal and magnetoquasistatic finite-element model . . . . . | 36          |
| 2.5.1 Basic formulations . . . . .                                       | 37          |

## Contents

---

|          |  |            |
|----------|--|------------|
| 2.5.2    | Model key features . . . . .   | 39         |
| 2.5.3    | Validation of automated model generator . . . . .                              | 44         |
| <b>3</b> | <b>Quench Protection</b>   | <b>49</b>  |
| 3.1      | Goals and overview . . . . .   | 49         |
| 3.2      | Energy extraction . . . . .  | 49         |
| 3.2.1    | Time budget estimation . . . . .   | 50         |
| 3.2.2    | Quench propagation simulation results . . . . .                                | 51         |
| 3.2.3    | Peak temperature estimation . . . . .  | 51         |
| 3.3      | Coupling-Loss Induced Quench . . . . .   | 53         |
| 3.3.1    | Simplified schematic of the electrical circuit . . . . .                       | 54         |
| 3.3.2    | Case of CLIQ, or EE, or both initiated together . . . . .                      | 56         |
| 3.3.3    | Case of CLIQ and EE with an in-between initiation delay time . . . . .         | 61         |
| 3.3.4    | Peak temperature estimation . . . . .  | 64         |
| 3.3.5    | CLIQ optimization . . . . .  | 64         |
| 3.4      | Co-wound copper tape . . . . .   | 72         |
| <b>4</b> | <b>Quench Detection</b>  | <b>79</b>  |
| 4.1      | Goals and overview . . . . .   | 79         |
| 4.2      | Current detection subscale experiment . . . . .                                | 79         |
| 4.2.1    | Goals of the experiment . . . . .  | 79         |
| 4.2.2    | Nb <sub>3</sub> Sn wire characterization . . . . .                             | 80         |
| 4.2.3    | Principle of current detection test setup . . . . .                            | 87         |
| 4.2.4    | Sample manufacturing . . . . .   | 92         |
| 4.2.5    | Current derivative sensor . . . . .  | 93         |
| 4.2.6    | Data acquisition system (DAQ) . . . . .  | 99         |
| 4.2.7    | Results and analysis . . . . .   | 102        |
| 4.3      | Instrumentation of CD1 . . . . .   | 115        |
| 4.3.1    | Voltage detection using a co-wound copper wire . . . . .                       | 116        |
| 4.3.2    | Optical detection using a co-wound optical fiber . . . . .                     | 118        |
| 4.3.3    | Final configuration . . . . .  | 118        |
| <b>5</b> | <b>Conclusion</b>  | <b>121</b> |
| 5.1      | Summary . . . . .  | 121        |
| 5.2      | Future work . . . . .  | 122        |
|          | <b>Bibliography</b>  | <b>123</b> |
| <b>A</b> | <b>Appendix</b>  | <b>133</b> |
| A.1      | Circuit coupling technical details . . . . .                                   | 133        |
| A.2      | Coupled model generation steps . . . . .                                       | 134        |
| A.3      | Peak temperature estimation with EE for different voltage thresholds . . . . . | 135        |
| <b>B</b> | <b>Glossary</b>  | <b>137</b> |



|                         |            |
|-------------------------|------------|
| <b>Curriculum Vitae</b> | <b>141</b> |
|-------------------------|------------|



# List of Figures

|      |  |    |
|------|--|----|
| 1.1  | Geographic localization of the Future Circular Collider. . . . .   | 1  |
| 1.2  | Sectional views of a four-layer CCT magnet design for the FCC. . . . .   | 3  |
| 1.3  | Full view of a two-layer CCT-type coil. . . . .  | 4  |
| 1.4  | Dipole field produced by a two-layer CCT-type coil. . . . .  | 4  |
| 1.5  | Cross section of a two-layer CCT-type coil. . . . .  | 5  |
| 1.6  | Structure of the CD1 model magnet. . . . .   | 7  |
| 1.7  | CD1 coil winding process with distinction of cable and former. . . . .   | 7  |
| 1.8  | Critical surfaces of Nb <sub>3</sub> Sn used in the CD1 cable. . . . .   | 8  |
| 1.9  | Load lines and different margins for an 8.4 T bore-field magnet design using Nb <sub>3</sub> Sn conductor. . . . .   | 9  |
| 1.10 | Different regimes of current distribution in a superconducting cable. . . . .  | 10 |
| 1.11 | Critical current versus temperature. . . . .   | 11 |
| 1.12 | Current profile versus time during a quench. 1a: detection phase $\Delta t_{\text{thres}}$ , 1b: validation phase $\Delta t_{\text{val}}$ , 2a: protection switch phase $\Delta t_{\text{switch}}$ , and 2b: discharge phase $\Delta t_{\text{dec}}$ . . . . . | 11 |
| 1.13 | Principle of direct and comparative voltage-based detection. . . . .   | 13 |
| 1.14 | Principle of voltage-based detection using a co-wound copper wire. (a) Electrical circuit; (b) Wire position inside the channel (not-to-scale). . . . .  | 14 |
| 1.15 | Electrical circuit of current-based detection. . . . .   | 15 |
| 1.16 | Linear array PCB antenna for quench localization, implemented in the CCT2 at LBNL. . . . .   | 16 |
| 1.17 | Electrical circuit of energy-extraction system. . . . .  | 18 |
| 1.18 | Electrical circuit of CLIQ system (Figure from [39]). . . . .  | 19 |
| 1.19 | Principle of inductive protection using a co-wound copper tape. (a) Position in the channel (not-to-scale); (b) Electrical circuit. . . . .  | 19 |
| 1.20 | Illustration of heater strips installed on the outer layer of a two-layer CCT coil. . . . .  | 20 |
| 2.1  | Peak temperature versus MIITs values at $B = 8.9$ T for the CD1 cable. . . . .   | 27 |
| 2.2  | CD1 differential inductance and comparison of current decay profile with/without $L_d(I)$ , when the CD1 is protected by a dump resistor of 40 m $\Omega$ , without consideration of quench resistance. . . . .  | 29 |

## List of Figures

---

|      |   |    |
|------|---|----|
| 2.3  | Quench propagation illustration in the CD1 3-turn helical model at 15.5 kA after 10 ms. The cable insulation is not included in the figure for a better illustration of temperature profiles in the bare cable and former. . . . .  | 31 |
| 2.4  | ANSYS plots of a 3-turn helical model of the CD1 inner layer, illustrating model geometry and meshing. . . . .  | 32 |
| 2.5  | Comparisons of critical current fit functions between the Summers and the simplified version for the CD1 at 15.5 kA. . . . .  | 35 |
| 2.6  | CD1 magnetic field distribution in Opera with a centre $B$ field of 10 T. Note that the yoke in this simulation is round, whereas the yoke aperture in the final CD1 magnet is square-shaped. . . . .   | 36 |
| 2.7  | Overview of coupled electromagnetic, circuit, and thermal simulation in ANSYS with user-defined elements at the example of CD1 (following [55]). . . . .  | 41 |
| 2.8  | The apparent cable cross-section in the cross-section of a CCT magnet, as compared to the actual cable cross-section. (a) CD1 insulated cable cross-section. The cross-section yields wide cable areas in the pole regions, observed in the red boxes; (b) Definition of cable areas. . . . . | 42 |
| 2.9  | Periodic slice model of a two-layer CCT-type coil. . . . .  | 43 |
| 2.10 | Lengths used in the definition of the length factor. . . . .  | 44 |
| 2.11 | CCT4 coil assembly at LBNL. The most-outer silver cylinder is the thick aluminum shell. . . . .   | 45 |
| 2.12 | Comparison of current decay curves from ANSYS with contributions of different losses in the CCT4 model magnet. . . . .  | 47 |
| 2.13 | Comparison of current decay curves between ANSYS simulation and test data at different current levels of the CCT4 model magnet, when the magnet is protected by a dump resistor of 30 m $\Omega$ . . . . .  | 47 |
| 3.1  | Quench propagation simulation results of a 3-turn CD1 helical model at 15.5 kA. . . . .   | 52 |
| 3.2  | Temperature profile in the centre of cable, of a 3-turn CD1 helical model in a quench propagation simulation at 1 kA, along the coil at different times. . . . .  | 52 |
| 3.3  | Simplified CD1 electrical circuit with EE and CLIQ. . . . .   | 54 |
| 3.4  | Simplified CD1 electrical circuit with EE and CLIQ in different time intervals of a transient protection simulation. . . . .  | 55 |
| 3.5  | CD1 initial electromagnetic field distribution at 15.5 kA. . . . .  | 56 |
| 3.6  | CD1 temperature distribution at 15.5 kA after 100 ms, when magnet is protected by only CLIQ, or by both EE and CLIQ system initiated at the same time. . . . .  | 57 |
| 3.7  | Current profiles in the inner layer $I_1$ and outer layer $I_2$ , with $I_C = I_2 - I_1$ , at different current levels, when the CD1 is protected by a CLIQ system of 400 V and 10 mF. . . . .  | 58 |
| 3.8  | Comparison of current decay curves from ANSYS with contributions of different losses in the CD1 model magnet. . . . .   | 59 |
| 3.9  | Current profile comparisons at 15.5 kA, when the CD1 is protected by only EE, or only CLIQ, or both EE and CLIQ initiated at the same time. . . . .   | 60 |

|      |  |    |
|------|--|----|
| 3.10 | CD1 temperature distribution at 15.5 kA after 100 ms, with both EE and CLIQ in the circuit, but initiated with different delay times. . . . .  | 62 |
| 3.11 | Current profile comparisons at 15.5 kA, when the CD1 is protected by both EE and CLIQ in the circuit, but initiated with different delay times. . . . .  | 63 |
| 3.12 | CD1 voltage to ground in the circuit at 15.5 kA, when CLIQ and EE are initiated at the same time or with a delay time of 20 ms. . . . .  | 63 |
| 3.13 | Comparison of induced current $I_C$ by CLIQ in the CD1 coil at 15.5 kA for different combinations of charging voltage $V_C$ and internal capacitance $C_C$ . . . . .                                       | 65 |
| 3.14 | CD1 temperature distribution on the bare cable at 15.5 kA after 5 ms, when magnet is protected by only CLIQ, for different combinations of charging voltage $V_C$ and internal capacitance $C_C$ . . . . . | 67 |
| 3.15 | Quench propagation simulation results of a 5-turn CD1 helical model at 1.4 kA for determination of the lowest current level to be self-protected. . . . .  | 68 |
| 3.16 | Current discharge in the CD1, when magnet is protected by a CLIQ system of 800 V and 10 mF. . . . .  | 69 |
| 3.17 | Electrical circuit of inductive protection using a co-wound copper tape for the CD1. . . . .   | 73 |
| 3.18 | Comparisons of current and temperature profiles, between the nominal CD1 cable, and the Cable A with a co-wound copper tape. . . . .   | 76 |
| 3.19 | Comparisons of current and temperature profiles, between the nominal CD1 cable, and the Cable B with a co-wound copper tape. . . . .   | 76 |
| 4.1  | Critical current profile as a function of magnetic field of the Nb <sub>3</sub> Sn sensing wire. . . . .   | 80 |
| 4.2  | Electrical circuit of $T_{c0}$ experiment of Nb <sub>3</sub> Sn sample. . . . .  | 81 |
| 4.3  | Cernox cryogenic temperature sensors. . . . .  | 81 |
| 4.4  | Electrical circuit of $T_{c0}$ experiment of Nb <sub>3</sub> Sn and Nb-Ti samples. . . . .   | 82 |
| 4.5  | Piping and instrumentation diagram of $T_{c0}$ experiment of Nb <sub>3</sub> Sn and Nb-Ti samples with current leads (not-to-scale). . . . .   | 83 |
| 4.6  | Heat leak to the cold end of each current lead as a function of wire diameter, when the current is 6 A and wire length is 1.5 m long. . . . .  | 84 |
| 4.7  | Nb-Ti and Nb <sub>3</sub> Sn samples for $T_{c0}$ experiment. . . . .  | 84 |
| 4.8  | Sample holder insulation for $T_{c0}$ experiment. . . . .  | 85 |
| 4.9  | Experimental setup of $T_{c0}$ experiment of superconducting wires. . . . .  | 85 |
| 4.10 | $T_{c0}$ experiment results of Nb <sub>3</sub> Sn and Nb-Ti wires, when the current is 6.2 A. . . . .  | 85 |
| 4.11 | Electrical circuit of current detection test. . . . .  | 87 |
| 4.12 | Piping and instrumentation diagram of current detection test with current leads (not-to-scale). . . . .  | 88 |
| 4.13 | Experimental setup of current detection. . . . .   | 89 |
| 4.14 | Sample cross-section design for current detection test (not-to-scale). . . . .   | 90 |
| 4.15 | Sample overview with connection wires for current detection test (not-to-scale). . . . .   | 91 |
| 4.16 | Sample construction process for current detection test. . . . .  | 93 |
| 4.17 | Sample with mold during impregnation process for current detection test. . . . .   | 94 |

## List of Figures

---

|   |     |
|---|-----|
| 4.18 Current derivative sensor design (following [105]). . . . .  | 94  |
| 4.19 Properties of mumetal (Data from [106]). . . . .   | 96  |
| 4.20 Current derivative sensor core shape for current detection test. . . . .   | 97  |
| 4.21 Current derivative sensor fabrication process. (a) Initial toroidal mumetal core;<br>(b) Pour epoxy resin on mumetal core for impregnation; (c) Degas in vacuum;<br>(d) Put windings on half core. . . . .         | 98  |
| 4.22 Final current derivative sensor in an iron shield box. . . . .   | 98  |
| 4.23 Calculated voltage on the current derivative sensor versus different air gap thick-<br>nesses, assuming a 2 A current flows in the primary circuit, with a current drop<br>of 1 mA in 1 ms to be detected. . . . . | 99  |
| 4.24 Connection scheme for the current signal in the heater circuit, measured on $R_1$ . . . . .  | 100 |
| 4.25 Connection scheme for the voltage signal on the secondary of the current deriva-<br>tive sensor. . . . .   | 101 |
| 4.26 Connection scheme for the current signal in the superconducting circuit, mea-<br>sured on $R_2$ . . . . .  | 101 |
| 4.27 Heat pulse delivered in the heater strip over time. Its amplitude is 5.2 A and<br>length is 20 ms. . . . .   | 103 |
| 4.28 Current detection results on Sample 1 with $R_3 = 3.3 \Omega$ , when a heat pulse of 5.2 A<br>is applied for 20 ms. . . . .  | 104 |
| 4.29 Simulation results for current detection, when a heat pulse of 5.2 A is applied for<br>20 ms. . . . .  | 105 |
| 4.30 Current detection test results on Sample 1 with $R_3 = 3.3 \Omega$ , when varying the<br>length and amplitude of the applied heat pulse to determine minimum quench<br>energy. . . . .                             | 107 |
| 4.31 Energy density versus measured quench delay time. The Point 1 to 4 correspond<br>respectively a heat pulse duration of 20, 15, 10 and 5 ms. . . . .  | 107 |
| 4.32 Locations of cutting surfaces of Sample 1. . . . .   | 108 |
| 4.33 Cutting surfaces of Sample 1 for determination of the distance between the<br>heater strip and the edge of superconducting wire, as well as the transverse<br>thickness of epoxy resin. . . . .                    | 108 |
| 4.34 Current detection results on Sample 1 with $R_3 = 1 \Omega$ , when a heat pulse of 5.2 A<br>is applied for 20 ms. . . . .  | 110 |
| 4.35 Transverse quench delay time (from heater initiation to first peak on the sensor)<br>obtained from the experiment and simulation with different $T_{init}$ in the current<br>detection test. . . . .               | 111 |
| 4.36 Current detection results on Sample 2 with $R_3 = 3.3 \Omega$ , when a heat pulse of 5.2 A<br>is applied for 30 ms. . . . .  | 112 |
| 4.37 Locations of cutting surfaces of Sample 2. . . . .   | 112 |
| 4.38 Cutting surfaces of Sample 2 for determination of the distance between the<br>heater strip and the edge of superconducting wire, as well as the transverse<br>thickness of epoxy resin. . . . .                    | 113 |
| 4.39 Quench instrumentation of LBNL's model magnets. . . . .  | 116 |

|   |     |
|---|-----|
| 4.40 Insulation braiding with a thin co-wound copper wire. . . . .  | 117 |
| 4.41 Ceramic-insulated copper wire before and after the thermal cycle. (a) Before<br>thermal cycle; (b) Ceramic peeled off after thermal cycle. . . . . | 117 |
| 4.42 Final CD1 instrumentation. . . . .   | 118 |
| 4.43 Finished CD1 magnet assembly. . . . .  | 119 |





# List of Tables

|     |   |    |
|-----|---|----|
| 1.1 | FCC-hh baseline parameters compared to the LHC and HL-LHC parameters. .   | 2  |
| 1.2 | PSI's four-layer CCT design parameters for the FCC. . . . .   | 3  |
| 1.3 | Main parameters of the CD1 Nb <sub>3</sub> Sn dipole magnet. . . . .  | 6  |
| 1.4 | Typical value of different times for a traditional quench protection system. . . .  | 12 |
| 2.1 | Overview of simulation methods. . . . .   | 24 |
| 2.2 | Source of material property for each type material used in the ANSYS FEM simulation. . . . .  | 33 |
| 2.3 | Main parameters of the CCT4 Nb <sub>3</sub> Sn dipole magnet of LBNL. . . . .   | 45 |
| 2.4 | Dimensions of different layers of the CCT4 Nb <sub>3</sub> Sn dipole magnet of LBNL. . . .  | 46 |
| 3.1 | Estimation of time budget by MIITs calculation for the CD1, when magnet is protected by a dump resistor of 40 mΩ. . . . .   | 50 |
| 3.2 | Sensitivity study of Cu RRR on time budget estimation by MIITs calculation for the CD1. . . . .   | 51 |
| 3.3 | CD1 peak temperature estimation after a quench, when magnet is protected by a dump resistor of 40 mΩ. . . . .   | 53 |
| 3.4 | Different case studies in CLIQ quench protection simulation. . . . .  | 53 |
| 3.5 | CD1 peak temperature at 15.5 kA after 100 ms, when magnet is protected by both EE and CLIQ in the circuit, but initiated with different delay times. . . . .  | 61 |
| 3.6 | CD1 peak temperature at different current levels after 100 ms, when magnet is protected by only CLIQ, and by both EE and CLIQ in the circuit, but initiated with a delay time of 20 ms. . . . .                 | 64 |
| 3.7 | Estimation of time budget by MIITs calculation, when the CD1 is protected by a CLIQ system of 800 V and 10 mF . . . . .   | 69 |
| 3.8 | Estimation of time budget by MIITs calculation, when the CD1 is protected by a CLIQ system of 700 V and 40 mF, or of 620 V and 80 mF . . . . .  | 70 |
| 3.9 | Proposed combination of voltage threshold, time to reach threshold, maximum validation time and switch time at different current levels when the CD1 is protected by a CLIQ system of 700 V and 40 mF . . . . . | 71 |

## List of Tables

---

|      |   |     |
|------|---|-----|
| 3.10 | Proposed combination of voltage threshold, time to reach threshold, maximum validation time and switch time at different current levels, when a magnet having the CD1 geometry with a magnetic length of 14.3 m, is protected by a CLIQ system of 1.2 kV and 50 mF . . . . .          | 72  |
| 3.11 | Cable parameters for inductive protection study in a two-layer CCT. . . . .   | 75  |
| 3.12 | Estimation of time budget by MIITs calculation, when the CD1 is protected by a co-wound copper tape. MIITs is the total value from the quench detection to the end of current decay whereas MIITs <sub>decay</sub> is the value for the current decay after quench detection. . . . . | 77  |
| 4.1  | Sample wire parameters with calculated and measured voltage for $T_{c0}$ experiment when a current of 6.2 A is applied. . . . .   | 86  |
| 4.2  | Solid state relay specifications. . . . .   | 88  |
| 4.3  | Sample main parameters for current detection test. . . . .  | 90  |
| 4.4  | Main parameters of the constructed current derivative sensor. . . . .   | 98  |
| 4.5  | Measured distances between the heater strip and superconducting wire, and resin thickness on cutting surfaces of Sample 1. . . . .  | 109 |
| 4.6  | Measured distances between the heater strip and superconducting wire, and resin thickness on cutting surfaces of Sample 2. . . . .  | 113 |
| A.1  | Time needed to reach different voltage thresholds $\Delta t_{thres}$ for CD1. . . . .   | 135 |
| A.2  | CD1 peak temperature estimation after a quench, when the magnet is protected by a dump resistor of 40 m $\Omega$ , for different voltage thresholds. . . . .  | 135 |

# 1 Introduction

## 1.1 Future Circular Collider project

The Future Circular Collider (FCC) study explores the post-LHC (Large Hadron Collider) era [1, 2, 3, 4, 5, 6]. In a tunnel of approximately 100 km circumference, which is more than three times of the size of LHC, a hadron collider, so-called FCC, is conceptually designed to increase the centre-of-mass energy from 14 to 100 TeV, and the peak luminosity from 1.0 to  $30 \times 10^{34} \text{ cm}^{-2} \text{ s}^{-1}$  [5]. The particle centre-of-mass energy and the beam peak luminosity are pushed to another high level in order to further study the high-energy physics. Figure 1.1 illustrates the proposed location of the new FCC tunnel. Table 1.1 summarizes the FCC-hh baseline parameters, including a comparison with the LHC and HL-LHC (High-Luminosity LHC) parameters.

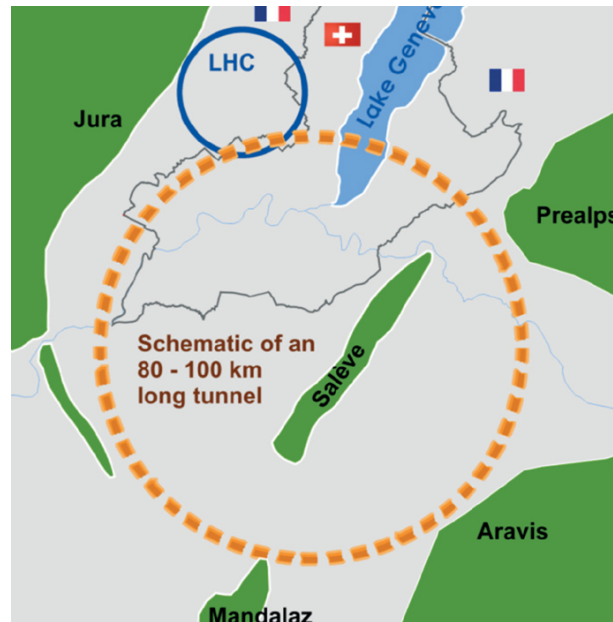


Figure 1.1 – Geographic localization of the Future Circular Collider.

Table 1.1 – FCC-hh baseline parameters compared to the LHC and HL-LHC parameters.

|  | LHC | HL-LHC    | FCC-hh                  |         |
|--|-----|-----------|-------------------------|---------|
|  |     |           | Initial                 | Nominal |
| c.m. Energy [TeV]  |     | 14        |                         | 100     |
| Circumference C [km]   |     | 26.7      |                         | 97.75   |
| Dipole field [T]   |     | 8.33      |                         | < 16    |
| Arc filling factor   |     | 0.79      |                         | 0.8     |
| Straight sections  |     | 8 × 528 m | 6 × 1400 m + 2 × 2800 m |         |
| Peak luminosity [ $10^{34} \text{ cm}^{-2} \text{ s}^{-1}$ ] | 1.0 | 5.0       | 5.0                     | < 30.0  |
| Dipole coil aperture [mm]                                    |     | 56        |                         | 50      |

To steer a 100 TeV beam over a 100 km tunnel, a total amount of 4578 dipole magnets with a length of 14.3 m for each is required. A magnetic field of 16 T needs to be produced, based on a calculation using the following magnetic rigidity formula [7],

$$B\rho = \frac{p}{e} \quad (1.1)$$

or in practical units,

$$[\text{T} \cdot \text{m}] B\rho = \frac{1}{0.29979} p_m \left[ \frac{\text{GeV}}{c} \right] \quad (1.2)$$

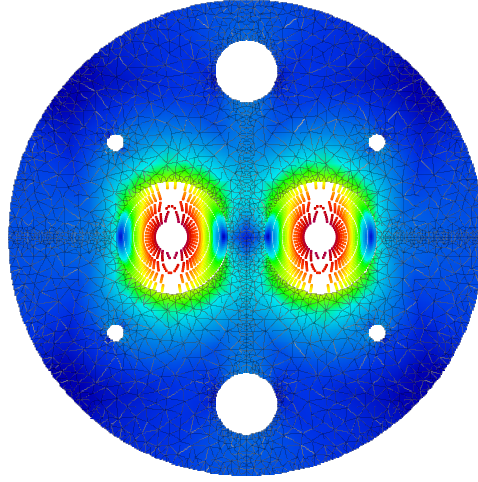
where  $B$  is the dipole field,  $B\rho$  the beam rigidity,  $\rho$  the dipole bending radius,  $p_m$  the momentum of the particle, and  $e$  the particle charge.

Among various magnet geometries, a four-layer twin-aperture Canted-Cosine-Theta (CCT) type 16 T Nb<sub>3</sub>Sn superconducting dipole magnet has been proposed as a possible candidate and has been designed for the FCC [8, 10, 11]. The magnet design is shown in Figure 1.2 and the key parameters are listed in Table 1.2. In this table, cuNc is the copper to non-copper (superconductor) ratio in a strand. The superconductor fraction in a strand is thus given by  $f_{sc} = 1/(1 + \text{cuNc})$ .

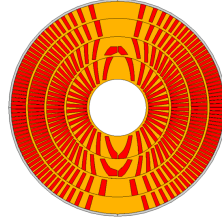
Since 2016, the magnet section at the Paul Scherrer Institut (PSI), in collaboration with CERN (European Organization for Nuclear Research) and LBNL (Lawrence Berkeley National Laboratory), is responsible for the R&D of this magnet type in terms of optimization of the FCC design, with respect to safety and efficiency, which motivates my thesis subject: analysis of quench detection and protection of a Nb<sub>3</sub>Sn CCT technology demonstrator dipole for FCC.

## 1.2 CCT-type magnets

In modern accelerators, superconducting magnets are used in the pursuit of high fields and high current densities. As a result, high Lorentz forces are accumulated on the coil windings, which tend to push the conductor towards the mid planes and supporting structure, causing a



(a) Twin-aperture CCT magnet design.



(b) Coil sectional view.

Figure 1.2 – Sectional views of a four-layer CCT magnet design for the FCC.

Table 1.2 – PSI's four-layer CCT design parameters for the FCC.

| Layer number             | 1         | 2         | 3         | 4         |
|--------------------------|-----------|-----------|-----------|-----------|
| Current [A]              | 18025     | 18025     | 18025     | 18025     |
| Inner bore radius [m]    | 0.025     | 0.0456    | 0.0636    | 0.0798    |
| Spar [m]                 | 0.0015    | 0.0015    | 0.0015    | 0.0015    |
| Strand diameter [m]      | 0.0012    | 0.0012    | 0.0012    | 0.0012    |
| Number of strands        | 29        | 25        | 22        | 20        |
| cuNc                     | 0.8       | 1.1       | 1.95      | 2.6       |
| Cable thickness [m]      | 0.002184  | 0.002184  | 0.002184  | 0.002184  |
| Cable width [m]          | 0.01827   | 0.01575   | 0.01386   | 0.0126    |
| Insulation thickness [m] | 0.00015   | 0.00015   | 0.00015   | 0.00015   |
| RRR                      | 110       | 110       | 110       | 110       |
| Tilt [deg]               | 15        | -15       | 15        | -15       |
| Pitch [m]                | 0.0110581 | 0.0110581 | 0.0110581 | 0.0110581 |
| $B_{\text{mean}}$ [T]    | 14.75     | 11.466    | 8.089     | 6.28      |
| $B_{\text{max}}$ [T]     | 16.35     | 15.2      | 13.22     | 11.58     |
| Number of turns          | 1294      | 1294      | 1294      | 1294      |
| Length of a turn [m]     | 0.436398  | 0.775854  | 1.08583   | 1.35466   |

stress increase on the conductor, and therefore a conductor movement or a deformed winding [12]. The conductor stress must be minimized due to the nature of  $\text{Nb}_3\text{Sn}$  being a brittle superconductor material [13]. Currently, the resulting stress should be maintained below 150 MPa at room temperature and below 200 MPa in cryogenic conditions in order to avoid any performance degradation in  $\text{Nb}_3\text{Sn}$  magnets [14].

In addition to an external supporting structure, the CCT-type magnet features an internal structure that is part of the coils. A full view of a two-layer CCT coil is presented in Figure 1.3. A CCT magnet superposes fields of nested and tilted solenoids that are oppositely canted. The current distribution of a canted layer generates a pure dipole field as well as a solenoid field that can be canceled with an oppositely canted layer [15]. The particles are thus bent by the pure dipole field. Figure 1.4 illustrates the superposition of produced fields. In a two-layer CCT coil, the rib and spar are pointed out in Figure 1.5. The ribs are placed between the adjacent cable turns and the spars are located beneath the insulated cables. Ribs and spars constitute winding formers. The superconducting cables are placed within the formers intercepting Lorentz forces of each turn to prevent stress accumulation on the coil.

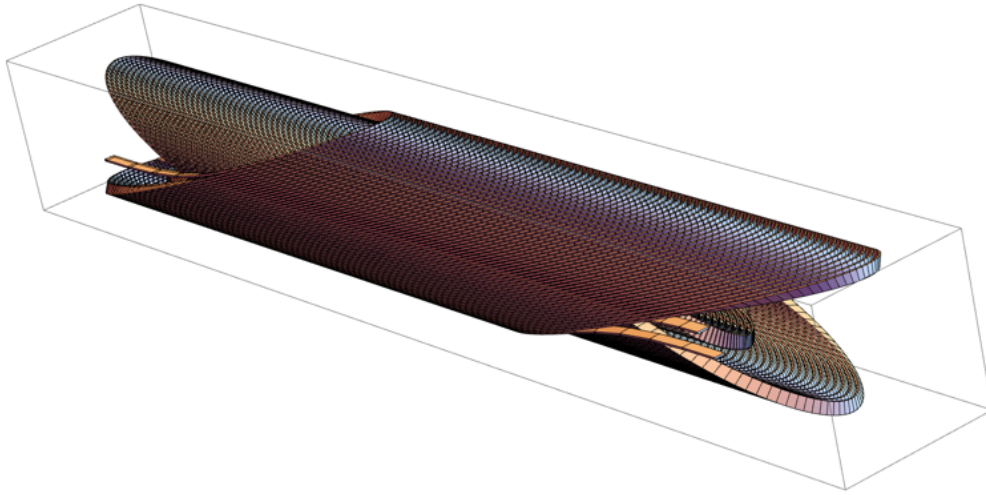


Figure 1.3 – Full view of a two-layer CCT-type coil.

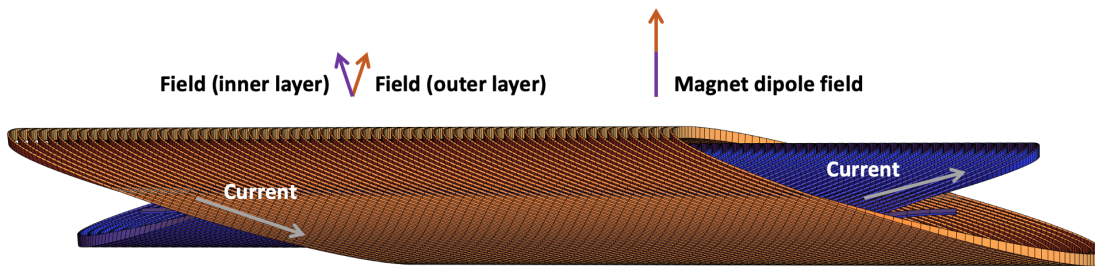


Figure 1.4 – Dipole field produced by a two-layer CCT-type coil.

The concept of coil pre-stress is applied in most of the accelerator dipole magnets [16]. However, the winding formers of CCT-type magnet provide an intrinsic azimuthal and axial stress

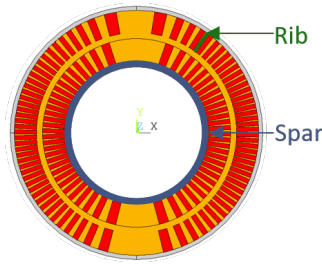


Figure 1.5 – Cross section of a two-layer CCT-type coil.

management since the Lorentz forces are transmitted first to the ribs, and then to the solid spar. Thanks to this unique mechanical structure, a lower stress on the coil and thus a better mechanical stability are expected at high field, comparing to other conventional superconducting magnets as each turn is independently supported [10].

In the LHC, a large amount of superconducting dipole and quadrupole magnets are equipped with quench heaters in order to protect the superconducting magnets in case of a quench [17, 18]. These quench heaters consist of a thin stainless steel strip covered by a layer of polyimide foil on each side for electrical insulation purposes. When there is a big contact surface between the heaters and the coil, the fired quench heaters can bring the entire coil to the normal state in a fast way. The stored magnetic energy is dissipated in the entire coil and therefore the coil temperature remains low enough compared to the allowed maximum temperature in the magnet because of the quench heaters.

However, for the CCT-type magnets, the traditional quench heaters become inefficient since a big amount of heat produced is transferred to the former rather than to the superconducting cables. Therefore the CCT-type magnet design and its construction are challenging in the aspect of protection. In my thesis, the specific issues of quench detection and protection are studied.

### 1.3 CCT program at PSI

LBNL started working on CCT-type magnets as part of the LBNL magnet R&D since 2013 and within the US Magnet Development Program (MDP) since 2016 [19, 20], pursuing a high-field dipole development and exploring the limits of  $\text{Nb}_3\text{Sn}$  technology [15]. PSI's program is complementary to LBNL's program to provide specific features in terms of efficiency (design, performance, protection and cost reduction) of CCT magnets for FCC. The keys to an efficient CCT design are thin spars combined with an external mechanical structure, wide cable (large strands) and thin ribs, allowing an increased current density [21, 22]. To achieve this goal, PSI collaborates closely with LBNL to exchange ideas and discuss progress.

At PSI, a two-layer 1-m long  $\text{Nb}_3\text{Sn}$  CCT model magnet (called CD1, Canted Dipole) was built to further explore CCT technology [23]. The main parameters, as well as the magnet

component materials are listed in Table 1.3. The magnetic design of the two-layer CCT model coil features a short sample current of  $I_{ss} = 18.1$  kA and a field of  $B = 10.4$  T in the magnet centre, at a working temperature  $T_{op} = 4.2$  K [22] <sup>1</sup>.

Table 1.3 – Main parameters of the CD1 Nb<sub>3</sub>Sn dipole magnet.

| Magnet parameter                | Value              |
|---------------------------------|--------------------|
| Number of turns                 | 66                 |
| Cable thickness                 | 1.475 mm           |
| Cable width                     | 9.85 mm            |
| Number of strands               | 21                 |
| Strand diameter                 | 0.85 mm            |
| Filament twist pitch            | 9 mm               |
| Glassfiber insulation thickness | 0.15 mm            |
| Cu RRR                          | 150                |
| Non-Cu fraction                 | 0.465              |
| Short-sample current (4.2 K)    | 18.1 kA            |
| Short-sample bore field (4.2 K) | 10.4 T             |
| Coil physical length            | 1 m                |
| Coil magnetic length            | 0.6 m              |
| Magnet component                | Material           |
| Strand type                     | Nb <sub>3</sub> Sn |
| Former (spar, rib)              | Aluminum bronze    |
| Protective shell                | Aluminum           |
| Pad                             | Aluminum bronze    |
| Outer shell                     | Aluminum           |

The construction of CD1 introduces CCT technology to PSI, in cable winding, heat treatment, impregnation methods, and mechanical structure. In order to keep a low stress on the coil and minimize the movement of the coil, a bladder-and-key type structure with an aluminum shell has been introduced for an increased rigidity of the impregnated coil-former assembly. The design of the model magnet together with the mechanical structure is illustrated in Figure 1.6. The supporting structure includes an aluminum protective shell enveloping the two-layer coil, two symmetric aluminum bronze pads surrounding the coils, two half iron yokes surrounding the pads, and an outer aluminum shell enclosing the whole structure.

Figure 1.7a presents the manufactured CD1 formers with the distinction of rib and spar. There are in total 66 turns in the model magnet CD1. The Nb<sub>3</sub>Sn cable shown in Figure 1.7b, is insulated with a thick fiberglass braided sleeve. The insulated cable is then wound into the channels between the ribs, as illustrated in Figure 1.7c. After the heat treatment, all the voids in the coil volume are filled with epoxy resin.

<sup>1</sup>The magnetic design was re-validated in April 2020 with the following parameters: the short sample current 17.64 kA, the peak field on the conductor 10.65 T and the dipole field in the magnet centre 9.74 T, at a working temperature 4.2 K.



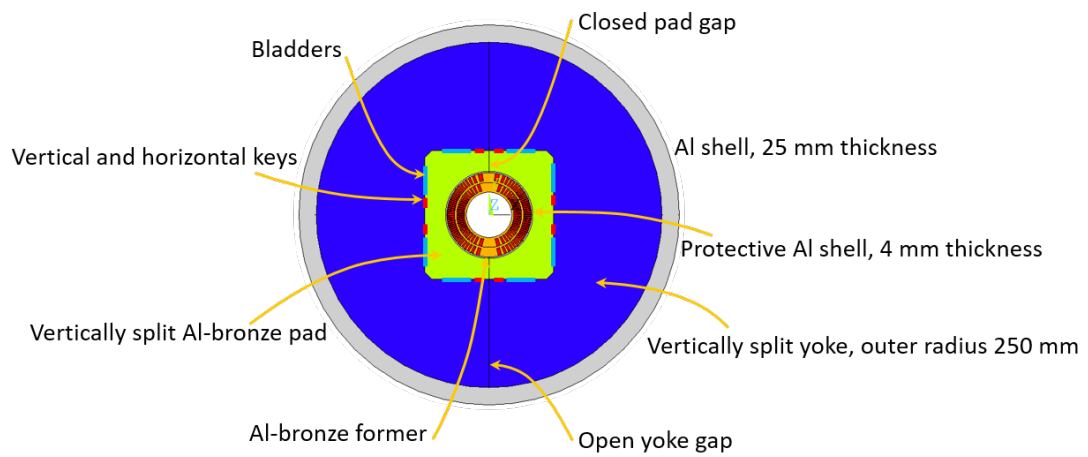
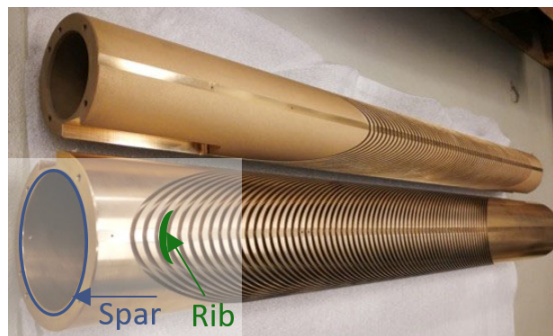
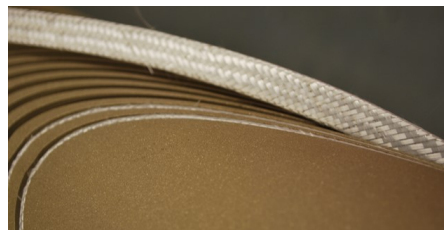


Figure 1.6 – Structure of the CD1 model magnet.



(a) 1-m long formers.



(b) Nb<sub>3</sub>Sn cable windings.



(c) Coil winding process.

Figure 1.7 – CD1 coil winding process with distinction of cable and former.

The development of a quench protection system for the CCT magnets is an important part of the PSI magnet program. In the framework of my thesis, a detection and protection system for PSI's model magnets CD1 is therefore designed and implemented. The CD1 test will take place in the near future<sup>2</sup>.

### 1.4 Critical surface and load line

Some essential notions often used in the field of superconducting magnets are introduced in this section for a better understanding of the study.

The critical surface is the boundary between the superconducting state and normal state in the current density  $J$ , magnetic field  $B$ , temperature  $T$  space. It is defined by the short sample (SS) measurements and considered as the perfect magnet's physical performance limit. Everywhere below the critical surface is the superconducting state and everywhere above it is the normal state. The critical surface is described by the critical current fit functions, which are implemented in the quench simulations to determine different regimes. Figure 1.8 displays the critical surface of Nb<sub>3</sub>Sn used in the CD1 cable.  $T_{c0}$  is the maximum critical temperature (at  $B = 0$ ) and  $B_{c20}$  is the maximum critical field (at  $T = 0$ ). These two parameters are determined by the characteristics of superconducting material. It is worth noting that, for strain-sensitive Nb<sub>3</sub>Sn material,  $T_{c0}$  and  $B_{c20}$  also have a dependency on strain. The existence of strain could lead to a reduction in  $J_c$ .

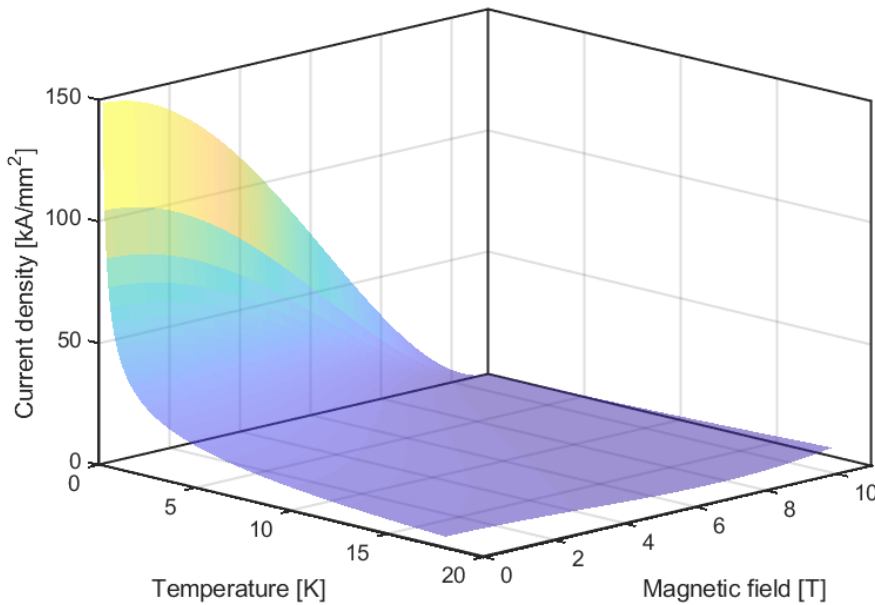


Figure 1.8 – Critical surfaces of Nb<sub>3</sub>Sn used in the CD1 cable.

---

<sup>2</sup>The outbreak of Coronavirus disease (COVID-19) caused a delay on the magnet test.

At a fixed temperature, the relationship between the magnet current and field on the conductor can be plotted. The operation point is determined by the magnet design. The line connecting the working point and zero is called the load line. If we extend it until it reaches the short sample curve, we obtain what is called in superconducting magnet jargon "100% of short sample on the load line". The load line is temperature-independent. Typically the working point is situated between 60 and 86% of the short sample on the load line, which means a load line margin of 40 to 14%. The value of working point is selected empirically based on many prototypes, e.g., HL-LHC [24]. Figure 1.9a shows the load lines of an 8.4 T bore-field magnet design using  $\text{Nb}_3\text{Sn}$  conductor. The yellow line represents the field in the magnet aperture, whereas the red line represents the peak field on the superconductor. The peak field on the superconductor is always larger than the field in the magnet aperture. The ratio between them depends on the selected coil geometry.

For magnets operated in liquid helium, the critical surface is represented by a curve of current versus field at 4.2 K. For magnets operated in superfluid helium, e.g., magnets of LHC and prospective FCC, the critical surface is represented by a curve of current versus field at 1.9 K. The practical operation always requires safety margins: critical current margin, critical field margin, margin along the load line, and temperature margin (Figure 1.9b). These margins can limit the number of training quenches, i.e., progressive improvement of the reached field level after a series of repeated quenching events, and avoid quenches during operation, described in the following section. The margin needed depends on the design and operating conditions.

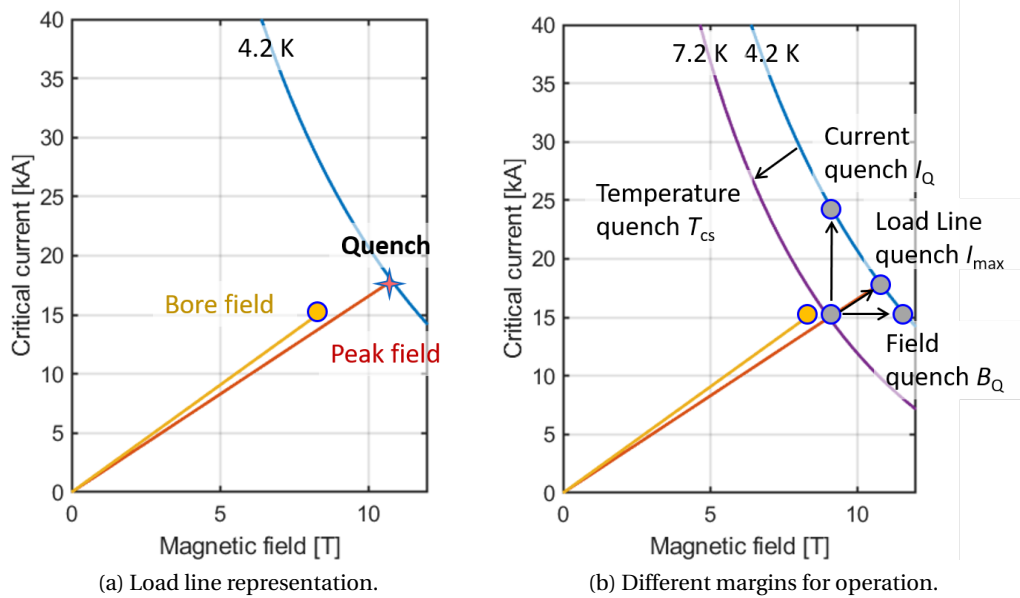


Figure 1.9 – Load lines and different margins for an 8.4 T bore-field magnet design using  $\text{Nb}_3\text{Sn}$  conductor.

## 1.5 Magnet quench and protection

Quench is the sudden transition from the superconducting to the normal-conducting state. It happens when the working point exceeds the critical surface, which is defined by current density, temperature and magnetic field. The triggering of a quench can have several origins. The temperature increase can be caused due to conductor movement (resin cracking), induced eddy current losses, radiation, beam losses, quench heaters, and heat transfer (adjacent parts). If one of those events occurs, then a certain amount of heat is deposited in the cable resulting in a rise in temperature. When the local temperature becomes higher than the critical temperature value, the superconducting properties are lost locally (i.e., an increasing zone of normal conductivity) causing a jump in resistance and rapid Joule heating in the coil. An increase in current or field also quenches the magnet once the critical surface is exceeded. These can be caused by induced voltage, current variation, and external fields. During a quench, a large amount of magnetic energy stored is released into heat after a quench detection and can destroy the magnet in the worst case [25].

There are three regimes of current distribution in the superconducting cable, presented in Figure 1.10), using  $\text{Nb}_3\text{Sn}$  as an example. In a  $\text{Nb}_3\text{Sn}$  superconducting cable, the superconducting filaments are embedded in a copper matrix to provide time to act on power circuit and stabilize the conductor against flux jumps.

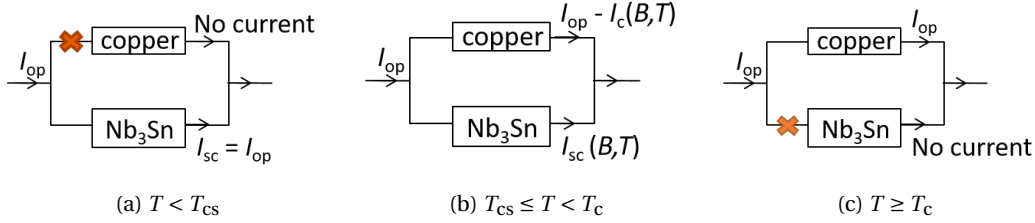


Figure 1.10 – Different regimes of current distribution in a superconducting cable.

Figure 1.10a illustrates the normal operating regime where the total current in the cable  $I_{op}$  goes into the superconductor, when the local  $T$  is smaller than the current-sharing temperature  $T_{cs}$ . If the local  $T$  exceeds  $T_{cs}$ , then a part of current starts flowing into the stabilizer, called the current-sharing regime, as shown in Figure 1.10b, where  $I_{sc}(B, T)$  is the current flowing into the superconductor, and  $I_{op} - I_{sc}(B, T)$  is the current flowing into the stabilizer. If the local  $T$  increases further, reaching the critical temperature  $T_c$ , all the current goes into the stabilizer, shown in Figure 1.10c.

The current level flowing in the superconductor depends on the temperature and  $B$  field [26]:

$$I_{sc}(B, T) = \begin{cases} I_{op}, & T < T_{cs}(B) \\ I_{op} \frac{T_c - T}{T_c - T_{cs}(B)}, & T_{cs}(B) \leq T < T_c \\ 0, & T \geq T_c \end{cases} \quad (1.3)$$

The relationship between magnet current and temperature is presented in Figure 1.11. Note that the Joule losses start at  $T_{cs}$ .

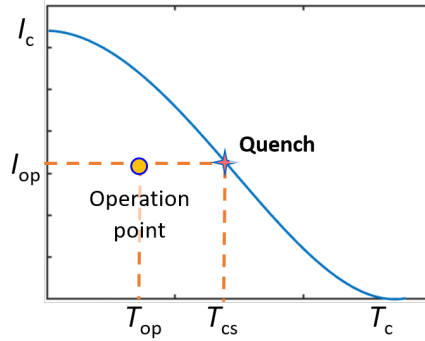


Figure 1.11 – Critical current versus temperature.

When a short part of the conductor is heated to be resistive due to any possible reason, if more heat is moved out of the resistive zone than generated therein, the resistive zone shrinks. Otherwise, it grows to trigger a quench. The minimum propagating zone MPZ is the minimum zone that produces enough heat at a given current, magnetic field, and cooling condition. The minimum quench energy MQE is the amount of energy needed to put into a given zone over a given time interval at a given temperature, magnetic field and current to produce thermal runaway. When MPZ and MQE are as large as possible, it is difficult to quench the conductor which is good for the quench stability. However, they may well be bad for quench protection, as detection takes longer and the protection systems may be ineffective.

During the process of a quench, we can distinguish different phases and associate them with time, as shown in Figure 1.12.

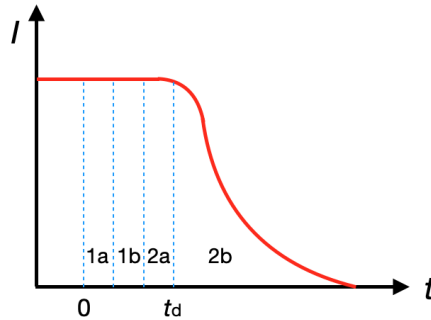


Figure 1.12 – Current profile versus time during a quench. 1a: detection phase  $\Delta t_{thres}$ , 1b: validation phase  $\Delta t_{val}$ , 2a: protection switch phase  $\Delta t_{switch}$ , and 2b: discharge phase  $\Delta t_{dec}$ .

When the current stays constant, the quench propagates until the resistive voltage reaches a pre-set threshold (in case of a voltage detection) (detection  $\Delta t_{thres}$ ), then some extra time is added to confirm if it is a real quench (validation  $\Delta t_{val}$ ). After a detection, the magnet current supply is disconnected and the protection system is fired to trigger a quench over the whole

coil to increase the quench resistance (protection switch  $\Delta t_{\text{switch}}$ ), consequently, the current drops and the magnetic energy is dissipated (discharge  $\Delta t_{\text{dec}}$ ). It is worth noting that  $t_d$  is the time when the power is switched off and the current starts to decrease. Some typical values for a traditional quench protection system are listed in Table 1.4 [27].

Table 1.4 – Typical value of different times for a traditional quench protection system.

| Name   | Time [ms] |
|--|-----------|
| Detection time for a voltage threshold of about 100 mV | 5-20      |
| Validation time to avoid false triggers                | 5-20      |
| Switch opening for discharge                           | 1-5       |
| Switch opening for quench heaters                      | 1-2       |
| Heater delay time from strip to cable                  | 10-40     |

When a quench occurs, the stored magnetic energy is converted into heat. The overheating of the coil leads to damage to the components, e.g., conductor, insulation, and splices. The abrupt decrease of current can result in large inductive voltage spikes and arcing, causing internal short circuits. Moreover, the mechanical structure can be over-stressed during a quench.

Magnet protection against quench damage is to take proper actions to safely dissipate the stored magnetic energy and limit the maximum temperature in the magnet. The location of the initial transition from the superconductor to the normal conductor is generally where the maximum temperature appears since the Joule heating lasts for the longest time. This maximum temperature can also be called peak temperature or hot-spot temperature. The allowable peak temperature after a quench is given by the lowest temperature at which any of the used materials either breaks or deforms plastically. This lowest temperature is the glass-transition temperature  $T_g$  of the resin. If we pass it, the coil risks deforming permanently.

During a quench, the action of turning off the power source is far and away not quick enough to protect the coils because the hot-spot temperature increases with time before the current turns to zero. Thus protection system is needed to accelerate the current discharge in the coil.

## 1.6 Detection and protection methods

In high-field superconducting magnets, the very high stored energy per unit volume of coil windings requires a fast action, from quench initiation to a full effective protection, in order to avoid any damage or degradation caused by the quench. The design of the quench protection system (QPS) is part of the design of superconducting high-field magnets. Typically when people talk about the protection of a magnet, the detection part is also included as they are closely associated. Different detection and protection means are found in the literature [28, 30]. Traditional and innovative detection and protection methods are both considered for CCT-type magnets. Their principles are presented in the following subsections.

### 1.6.1 Detection methods

A quench creates an increasing normal zone of the conductor (i.e., an increase of resistance) and an increase of temperature in the normal zone. Therefore a quench can be detected based on the change of voltage (or current), temperature, or pressure. The possible methods are voltage detection, current detection, optical detection, quench antennas, pressure gauges, acoustic detection, and stray-capacitance change monitoring. They are discussed in the following paragraphs.

#### Voltage detection

With a large amount of current in the cable, the resistive voltage rises. A quench is detected when the output voltage is above a pre-set threshold. A direct voltage measurement is shown in Figure 1.13a. The voltage taps connected to the coil give an imperfect result because both the voltage on the rising quench resistance and the inductive voltage of the coil are measured. A more precise knowledge is required for analysis.

One can also measure the rising voltage with inductive compensation. The most conventionally used method is a comparative measurement, shown in Figure 1.13b. The subtraction of the voltage from the mid-coil to one lead and the voltage from the mid-coil to the other lead can cancel out the main inductive signals of two parts of the coil. However, this method cannot cancel out the noise from both coil parts. In addition, the inductive voltage may effectively hide the resistive voltage or lead to an erroneous trigger in the absence of a quench.

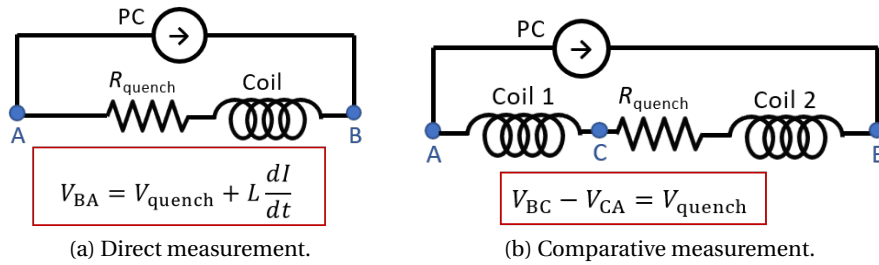


Figure 1.13 – Principle of direct and comparative voltage-based detection.

In order to measure purely the voltage on the rising quench resistance, one can connect the voltage taps to a co-wound copper wire. The wires are wound in anti-series to cancel out the effects of the magnetic field and noise, as shown in Figure 1.14a. The position of the co-wound copper wire inside the channel is illustrated in Figure 1.14b.

The voltage-based detection time depends on the longitudinal and transverse heat propagation velocity in the coil during a quench, which can be predicted in a 3D simulation, explained in Subsection 3.2.2. The voltage detection method is a straightforward way, nevertheless, the measurements are affected by flux jumps and electromagnetic fluctuations. To be precise, a flux jump is an avalanche of flux flow caused by a flux motion due to a breakdown of a pinning

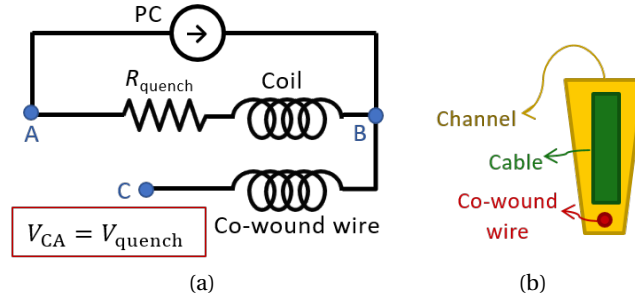


Figure 1.14 – Principle of voltage-based detection using a co-wound copper wire. (a) Electrical circuit; (b) Wire position inside the channel (not-to-scale).

site in the Low-Temperature Superconductor (LTS) materials, while the electromagnetic fluctuations are the motion of electrically charged particles inside materials caused by a fluctuating electromagnetic field. A validation time is compulsory to avoid any false trigger in this kind of detection. This extra time needs to be minimized or even suppressed.

### Current detection

The current detection relies on a co-wound superconducting wire, which is insulated from the cable (Figure 1.14b). The insulation can be realized by a mica sheet separating the cable and the wire. An alternative approach is in the absence of mica, the superconducting sensing wire could be ceramically insulated, provided sufficiently robust insulation can be found. In the case of a quench in the superconducting cable, a transverse heat propagation quenches the sensing wire after a certain delay in the millisecond range, explained in Section 4.2. This detection delay time depends on the heat propagation speed from the cable to the co-wound wire through insulation, which can be studied in detail in the simulation.

When the sensing wire is powered by a constant voltage source, the rise of quench resistance of the superconducting wire leads to a drop in current, which can be directly measured ( $I$ ) and also detected by a current derivative sensor ( $dI/dt$ ). The electrical circuit of the principle is presented in Figure 1.15. In this connection way, the current in the sensing wire does not produce any field on the beam. In addition, the inductive disturbance on the sensor is compensated by running current in an opposite direction than the coil.

As we run a small current (several ampere) in the co-wound sensing circuit, the heating produced during the current discharge should not be an issue. Nevertheless, the power supply of the co-wound sensing circuit could be switched off after a quench detection for safety considerations. The presumed advantage of this method is that the sensing of the loop current is localized and can be electromagnetically shielded. It is, thus, presumed to be less impacted by flux jumps and electromagnetic noise on the coil.



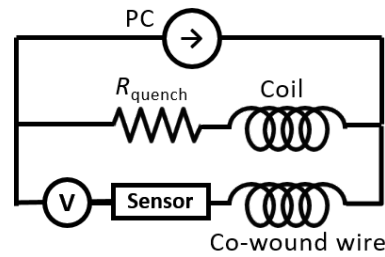


Figure 1.15 – Electrical circuit of current-based detection.

### Optical detection

The optical detection uses Rayleigh backscattering interrogated optical fibers (RIOF) [31, 32]. The position of the co-wound optical fiber inside the channel is illustrated in Figure 1.14b. The principle relies on the measurement of spectral shift (i.e., the deviation between a measurement and a reference condition), based on Rayleigh backscattering spectra, containing information of temperature and strain. From the perspective of photon interactions with matter, all of the defects (e.g., density fluctuations, voids, and impurities) are scattering centres for Rayleigh scattering. Some scattering events result in backscattering and are used to calculate the spectral shift as a function of fiber length. The swept wavelength interferometry is used to measure the spectral shift.

The optical fibers can detect any thermal or mechanical perturbation and to locate hot-spots. The validation time is not mandatory in this case because the measurements are not affected by electromagnetic noise (i.e., time-varying magnetic field). The quench delay time is therefore reduced (but the processing time may be longer, in the order of millisecond). The optical detection method has so far only been employed and tested in High-Temperature Superconductors (HTS). PSI has discussed with North Carolina State University (NCSU) to investigate the usage of an optical fiber for LTS, e.g., a  $\text{Nb}_3\text{Sn}$  CCT magnet.

There are two modes to configure the fiber working conditions. The first mode is a detection mode. A fast scan of the whole cable checks any perturbation. A heat deposition should be detected by an external analyzer (swept wavelength interferometry) within around a millisecond. In this mode, the spatial resolution is not necessary. Validation time should be eliminated. The second mode is a scanning mode. After a quench detection, a detailed scan is performed with spatial resolution in the order of a centimeter to find the hot-spot location in the magnet. The fibers are connected to the analyzer which can produce a qualitative picture of the temperature profile along the coil.

### Other detection methods

Four additional detection methods are briefly outlined.

A quench antenna is a device using arrays of pick-up coils lined up along the aperture of the magnet [33]. The inductive pick-up coils can detect a current redistribution in the quenching cable. Quench antennas are mainly used to localize the origin of quench since they are too sensitive to perturbations to use them as a detector. Figure 1.16 shows a linear array PCB antenna, implemented on the CCT2 at LBNL [34]. The quench antenna was successfully tested, however as it was installed on the outer layer of the coil, only the quench signals from the outer layer were captured. An inner-layer quench antenna is necessary if this method is considered for the test of a CCT-type magnet.

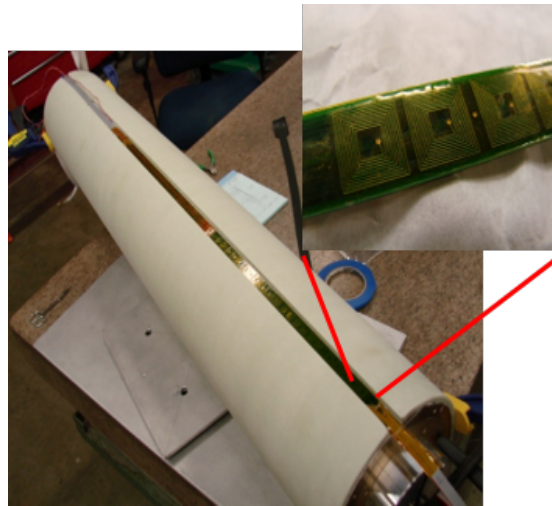


Figure 1.16 – Linear array PCB antenna for quench localization, implemented in the CCT2 at LBNL.

Pressure gauges detect a change in pressure due to the thermal expansion in the hot-spot. The limitation is that a large number of gauges are needed to have a fast detection. Thus the pressure gauges are not suitable for quench detection in a CCT-type magnet.

Acoustic detection uses amplified piezoelectric transducers, in combination with fast data acquisition and processing techniques, for detecting mechanical vibrations in superconducting magnets. This acoustic sensing technique has been tested on the LARP high-field  $\text{Nb}_3\text{Sn}$  quadrupole HQ01 [35]. The recorded acoustic data showed a good correlation with voltage instabilities measured simultaneously in superconducting magnets during ramping, quench and recovery [36]. The inexpensive acoustic sensors are easy to be installed on the magnet and they are not sensitive to the magnetic field. Therefore this method can be easily adapted to various magnet configurations. Nevertheless, the interpretation of the acoustic data is a challenging problem, requiring further development of the acoustic technique, especially on improving sensitivity, developing instrumentation and software for precise localization of the sound sources, and quantifying energy release in the detected acoustical events. Acoustic detection is a good approach for quench diagnostics in a CCT-type magnet.

A new detection technique based on stray-capacitance monitoring is proposed in [37] for HTS

magnets. The principle is to monitor the capacitance change, due to the variation of electrical permittivity of the cryogenic fluid impregnating insulation layers between coil parts, to obtain an indication of local heat deposition in the conductor. This technique was successfully tested on three small-scale Bi-2212 magnets manufactured at LBNL [38]. This method offers high sensitivity to heat deposited in the coil. However it is particularly promising for HTS magnets operated in cryogenic liquid since the critical temperature of HTS is well above helium boiling temperature, and thus a significant change of stray-capacitance is expected. For this reason, the method is not applied in a CCT-type magnet using Nb<sub>3</sub>Sn LTS.

### 1.6.2 Protection methods

A quench leads to a fast temperature increase in the coil as a large amount of energy stored, of the order of magnitude of mega-joule, is released. The action of turning off the power source is far and away not quick enough to protect the coils because the hot-spot temperature increases with time before the current turns to zero. Thus the current should decay as quickly as possible to avoid any damage in the coil.

There are two ways to protect the magnet. The first way is called passive protection. We extract the stored energy on a dump resistor  $R_{EE}$ , which is connected in series with the magnet. After a quench detection, the magnet can be electrically modeled as an  $LR$  circuit. The current in the coil is thus given by

$$I(t) = I_0 e^{-t \frac{R_{\text{quench}}(t) + R_{EE}}{L(t)}} \quad (1.4)$$

where  $I_0$  is the initial current. The second way is called active protection. We maximize  $R_{\text{quench}}$  to decrease  $I$  for minimizing Joule heating. The current in the coil can be written as

$$I(t) = I_0 e^{-t \frac{R_{\text{quench}}(t)}{L(t)}} \quad (1.5)$$

By quenching the entire coil volume, one can increase the quench resistance in the coil and distribute heat dissipation quickly across the magnet. Four different protection methods, energy extraction, Coupling-Loss Induced Quench (CLIQ) system, inductive protection, and heater strip, are discussed in the following paragraphs. In this document, only the energy extraction is considered as a passive protection method, while the others are considered as active protection methods<sup>3</sup>.

#### Energy-extraction system

The energy-extraction system dissipates the magnet's energy in a dump resistor  $R_{EE}$ . The dump resistor is added in series with the magnet, illustrate in Figure 1.17, making the method

<sup>3</sup>Note that there is an ambiguity on the type (active or passive) of the energy extraction with a switch. It is considered to be active, as the switch needs to be actuated. It is considered to be passive, as the main component is a passive resistor.

suitable for a single-magnet system. When the switch is closed, we are in normal operation. When the switch is open, we initiate the energy-extraction system after a quench detection. The energy extraction is the basic safety method for R&D magnets on a test bench. However, this method is difficult to implement when several magnets are powered in series. In an energy-extraction system, the value of the dump resistor and the current decay time, are limited by the maximum voltage-to-ground  $V = R_{EE} \cdot I$ .

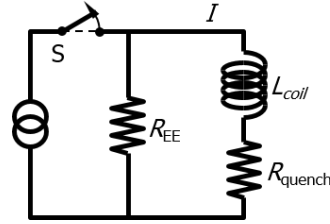


Figure 1.17 – Electrical circuit of energy-extraction system.

### Coupling-Loss Induced Quench method

The CLIQ system was recently developed [39]. The electrical circuit is illustrated in Figure 1.18. The essential part of CLIQ is a capacitive discharge unit. Once a quench is detected, the CLIQ system starts working by inducing current oscillations in the coil, resulting in a change in the local magnetic field, which introduces high Inter-Filament and Inter-Strand Coupling Losses (IFCLs and ISCLs). Hence the varying magnetic field heats up a large portion of the coil. With the CLIQ system, the heat is generated directly in the conductor, leading to a fast quench initiation. However, an analysis of additional mechanical stress due to the introduced current is required. Furthermore, if the CLIQ concept is applied to a chain of magnets, detailed studies have to be done to investigate the implementation means, transient waves, resonances, etc [40].

The CLIQ system is the protection baseline method for the FCC dipole magnets according to the conceptual design report [5]. The reasons are described as follows. The protection study of another three 16 T dipole magnet candidates for FCC, i.e., cos-theta- [43], block- [44] and common- [45] coil type magnet, is presented in [46], using either CLIQ or traditional quench heaters or both of them. In the case of a CCT-type magnet, CLIQ promises fast protection because it shows that at nominal operation current, the performance of CLIQ is more efficient in terms of peak temperature reduction than the case of heaters. The study of CLIQ for the two-layer CCT magnet CD1 is presented in Section 3.3.

### Inductive protection method - co-wound copper tape

In a CCT-type magnet, a co-wound copper tape, placed beneath the cable in the channel (Figure 1.19a), can be seen as a secondary  $LR$  circuit, which is inductively coupled to the magnet coil (Figure 1.19b). When a quench occurs in the primary loop, the variation of current

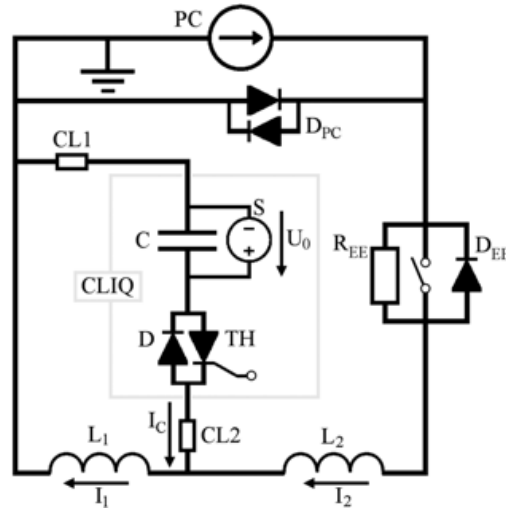


Figure 1.18 – Electrical circuit of CLIQ system (Figure from [39]).

induces a voltage in the secondary. The secondary circuit removes a portion of the magnet energy and dissipates it in a low-cost copper tape. Heat in the secondary circuit can also be supplied back to the coil to quench its superconducting fraction: an effect that is called "quench back". The aim to make a compact magnet by adding a co-wound copper tape. This study is presented in Section 3.4 for the two-layer CCT magnet CD1.

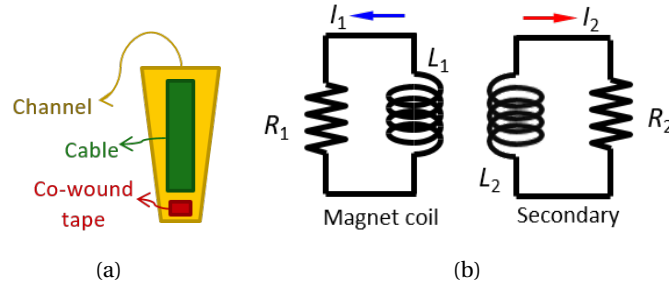


Figure 1.19 – Principle of inductive protection using a co-wound copper tape. (a) Position in the channel (not-to-scale); (b) Electrical circuit.

### Quench heaters

Heaters are thin foil strips placed (usually epoxy-impregnated) on the top of windings. This method relies on the thermal diffusion across insulation layers, whereby the protection delay is determined by the insulation thickness and material. By heating up the coil, the normal conducting zone expands quickly. A large normal conducting volume results in a low energy density in the coil. In this way, a low peak temperature is obtained. However quench heaters may cause electrical shorts and get damaged during magnet assembly, cool-down, or powering. Furthermore, in a CCT-type magnet, their installation is not optimal due to the large exterior

coil surface that is covered by the winding former, as illustrated in Figure 1.20.

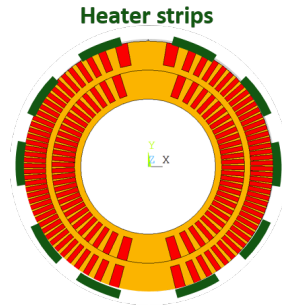


Figure 1.20 – Illustration of heater strips installed on the outer layer of a two-layer CCT coil.

### 1.7 Thesis objectives

Following the EuroCirCol's (European Commission funded European Circular) guideline and according to the quench protection analysis for the FCC [49, 50, 51, 52], the maximum allowed values in the system during a quench are 350 K for the peak temperature and 2 kV for the voltage to ground. In order to safely dissipate the very high stored magnetic energy in the coil windings and to protect the magnet against the consequences of a quench (cable degradation or even coil destruction), we need a fast and reliable detection and a fast and efficient discharge to prevent overheating of the magnet.

The characteristics of a protection system depend on diverse factors: the superconducting cable composition (copper to non-copper ratio), the magnet geometry (inductance, shape of the coil), the magnetic energy, and the operating conditions (temperature, field, current ramp rate). In the case of a CCT-type magnet, these topics have not yet been explored in detail. Therefore the topic of quench protection deserves a meticulous study.

My thesis research program covers three main parts for the CCT magnet detection and quench problem: simulation methods, detection and protection concepts, as well as experimental work. On one hand, I work on the multiphysics simulations in order to predict the real electrothermal behavior of the magnet. On the other hand, different approaches to detect a quench and to protect the magnet are studied. I implement and use generic simulation methods to qualify different protection concepts. The new User-Defined-Elements (UDEs) in ANSYS APDL, developed at LBNL [53, 54, 55], are adapted and used in the quench simulation models. Based on the simulation results, the appropriate detection and protection methods are selected and developed for testing. One method is tested in the subscale experiments and others are to be tested on a two-layer CD1 model magnet that was built over the thesis period at PSI. The results allow us to validate the conceptual design and feasibility of the construction of a reliable, robust, fast, and efficient quench detection and protection system for a two-layer CCT magnet.

In this document, Chapter 2 focuses on the general simulation methods used in the quench study. Chapter 3 presents the simulation studies of different quench protection methods, e.g., energy extraction, CLIQ and co-wound copper tape, using the example of the two-layer CCT-type magnet CD1. Chapter 4 presents the experimental studies of different quench detection methods. The voltage detection and optical detection techniques are tried out on the CD1 model magnet. The current detection method is investigated in a subscale experiment.





## 2 Simulation Methods

### 2.1 Overview

The quench phenomenon is a multiphysics problem. The simulations are usually performed by Finite Element Analysis (FEA), such as ANSYS [53], COMSOL Multiphysics [56] or network models, such as ROXIE [57], Thea [58], LEDET [59], etc. MATLAB [60] and Excel spreadsheets are also used to compute some simple approximations. ANSYS Mechanical APDL (ANSYS Parametric Design Language), a scripting language to build models and analyses in terms of parameters, is selected as the principal working tool due to the use of ANSYS for mechanical models, a collaboration with LBNL, as well as the license availability at PSI.

ANSYS is an adequate and promising tool for quench simulation in superconducting magnets by combining electrodynamics, thermal, mechanical, and possibly fluid dynamics analysis [61]. Different phases in a quench can be studied in a detailed way, with standard ANSYS features (magnetostatic, heat-flow at a constant field, conventional eddy-currents). For example, a quench propagation can be modeled in order to investigate the detection and validation phase. Nevertheless, ANSYS is still not a perfect quench simulation tool since at present it does not support multi-dependency material properties and does not include the effects of inter-filament coupling currents [62, 63, 64]. These features are necessary to simulate the full quench evolution, in particular the discharge phase.

One of ANSYS' capabilities is the user-programmable feature, which allows implementing custom commands, material laws, and also complete new elements. At LBNL, the 2D thermal and electromagnetic User-Defined Elements (UDEs) are developed in ANSYS for quench simulations to include the missing features mentioned above: the multi-dependency material properties and the losses of inter-filament coupling currents [55]. The purpose of developing these UDEs is to improve simulation accuracy and performance. The performance of these ANSYS elements have been verified via a benchmark study, showing a good agreement, between the new elements and a COMSOL Multiphysics implementation developed at CERN on a simple-geometry Nb<sub>3</sub>Sn block dipole, using a dump resistor and coupling-loss induced quench (CLIQ) based magnet protection approaches. Furthermore, with these elements,

ANSYS reproduced the strong coupled quench back behavior, observed during the test of a Nb<sub>3</sub>Sn superconducting undulator prototype at LBNL [55].

As far as the CCT-type magnet is concerned, the unique geometry has already been created in ANSYS APDL and can be used for different types of simulations [11, 23, 65], e.g., quench simulation. In order to determine the realistic dynamic behavior of the coil during a quench, it is worthwhile to investigate the coupled problem in the electrical circuit, the electromagnetic, and the electrothermal domains. The simulation methods are applied to our CCT-type model magnet for test and validation. Nevertheless, by their nature, they are also generic for all other types of superconducting magnets.

There are two major original contributions on the simulation side. The first one is the adaption of UDEs in order to account for particular geometry effects that are inherent to the modeling in 2D of CCT-type magnets. The second one is the creation of an automated Mathematica-generated ANSYS quench model generator [66], with UDEs, for superconducting magnets using Nb<sub>3</sub>Sn Rutherford cables. The implementation of the setup of the UDE-based model in a model-generation software makes the work useful for future projects and simulations in the wide superconducting magnet community.

In this chapter, the simulation models or techniques, covering all the phases of the quench process, are developed and explained in a hierarchical pattern from the simplest to the most sophisticated one. An overview of the simulation methods is given in Table 2.1. The model magnet CD1 introduced in Section 1.3 is used as an example in all of the calculation methods outlined in this chapter. The coupled quench model using UDEs is applied for the CCT4 model magnet, which was built and tested at LBNL. The comparisons between the simulation results and experimental data are described at the end of this chapter in order to validate the coupled simulation method. It is worth noting that round strands are assumed in all the calculations. The simulation results using these simulation methods for CD1 are presented in Chapter 3.

Table 2.1 – Overview of simulation methods.

| Simulation method                             | Direct output and purpose   |
|---|---|
| MITs adiabatic calculation                    | $t_d$ budget or $T_{peak}$ estimation   |
| Adiabatic integrator                          | $R_{quench}$ for calculation of a rising voltage during detection phase or a current decay  |
| 3D magnetostatic/thermal model                | Temperature profile along the cable for determination of a voltage-based $\Delta t_{thres}$ |
| 2D magnetoquasistatic/thermal model with UDEs | Current profile in the coil for a CLIQ and/or EE protection study                           |

## 2.2 MIITs adiabatic calculation

MIITs is an essential parameter in superconducting magnet design. MIITs stands for M (Mega) I (current) I (current) T (time) s (plural). MIITs is used to link a current profile during a quench (from the current plateau or ramp after a quench initiation to the end of the current decay) to a peak temperature for a given cable type under adiabatic conditions [67]. MIITs calculation is a reliable conservative estimate in a fast way for the peak temperature after a quench or the total time budget before the current discharge. In this section, for a given superconducting cable, the equation of total time budget to detect and actuate the protection after a quench is outlined, using a given time constant of the current decay function. This calculation helps us study the detection, validation and protection phases introduced in Section 1.5. MIITs calculation is applied in the following locations: Subsection 3.2.1, 3.2.3, 3.3.5, and Section 3.4.

### 2.2.1 MIITs calculation

The MIITs expression can be obtained starting from the heat-balance equation in adiabatic conditions:

$$c_v \frac{\partial T}{\partial t} = q_v \quad (2.1)$$

where  $c_v$  is the volumetric specific heat;  $T$  the temperature;  $t$  the time;  $k$  the conductivity and  $q_v$  the volumetric heat source, e.g., Joule losses, in the coil.

Joule losses start when current flows into stabilizer (i.e.,  $T > T_{cs}$ ):

$$P = I^2 R = I^2 \rho \frac{l}{A} = \rho \frac{I^2}{A^2} l A = \rho J^2 V \quad (2.2)$$

where  $P$  is the power source;  $I$  the current;  $R$  the resistance;  $\rho$  the resistivity;  $l$  the length;  $A$  the cross-section area;  $J$  the current density and  $V$  the volume.

Therefore the volumetric heat source  $q_v$  equals  $\rho J^2$ . Eq. (2.1) becomes:

$$\rho_{cu}(T, B) J_{cu}^2(t) dt = c_v(T, B) dT \quad (2.3)$$

where  $\rho_{cu}$  is the copper resistivity and  $J_{cu}$  the current density in the copper. It is worth noting that only copper resistivity is considered as the resistivity of other cable components are considerably higher than the one of copper. Therefore their contributions are negligible in a parallel connection. More explanation is given in Subsection 2.4.2.

The copper resistivity is computed as follows [68]:

$$\rho(T, RRR) = 10^{-8} \left[ \frac{1.7}{RRR} + \left( \frac{2.32547 \cdot 10^9}{T^5} + \frac{9.57137 \cdot 10^5}{T^3} + \frac{1.62735 \cdot 10^2}{T} \right)^{-1} \right] + MR \cdot B \quad (2.4)$$

## Chapter 2. Simulation Methods

where  $T$  is the temperature and RRR the residual resistivity ratio. The term  $MR \cdot B$  is the magnetoresistivity with  $MR = 0.5 \cdot 10^{-10} \Omega \cdot m/T$ .

The RRR is defined as the ratio between the resistivity at a high temperature  $T_h$  and a low temperature  $T_l$  at zero field:

$$RRR = \frac{\rho(T_h, B = 0 \text{ T})}{\rho(T_l, B = 0 \text{ T})} \quad (2.5)$$

In the model, the coefficients are selected for  $T_l = 4 \text{ K}$  and  $T_h = 290 \text{ K}$ .

For MIITs calculation to work, we have to choose one  $B$ -field value and keep it constant, which is a wrong assumption during the current decay. To be conservative, the peak  $B$ -field value is chosen to compute material properties. The following equation is obtained after integration:

$$\int_0^\infty I^2(t) dt = f_3 A^2 \int_{T_0}^{T_{\max}} \frac{c_v(T, B)}{\rho_{cu}(T, B)} dT = F(T_{\max}) \quad (2.6)$$

where  $I$  is the magnet current;  $A$  the cable cross section;  $T_0$  the operating temperature;  $T_{\max}$  the maximum temperature in the system and  $c_v$  the average volumetric specific heat of the cable across copper, superconductor and resin, which is given by

$$c_v = f_1 c_{v, \text{res}} + f_2 c_{v, \text{sc}} + f_3 c_{v, \text{cu}} \quad (2.7)$$

The fractions of different components are defined as

$$f_1 = 1 - f_{\text{cond}} = \frac{A_{\text{res}}}{A_{\text{cab}}} \quad (2.8)$$

$$f_2 = f_{\text{cond}} f_{\text{sc}} = \frac{A_{\text{sc}}}{A_{\text{cab}}} \quad (2.9)$$

$$f_3 = f_{\text{cond}} (1 - f_{\text{sc}}) = \frac{A_{\text{cu}}}{A_{\text{cab}}} \quad (2.10)$$

$f_1$ ,  $f_2$  and  $f_3$  are respectively the cross-section area fraction of the resin, superconductor and copper in the cable area.  $f_{\text{cond}}$  is the conductor fraction in the cable area.  $f_{\text{sc}}$  and  $(1 - f_{\text{sc}})$  are respectively the fraction of superconductor and copper within the conductor area.

### Example:

The fraction calculations are explained using the CD1 parameters listed in Table 1.3. The multiplication of cable thickness and cable width gives the cable area  $A_{\text{cab}} = 14.53 \text{ mm}^2$ . The conductor area in the cable area is the sum of all the round-strand areas, which is  $11.92 \text{ mm}^2$ . Thus we have  $f_{\text{cond}} = 11.92/14.53 = 0.82$  and  $f_1 = 0.18$ . The resin area in the cable area is the difference between the cable and conductor  $A_{\text{res}} = 2.61 \text{ mm}^2$ . The non-Cu fraction is the fraction of superconductor within the conductor area  $f_{\text{sc}} = 0.465$ . Therefore we obtain  $A_{\text{sc}} = 5.54 \text{ mm}^2$ ,  $A_{\text{cu}} = 6.38 \text{ mm}^2$ ,  $f_2 = 0.38$ , and  $f_3 = 0.44$ .

The calculation of MIITs gives:

$$\text{MIITs} = 10^{-6} \int_0^{\infty} I^2(t) dt = 10^{-6} \left( I_{\text{op}}^2 t_d + \int_{t_d}^{\infty} I^2(t) dt \right) \quad (2.11)$$

with  $t_d = \Delta t_{\text{thres}} + \Delta t_{\text{val}} + \Delta t_{\text{switch}}$ , as illustrated in Figure 1.12.

The final formulation is obtained from inserting the MIITs expression into Eq. (2.6) and solving for a maximum temperature.

$$F^{-1} \left( \int_0^{\infty} I^2(t) dt \right) = T_{\text{max}} \quad (2.12)$$

The function is used to yield a worst-case estimate of the hot-spot temperature for a given current decay.

### Example:

For a maximum allowed temperature of 350 K [69], the MIITs number at 8.9 T should be smaller than 10.7 MA<sup>2</sup>s, calculated from the material properties of the superconducting cables used in CD1, given in Table 1.3. The plot of peak temperature versus MIITs values at  $B = 8.9$  T for CD1 is shown in Figure 2.1.

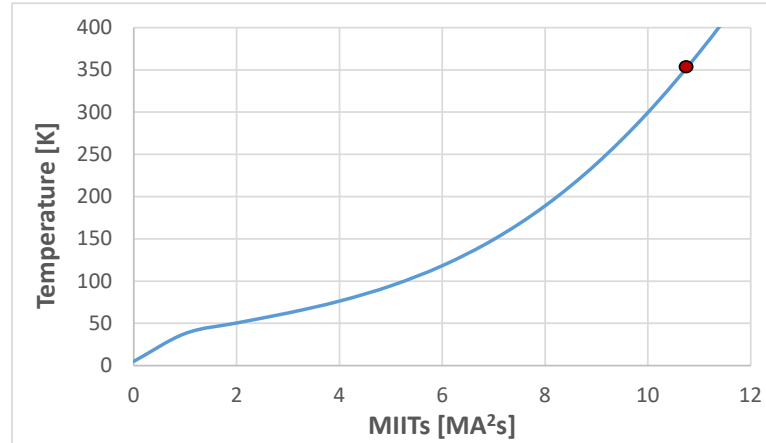


Figure 2.1 – Peak temperature versus MIITs values at  $B = 8.9$  T for the CD1 cable.

### 2.2.2 Time budget estimation

The time budget before current decay can be calculated from Eq. (2.11) as follows:

$$t_d = \Delta t_{\text{thres}} + \Delta t_{\text{val}} + \Delta t_{\text{switch}} = \frac{F(T_{\text{max}}) - \int_{t_d}^{\infty} I^2(t) dt}{I_{\text{op}}^2} \quad (2.13)$$

with

$$I(t) = I_0 e^{-t \frac{R_{EE} + R_{\text{quench}}(t)}{L(I)}} \quad (2.14)$$

Since  $R_{EE} \gg R_{\text{quench}}$ , if only considering the dump resistor in the circuit, the current expression can be simply written as follows

$$I(t) = I_0 e^{-t \frac{R_{EE}}{L(I)}} \quad (2.15)$$

### 2.2.3 Current decay expression

The knowledge of current decay function is necessary for computing MITs calculation. Once the quench is detected and the power supply is switched off, the equation in the loop can be written as

$$L_d(I) \frac{dI(t)}{dt} = -(R_{EE} + R_{\text{quench}}(t))I(t) \quad (2.16)$$

Note that the lead resistance is neglected here.

The dump resistor value is determined by the maximum operating current and the maximum voltage rating of the test station equipment and the magnet's ground insulation.

#### Example:

For a test of CD1 magnet at LBNL, we have  $V_{\text{max}} = 800 \text{ V}$  [70] and  $I_{\text{max}} = 18.1 \text{ kA}$ . The dump resistor value can be estimated as:

$$R_{EE} = \frac{U}{I} = \frac{800 \text{ V}}{18.1 \text{ kA}} = 44 \text{ m}\Omega \quad (2.17)$$

Without any consideration of active protection ( $R_{\text{quench}}$ ), the current decay function is computed numerically via:

$$I_n = I_{n-1} - \Delta t \frac{R_{EE}}{L(I_{n-1})} I_{n-1} \quad (2.18)$$

where  $\Delta t = t_n - t_{n-1}$  and  $I_n = I(t_n)$  with small steps. Note that the inductance  $L$  has a dependence on the current  $I$ . The inductance profile needs to be included to get a realistic current decay function.

### 2.2.4 System inductance

A magnetostatic model was solved beforehand in Opera [81], to calculate the energy of CD1 full model at several different current levels. From that, the differential inductance is derived.

The total energy is

$$W = \int_0^\varphi I d\varphi = \int_0^I I \frac{d\varphi}{dI} dI = \int_0^I L_d I dI \quad (2.19)$$

where  $\varphi$  is the linked magnetic flux in the magnet coil and  $L_d$  is the differential inductance. If we rewrite Eq. (2.19), it becomes

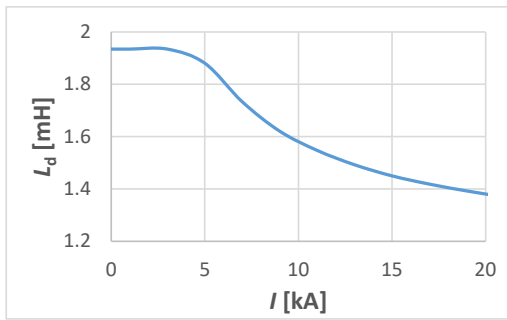
$$\Delta W = L_d(\bar{I}) \bar{I} \Delta I \quad (2.20)$$

where  $\bar{I}$  is the average current for two adjacent values with small steps. The differential inductance function is computed from consecutive energy values via

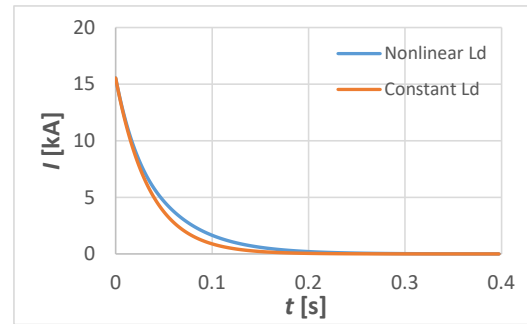
$$L_d(\bar{I}) = \frac{\Delta W}{\bar{I} \Delta I} \quad (2.21)$$

### Example:

Figure 2.2a shows the differential inductance value as a function of current for CD1. At the beginning of discharge  $L_d = 1.4$  mH while at the end of discharge  $L_d = 1.9$  mH. If we substitute  $L$  in Eq. (2.18) by Eq. (2.21), the current decay is obtained as well as the MIITs value for the decay part. Figure 2.2b plots the current discharge when power supply is switched off at  $I_{op} = 15.5$  kA, using a nonlinear  $L_d$  or a constant  $L_d = 1.4$  mH. The MIITs value for both cases is respectively 4.8 and 4.2 MA<sup>2</sup>s. From this figure, we remark a slight difference in the current decay. It is more conservative assuming  $L_d = 1.4$  mH to compute the time budget available before discharge. The usage of a nonlinear  $L_d$  is mainly to make the simulation more realistic.



(a) CD1 inductance in 3D full model.



(b) Current discharge curve.

Figure 2.2 – CD1 differential inductance and comparison of current decay profile with/without  $L_d(I)$ , when the CD1 is protected by a dump resistor of 40 mΩ, without consideration of quench resistance.

### 2.3 Adiabatic integrator

An adiabatic integrator assumes a time of quench for each turn. The quench resistance is computed via adiabatic integration of the temperature in each turn. When a temperature profile in the superconducting cable centre is available, the resistivity of the normal zone, its quench resistance as well as the voltage rise in the magnet can be calculated as a function of time. This calculation helps us study the detection and discharge phase introduced in Section 1.5. The adiabatic integrator is applied in Subsection 3.2.2 and 3.4.

For each mesh element of the cable in the model, a fixed temperature  $T_e$ , a constant magnetic field across the coil, a constant cable cross-section area and a discretization length  $\Delta x$  are assumed to calculate the quench resistance. The current-sharing regime is neglected here. An element is considered to be quenched when the element temperature is larger than  $T_{cs}$ . The element resistance is calculated as  $R_e = \rho_{cu}(T_e) \cdot \Delta x / A_{cu}$ .

The total quench resistance is the sum of all the resistances of the quenched elements, given by  $R_{\text{quench}} = \sum_i^n R_{e,i}$ . The voltage rise in the coil is written as  $V_{\text{quench}} = I_{\text{op}} R_{\text{quench}}$ . In the voltage detection method,  $V_{\text{quench}}$  is used to determine the quench detection time assuming that the inductive voltage is canceled out.

### 2.4 Magnetostatic and electrothermal finite-element model

In a magnetostatic and electrothermal model, the thermal diffusion and quench propagation in the coil are investigated at a fixed magnetic field (i.e., a fixed current), to study the longitudinal and turn-to-turn propagation. A magnetic-field map, that does not change over time, is implemented in the model. Based on the temperature profiles obtained in the simulated models, we aim to quantify the detection problem by evaluating the detection time for the voltage-based method, using the adiabatic integrator, described in Section 2.3. These models help us study the detection and validation phases in Section 1.5.

In the model, the quench is triggered by assigning a temperature profile that locally exceeds Nb<sub>3</sub>Sn critical temperature for a certain region in the superconducting cable. A 3D 3-turn helical model of CD1 cable on the inner layer is generated. In the simulation, we assume that the first turn is already quenched (20 K) and other turns are set at the operating temperature (4.2 K) as the initial conditions, since my interest is to observe the longitudinal and transverse quench propagation in a CCT-type magnet on the quench front. Figure 2.3 illustrates an example of a temperature profile on the cable and former in the coil at 15.5 kA after a simulation time of 10 ms. The results and discussions for CD1 are presented in Subsection 3.2.2. Note that the propagation velocity is best measured when the quench reaches the third turn, i.e., when the influence of the initial condition is no longer relevant.

Once the detection plateau, as well as the current decay is known, when the magnet is protected by the energy-extraction system, one can calculate the MIITs, described in Section 2.2,



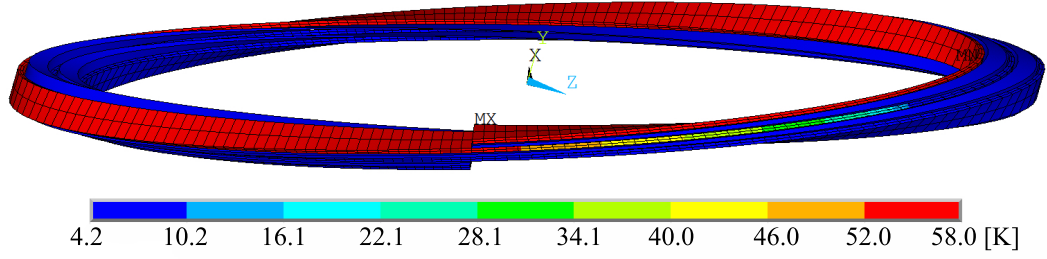


Figure 2.3 – Quench propagation illustration in the CD1 3-turn helical model at 15.5 kA after 10 ms. The cable insulation is not included in the figure for a better illustration of temperature profiles in the bare cable and former.

during a quench, in order to estimate the worst-case peak temperature in the conductor, explained in Subsection 3.2.3. Furthermore, the voltage-based detection time can be used in other quench protection simulations, e.g., when we combine the detection time with the CLIQ unit, explained in Subsection 3.3.4. Additionally, the voltage-based detection time can be used to compare with other detection methods, e.g., current-based method, explained in Subsection 4.2.7.

The following subsections concentrate on the different aspects of the modeling. The 3D coil geometry is first generated with the model general settings. Then all the material properties involved are added into the code, as well as the critical current fit functions of the superconductor. The real magnetic-field map is implemented and associated with corresponding finite elements.

### 2.4.1 Model geometry and general settings

In Figure 2.4a, different components (cable representing  $\text{Nb}_3\text{Sn}$ , copper and resin, insulation in G10, spar and rib in aluminum bronze) are observed in a superconducting cable of a 3-turn helical model of CD1 inner layer. Finer meshes are applied between turns for a better observation of transverse propagation in a quench propagation simulation (Figure 2.4b).

The time substep in ANSYS, as well as the mesh size, depend on the geometry and the physics (material parameters, excitation, etc.). The total simulation duration is set differently depending on the current levels. A finer mesh or a smaller time substep means a longer simulation running time. In order to guarantee convergence, the mesh size and time substep are chosen as large as possible and as small as necessary.

### 2.4.2 Material properties and homogenization

Material properties from different sources are used [68], e.g., MATPRO [72], NIST [73], CUDI [74], CryoComp [75], LBNL, and Fermilab. In my study, the temperature range of interest for quench simulation is from 4 to 350 K. The different types of material properties are used, e.g.,

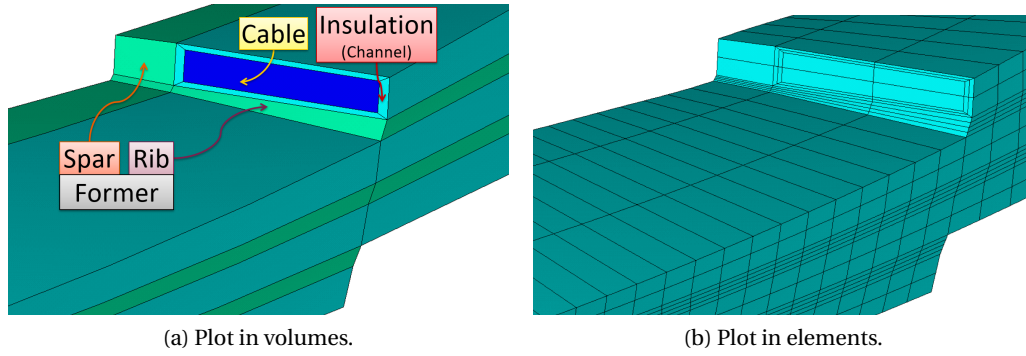


Figure 2.4 – ANSYS plots of a 3-turn helical model of the CD1 inner layer, illustrating model geometry and meshing.

electrical resistivity  $\rho$  [ $\Omega \cdot \text{m}$ ], thermal conductivity  $k$  [ $\text{W}/(\text{K} \cdot \text{m})$ ], mass density  $d$  [ $\text{kg}/\text{m}^3$ ], and specific heat  $c$  [ $\text{J}/(\text{K} \cdot \text{kg})$ ] or volumetric heat capacity  $c_v = d \cdot c$  [ $\text{J}/(\text{K} \cdot \text{m}^3)$ ]. The following considerations are taken into account in the modeling.

We only consider the copper electrical resistivity in the simulation because the electrical resistivity of the other cable components are considerably higher than the one of copper, thus their contributions are negligible in a parallel connection. For example, according to MATPRO, the normal-state electrical resistivity of  $\text{Nb}_3\text{Sn}$  is in the range of  $2.3 \cdot 10^{-7} \sim 4.1 \cdot 10^{-7} \Omega \cdot \text{m}$ , where the lower value is for cryogenic temperature (4.2 K) and the higher value for room temperature (295 K). While the copper resistivity is about  $1.7 \cdot 10^{-8} \Omega \cdot \text{m}$  at room temperature (290 K), and is 100 to 200 times lower at cryogenic temperature. Thus there is at least more than one order of magnitude of difference between the resistivity of  $\text{Nb}_3\text{Sn}$  and copper.

To calculate the longitudinal propagation of heat through the cable, only copper is considered. The reason is the same for the electrical resistivity. For example, according to MATPRO, the maximum thermal conductivity of  $\text{Nb}_3\text{Sn}$  is  $2.8 \text{ W}/(\text{K} \cdot \text{m})$  and the thermal conductivity of copper is bigger than  $100 \text{ W}/(\text{K} \cdot \text{m})$ . For the calculation of transverse propagation of heat (between different turns), the material properties of the ribs from former and the cable are involved.

The change in mass density due to thermal expansion is neglected, because the warm geometry is used, so the contraction is neglected. In addition, it seems to be quite small. For example, the copper density decreases about 1.33% from room to cryogenic temperatures [76] and  $\text{Nb}_3\text{Sn}$  has even a smaller thermal expansion than copper [77].

Table 2.2 specifies the source of material property for each type material used in the simulation. This table is also valid for the simulation described later in Section 2.5. In a quench propagation simulation, only the material properties of copper,  $\text{Nb}_3\text{Sn}$  G10, and aluminum bronze are involved. For the simulation in Section 2.5, everything listed in the table is involved. It is worth noting that in the quench propagation model, the simplest Wiedemann-Franz law is used for

## 2.4. Magnetostatic and electrothermal finite-element model

calculation of copper thermal conductivity while a more precise database CUDI is used in the model in Section 2.5. Moreover, for simplicity, the epoxy regions in the cable are considered to be glassfiber reinforced due to a lack of material properties for pure epoxy. Thus the properties of G10 are assumed.

Table 2.2 – Source of material property for each type material used in the ANSYS FEM simulation.

| Material           | Property | Source                     |
|--------------------|----------|----------------------------|
| Copper             | $\rho$   | CUDI                       |
|                    | $k$      | Wiedemann-Franz law / CUDI |
|                    | $c_v$    | CUDI                       |
| Nb <sub>3</sub> Sn | $c_v$    | CUDI                       |
| G10                | $k$      | NIST                       |
|                    | $c$      | Fermilab                   |
| Aluminum bronze    | $k$      | LBNL                       |
|                    | $c$      | LBNL                       |
| Aluminum           | $k$      | NIST                       |
|                    | $c$      | NIST                       |
| Kapton             | $k$      | NIST                       |
|                    | $c$      | NIST                       |

In finite element analysis, the material properties are assigned to elements, and elements resolve the entire cable, which is assumed to contain resin, copper stabilizer and superconductor. The material properties are blended using area fractions for thermal conductivity  $k$  and volumetric heat capacity  $c_v$ . With all these assumptions the blended properties used are given by

$$k = f_3 k_{\text{cu}} \quad (2.22)$$

$$c_v = f_1 c_{v,\text{res}} + f_2 c_{v,\text{sc}} + f_3 c_{v,\text{cu}} \quad (2.23)$$

with the definition of fractions described in Subsection 2.2.1.

The generated volumetric heat is

$$q_v(T) = \frac{A_{\text{cu}}}{A_{\text{cab}}} \rho_{\text{cu}}(T) \left( \frac{I_{\text{op}} - I_{\text{sc}}(B, T)}{A_{\text{cu}}} \right)^2 \quad (2.24)$$

where  $A_{\text{cu}}$  is the copper area;  $A_{\text{cab}}$  the bare cable area; and  $I_{\text{sc}}(B, T)$  the current flowing in the superconductor.

### 2.4.3 Critical current fit function

As mentioned in Section 1.4, Nb<sub>3</sub>Sn is a strain-sensitive material, the large transverse forces can cause irreversible damage to the conductor, which happens in high-field magnets. In addition to large transverse forces, a relatively small longitudinal force can cause degradation. We know that a transverse stress below 130 MPa does not lead to a significant reduction in  $J_c$  and it avoids any irreversible degradation [13, 78]. For this reason, the CCT geometry using the Nb<sub>3</sub>Sn conductor can mitigate the issue related to the strain or stress management, because the expected peak coil stress is respectively 135 MPa at nominal field for the FCC CCT dipole magnet and 101 MPa at short sample step for the CD1 model magnet [11, 23]. Furthermore, the quench model is not coupled to a mechanical one, therefore the strain function is not included in the fit functions described in this subsection.

The Summers critical current fit function is given by [68]<sup>1</sup>:

$$B_{c2}(T) = B_{c20} \left[ 1 - \left( \frac{T}{T_{c0}} \right)^2 \right] \left\{ 1 - 0.31 \left( \frac{T}{T_{c0}} \right)^2 \left[ 1 - 1.77 \ln \left( \frac{T}{T_{c0}} \right) \right] \right\} \quad (2.25)$$

$$J_c(B, T) = \frac{C}{\sqrt{B}} \left( 1 - \frac{B}{B_{c2}(T)} \right)^2 \left[ 1 - \left( \frac{T}{T_{c0}} \right)^2 \right]^2 \quad (2.26)$$

where  $T_{c0}$  and  $B_{c20}$  are characteristics of the superconducting material.  $C$  is a normalization constant. The respective values are  $T_{c0} = 18$  K,  $B_{c20} = 28$  T and  $C = 3.7 \cdot 10^{10}$  A.T<sup>1/2</sup>/m<sup>2</sup>, obtained from the CD1 strand short sample measurement.

For numerical efficiency, i.e., in order to avoid numerically solving a nonlinear problem to compute  $T_{cs}$ , the below critical current fit function is implemented in the magnetostatic and electrothermal model [80]:

$$T_c(B) = T_{c0} \left( 1 - \frac{B}{B_{c20}} \right)^{0.59} \quad (2.27)$$

$$J_c(B, T) = (C_1 + C_2 B) \left( 1 - \frac{T}{T_c(B)} \right) \quad (2.28)$$

The Summers fit functions are replaced by this simplified version. For a selected operating point, the current-sharing temperature can be easily computed with this simplified version in Eq. (2.29).

$$T_{cs}(B) = T_c(B) \left( 1 - \frac{J_{op}}{C_1 + C_2 B} \right) \quad (2.29)$$

However it is impossible to get a perfect superposition of the standard (Eq. (2.25) and (2.26)) and the simplified (Eq. (2.27) and (2.28)) fit functions everywhere. Nevertheless if we also adapt  $T_{c0}$  and  $B_{c20}$  values in addition to the constant  $C_1$  and  $C_2$ , we are able to obtain the

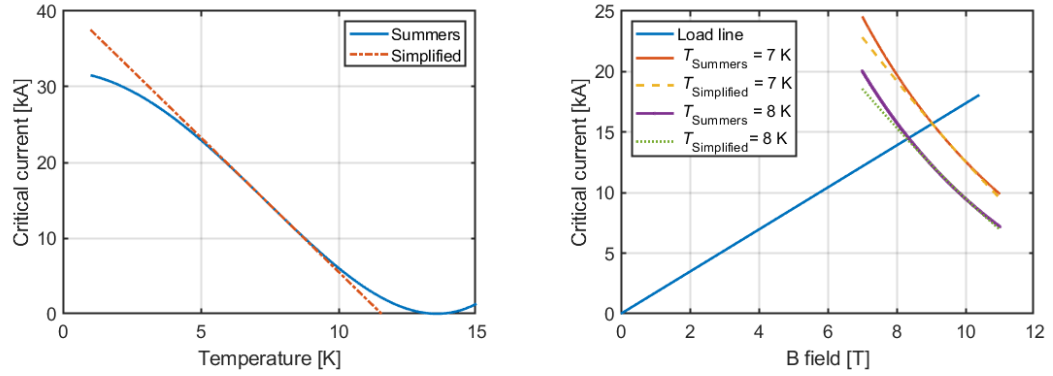
---

<sup>1</sup>A discrepancy of fit function exists between the original paper [79] and ROXIE document [68]. To be consistent with the superconducting magnet community, the critical current fit function in ROXIE is used in the calculations.

same results of critical current for the standard and simplified equations within a range of temperature and magnetic field (quench zone).

### Example:

Figure 2.5 shows an example when  $I_{op} = 15.5$  kA. Figure 2.5a plots the critical current as a function of temperature at a fixed magnetic field while Figure 2.5b plots the critical current as a function of  $B$  field at two different temperatures. In the figure, the linear (simplified) and curved (standard) lines are overlapped around  $T = 7.2$  K and  $B = 8.9$  T. These simplified critical functions may not be appropriate when we are at low  $B$  field. Nevertheless, since the quench propagation model is based on the cables turns in the inner layer of CD1, the  $B$  field range is approximately between 5 to 9 T at 15.5 kA.



(a) Critical current versus temperature at a fixed  $B$  field. (b) Critical current versus magnetic field at a fixed temperature.

Figure 2.5 – Comparisons of critical current fit functions between the Summers and the simplified version for the CD1 at 15.5 kA.

Finally, for computations of FCC magnets, the following fit function are suggested in [69]

$$C(t) = C_0(1 - t^{1.52})^\alpha(1 - t^2)^\alpha \quad (2.30)$$

$$B_{c2}(T) = B_{c20}(1 - t^{1.52}) \quad (2.31)$$

$$J_c = \frac{C(t)}{B_p} b^{0.5}(1 - b)^2 \quad (2.32)$$

where  $t = T/T_{c0}$ ,  $b = B_p/B_{c2}(t)$ , with  $B_p$  the peak field on the conductor. The following fit parameters are used, representing the target values for the FCC R&D wire:  $T_{c0} = 16$  K,  $B_{c20} = 29.38$  T,  $\alpha = 0.96$  and  $C_0 = 267845$  A/mm<sup>2</sup> for FCC CCT study [69].

### 2.4.4 Magnetic-field map implementation

In a magnetostatic model, the magnetic field changes with location, and the value of the magnetic field impacts some material properties, e.g., electrical resistivity, specific heat. Therefore

the  $B$ -field map needs to be imported in ANSYS. Since the mesh discretization is done in ANSYS, the centroid coordinates of each element are extracted from the model built. Then the corresponding  $B$ -map table is extracted from an Opera model, based on the element centroid coordinates (Figure 2.6). Finally, the  $B$  value is rescaled with the operating current and assigned to each element in the ANSYS model. The scaling law used is as follows  $B = I \cdot B_d / I_d$ , where  $d$  denotes magnetic design.

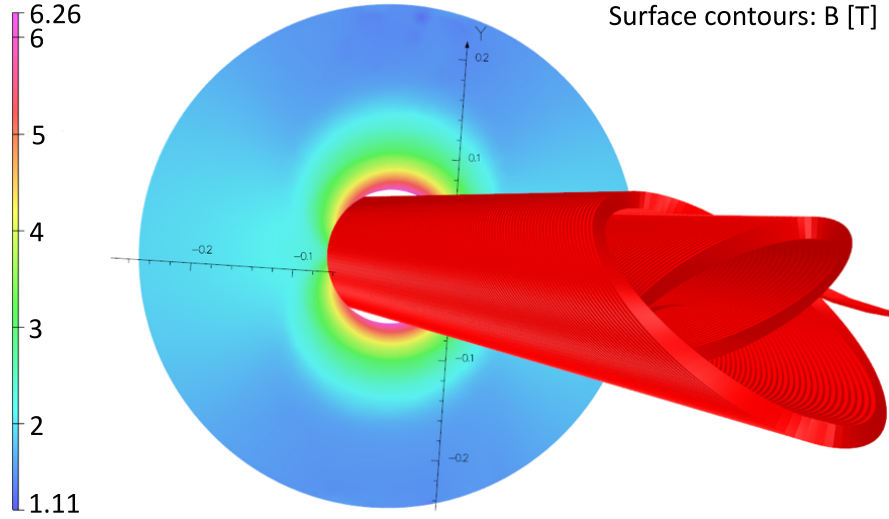


Figure 2.6 – CD1 magnetic field distribution in Opera with a centre  $B$  field of 10 T. Note that the yoke in this simulation is round, whereas the yoke aperture in the final CD1 magnet is square-shaped.

### 2.5 Electrothermal and magnetoquasistatic finite-element model

In a time-varying magnetic field, the efficiency of the protection methods and the current decay are studied, when the magnet is protected by only CLIQ, or only EE, or both of them initiated at the same time or with a delay time between them. The goal of this study is to simulate the electromagnetic and electrothermal behavior of a 2D cross-section model with the quench protection system connected in the electrical circuit. The model helps us study the protection and discharge phases introduced in Section 1.5.

In this approach, the coupled model includes, on the electromagnetic side, inter-filament coupling currents in the bare cable, quench-state check algorithm, eddy currents in the spar domains, Al protective shell and outer shell, and a non-linear  $B$ - $H$  curve in the iron yoke; on the thermal side, losses in the bare cable, and temperature- and field-dependent material properties in the bare cable, insulation, spars, ribs and Al protective shell. As mentioned in Section 2.4, the obtained voltage-based detection time can be added at the beginning of simulation in order to calculate the peak temperature in the conductor after a quench. The results and discussions are presented in Section 3.3, for the CD1 model magnet.

### 2.5.1 Basic formulations

On the thermal side, the heat-balance equation is given by:

$$dc \frac{\partial T}{\partial t} - \nabla \cdot (k \nabla T) = q_v \quad (2.33)$$

where  $d$  is the mass density,  $c$  the specific heat,  $T$  the temperature,  $t$  the time,  $k$  the thermal conductivity and  $q_v$  the volumetric heating power.

On the electromagnetic side, the Ampere's law is written as

$$\vec{\nabla} \times \vec{H} = \vec{J} \quad (2.34)$$

where  $H$  is the magnetic-field strength and  $J$  the current density.

The relationship between  $B$  and  $H$  is  $\vec{B} = \mu_0(\vec{H} + \vec{M})$ , where  $\mu_0$  is the permeability and  $M$  the magnetization. If we inject this formula into Eq. (2.34), we obtain

$$\vec{\nabla} \times \left( \frac{\vec{B}}{\mu_0} - \vec{M} \right) = \vec{J} \quad (2.35)$$

In the magnetic vector potential formulation  $\vec{B} = \vec{\nabla} \times \vec{A}$ , thus Eq. (2.35) becomes

$$\vec{\nabla} \times \left( \frac{1}{\mu_0} \vec{\nabla} \times \vec{A} \right) - \vec{\nabla} \times \vec{M} = \vec{J} \quad (2.36)$$

The current density  $J$  can be expanded as  $\vec{J} = \sigma \vec{E} + \vec{J}_s$ , where  $\sigma$  is the electrical conductivity,  $E$  the electric field and  $J_s$  the source current density. Eq. (2.36) is thus further developed:

$$\vec{\nabla} \times \left( \frac{1}{\mu_0} \vec{\nabla} \times \vec{A} \right) - \vec{\nabla} \times \vec{M} - \sigma \vec{E} = \vec{J}_s \quad (2.37)$$

If we put the relationship between the electric field  $E$  and the vector potential  $A$ , which is defined by  $\vec{E} = -\frac{\partial \vec{A}}{\partial t}$ , into Eq. (2.37), the final magnetoquasistatic equation is:

$$\vec{\nabla} \times \left( \frac{1}{\mu_0} \vec{\nabla} \times \vec{A} \right) - \vec{\nabla} \times \vec{M} + \sigma \frac{\partial \vec{A}}{\partial t} = \vec{J}_s \quad (2.38)$$

where  $\sigma \frac{\partial \vec{A}}{\partial t}$  is the eddy-current term.

In the bare cable region, an equivalent magnetization term  $\vec{M}_e$  is formed to include the inter-filament coupling currents [82, 83].

$$\vec{\nabla} \times \left( \frac{1}{\mu_0} \vec{\nabla} \times \vec{A} \right) - \vec{\nabla} \times \vec{M}_e = \vec{J}_s \quad (2.39)$$

## Chapter 2. Simulation Methods

---

The equivalent magnetization term has been used in different models with the following definition [57, 84, 85]:

$$\vec{M}_e = -\frac{2\tau}{\mu_0} \frac{\partial \vec{B}}{\partial t} \quad (2.40)$$

with a time constant  $\tau$  for inter-filament coupling losses:

$$\tau = \frac{\mu_0}{2\rho_{et}} \left( \frac{L}{2\pi} \right)^2 \quad (2.41)$$

where  $\rho_{et}$  is the effective resistivity of the strand copper matrix and  $L$  the filament twist pitch length.

Considering the form of  $\vec{M}_e$ , the differential equation to be solved in the bare cable is

$$\vec{\nabla} \times \left( \frac{1}{\mu_0} \vec{\nabla} \times \vec{A} \right) + \vec{\nabla} \times \left( \frac{2\tau}{\mu_0} \vec{\nabla} \times \frac{\partial \vec{A}}{\partial t} \right) = \vec{J}_s \quad (2.42)$$

The equivalent magnetization approach, which includes the effects of eddy currents, is beneficial in the simulation since the finite-element formulation is derived from the vector potential only, without the need for an additional degree of freedom.

When the model is coupled to an electrical circuit, a stranded formulation is used which adds a current  $I$  and an electromotive force  $V$  degree of freedom to the vector potential  $A$ , where  $I$  is the current per stranded coil turn, and  $V$  the voltage drop across the coil. The total voltage drop across the coil  $V$  is a combination of a resistive part  $V_r$  and an inductive part  $V_l$ , given by  $V = V_r + V_l$ .

The resistive voltage drop is  $V_r = IR$ . The current flowing in the copper part is defined as  $I_{cu} = If_{cs}$ , with  $f_{cs}$  the fraction of current flowing in the copper compared with the superconductor. The copper resistance is computed as follows

$$R = \rho_{cu} \frac{l}{A} \quad (2.43)$$

with  $\rho_{cu}$  the copper resistivity,  $l$  the total cable length and  $A$  the copper area in one stranded coil turn.

The cable length per stranded coil area is the multiplication of the number of turns per stranded coil area  $n_t$  and the effective length chosen to match the resistance of the 3D coil  $L_c$  (physical length). The cable length is thus given by  $l = n_t L_c$ . Note that in a CCT-type magnet,  $n_t$  is always 1. This parameter is useful for multi-turn areas in other types of magnet.

The copper area in one stranded coil turn is written as  $A = A_{cu}/n_t$ , with  $A_{cu}$  the total copper area in the stranded coil area, which can be expressed by  $A_{cu} = S_c f_{cond}(1 - f_{sc})$ , where  $S_c$  is the



stranded coil area,  $f_{\text{cond}}$  the conductor fraction in the stranded coil area and  $f_{\text{sc}}$  the fraction of superconductor within the conductor area.

By injecting the expressions of  $l$  and  $A$  into Eq. (2.43), we obtain

$$R = L_c \frac{n_t^2}{S_c} \frac{1}{f_{\text{cond}}(1 - f_{\text{sc}})} \rho_{\text{cu}} \quad (2.44)$$

Since the FEA is done on the cable elements, the above equation is developed as

$$R = L_c \left( \frac{n_t}{S_c} \right)^2 \frac{1}{f_{\text{cond}}(1 - f_{\text{sc}})} \int \rho_{\text{cu}} dS \quad (2.45)$$

The final expression of the resistive voltage is given by

$$V_r = IL_c \left( \frac{n_t}{S_c} \right)^2 \frac{f_{\text{cs}}}{f_{\text{cond}}(1 - f_{\text{sc}})} \int \rho_{\text{cu}} dS \quad (2.46)$$

The inductive voltage is given by the time derivative of the linked flux:

$$V_l = \frac{\partial \Phi}{\partial t} = n_t \frac{\partial}{\partial t} \int (\vec{u} \cdot \vec{A}) dS \quad (2.47)$$

where  $\vec{p}$  is current direction vector and  $\vec{A}$  the nodal potential. For a 2D model with current restricted to flow only in the  $z$  direction, the equation becomes

$$V_l = n_t \frac{\partial}{\partial t} L_i(u A_z) \quad (2.48)$$

where  $L_i$  is the effective length scaling of the inductance chosen to match the 3D magnet (magnetic length),  $u$  the variable +1 or -1 based on the direction of the current and  $A_z$  the nodal potential in the  $z$  direction for 2D model. It is convenient to reformat this into a surface integral such that

$$V_l = L_i \frac{n_t}{S_c} u \int \frac{\partial A_z}{\partial t} dS \quad (2.49)$$

### 2.5.2 Model key features

There are three key features: the ANSYS Multi-Field Solver (MFS) between electromagnetic and electrothermal domain, the electrical circuit coupling to the electromagnetic domain for the quench protection system modeling, and the usage of ANSYS thermal and electromagnetic UDEs for the bare superconducting cable areas.

### ANSYS Multi-Field Solver

The ANSYS Multi-Field Solver (MFS) is available for a variety of coupled problems. The MFS solves sequentially the coupled physics problems. The working principle is described as follows. Each type of model is created with an independent set of equations and mesh, the ensemble of which is called a field. Each field has a group of defined element types. The surfaces or volumes, where the loads need to be transferred, are identified. By using a set of MFS commands, one can configure the problem and define the solution sequencing. The MFS iterates between each physics field until the loads across physics interfaces converge. In our case, the heat generation and temperature are defined as loads. At the end of the simulation, independent results files are created for each field.

### Circuit coupling

In addition, electrical circuits are connected to the magnetoquasistatic FEM domain in order to evaluate the response of the protection components, e.g., an energy-extraction (EE) system or a coupling-loss induced quench (CLIQ) system. Every cable area in a 2D cross section is defined as a stranded coil element and connected in the electrical circuit. By coupling or uncoupling the voltage degrees of freedom between nodes, we are able to control the function of the circuit, e.g., to charge the CLIQ capacitor. Moreover, by coupling the finite element regions to an electrical circuit defined within ANSYS using the CIRCU124 element, the effect of eddy currents in the magnet structure can be coupled to the behavior of the magnet in the circuit.

### ANSYS 2D User-Defined Elements

In the coupled simulations, the 2D UDEs of ANSYS are used for a better prediction of the superconducting magnet quench behavior. The basis of UDE creation is the modification of the individual stiffness, mass and damping matrix in the FEM equations. The integration of the modified codes is done by compilation of the code fragments and linking them to the ANSYS libraries. A full description of these UDEs and the benchmark study can be found in [55]. There are two new types of UDEs.

The thermal UDE supports the multi-dependence material properties, which are not only temperature dependent but also magnetic-field dependent, while the ANSYS standard elements only support temperature-dependent material properties. If  $B$ -field dependent material properties are needed, one has to update them through APDL code in each element and at each time substep, the execution of which is computationally inefficient. The thermal UDE solves this problem and the necessary material properties are generated internally in the code, which is convenient and efficient for numerical computation.

The electromagnetic UDE includes the Inter-Filament Coupling Currents (IFCCs) within the conductor. The generated losses of IFCCs are critical in CLIQ modeling. For the CCT-type

## 2.5. Electrothermal and magnetoquasistatic finite-element model

magnet quench protection, the study of CLIQ performance during a quench is an essential task since CLIQ is the baseline protection method in the FCC conceptual design study. The generated losses of IFCCs within the cables are for the first time included in the CCT-type magnet quench simulations, by using the electromagnetic UDE in ANSYS. Furthermore, the quench status check process is incorporated inside these two elements.

Note that only the bare cable areas use the new UDEs. The remaining areas (iron, insulation, structure, air) use the standard elements. The 2D UDEs are initially created for a magnet cross section that can be longitudinally extruded to a 3D one. Some modifications, which are described in the following paragraphs, are made within these UDE FORTRAN files to accommodate the special locally 3D features of CCT-type magnets. An overview of the coupled electromagnetic, circuit, and thermal simulation in ANSYS with user-defined elements is shown in Figure 2.7 at the example of CD1.

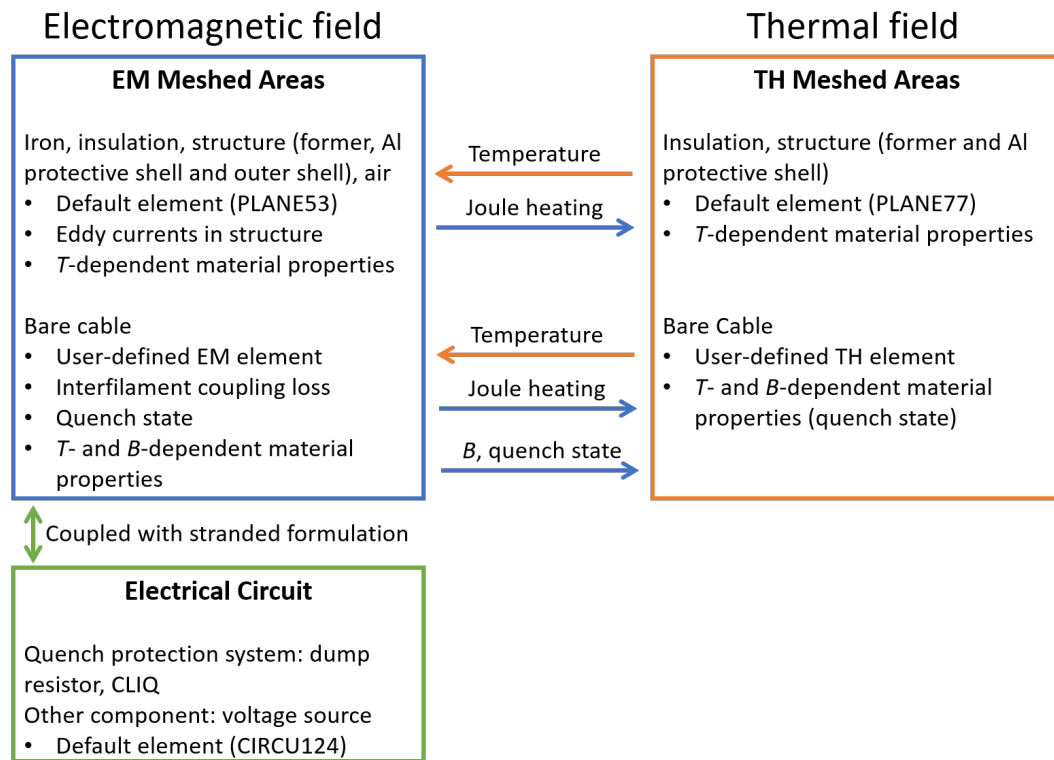


Figure 2.7 – Overview of coupled electromagnetic, circuit, and thermal simulation in ANSYS with user-defined elements at the example of CD1 (following [55]).

### Addition of critical current fit functions

The critical current fit functions in Eq. (2.25), (2.26) and Eq. (2.30), (2.31), (2.32) are implemented in the UDE code.

### Adjustment of current density

In a 2D cross-section model of a CCT-type coil, none of the cables is cut orthogonally. Thus, depending on the cutting angle, the cable cross section appears always larger than the real section. The cross-section through the CCT magnets yields wide cable areas in the pole regions, which can be observed in Figure 2.8a. Figure 2.8b shows a comparison of the FEM turn area and real cable area.

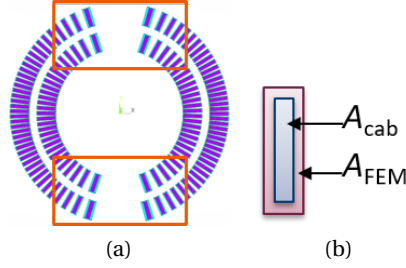


Figure 2.8 – The apparent cable cross-section in the cross-section of a CCT magnet, as compared to the actual cable cross-section. (a) CD1 insulated cable cross-section. The cross-section yields wide cable areas in the pole regions, observed in the red boxes; (b) Definition of cable areas.

A tilt factor  $f_{\text{tilt}}$  is defined as the real cable cross section area  $A_{cab}$  over the FEM turn area  $A_{FEM}$ , given by  $f_{\text{tilt}} = A_{cab} / A_{FEM}$ . This factor is implemented as a new real constant in the electromagnetic UDE and can be passed via APDL code to the thermal UDE for usage. The value is calculated for each turn. In Subsection 2.4.2, different fractions of a defined cable area is distinguished. When we do the multiplication of a fraction with the tilt factor, we get simultaneously the corresponding fraction of a selected FEM area. An example is shown as below

$$f_{\text{cond}} f_{\text{tilt}} = \frac{A_{\text{cond}}}{A_{cab}} \frac{A_{cab}}{A_{FEM}} = \frac{A_{\text{cond}}}{A_{FEM}} \quad (2.50)$$

The tilt factor is used in order to adjust the current density in the superconducting fraction of the conductor region, so that the total current entering or exiting each cross section is the same. The current density is defined for calculation of quench status check and current-sharing regime. The new current density  $J_{sc}$  is thus calculated as

$$J_{sc} = \frac{J_e}{f_{\text{tilt}} f_{\text{cond}} f_{sc}} \quad (2.51)$$

for an applied current density  $J_e$  in an element. When this cable turn section is defined as a stranded coil coupled to an electrical circuit, the current density  $J_{sc}$  is written as

$$J_{sc} = \frac{In_t}{f_{\text{tilt}} S_c f_{\text{cond}} f_{sc}} \quad (2.52)$$

## 2.5. Electrothermal and magnetoquasistatic finite-element model

where  $I$  is the current per stranded coil turn,  $n_t$  the number of turns per stranded coil area, and  $S_c$  is the stranded coil area.

Moreover,  $f_{\text{tilt}}$  is used to appropriately adjust the quantity of material properties in different cable turns. The new homogenized volumetric heat capacity is calculated as

$$c_v = f_{\text{tilt}}(f_1 c_{v,\text{res}} + f_2 c_{v,\text{sc}} + f_3 c_{v,\text{cu}}) \quad (2.53)$$

To be balanced in the heat equation, the Joule heating per unit volume of modeled conductor is modified as below

$$P_{\text{res}} = \rho_{\text{cu}} f_{\text{tilt}} \frac{(f_{\text{cs}} J_e)^2}{f_{\text{cond}}(1 - f_{\text{sc}})} \quad (2.54)$$

and IFCC heat generation power per unit volume is modeled as below

$$P_{\text{tau}} = 2\tau f_{\text{tilt}} \frac{f_{\text{cond}}}{\mu_0} \left| \frac{\partial B}{\partial t} \right|^2 \quad (2.55)$$

In addition, the resistive voltage drop across the coil is also modified as below

$$V_r = I L_c \left( \frac{n_t}{S_c} \right)^2 \frac{f_{\text{cs}}}{f_{\text{tilt}} f_{\text{cond}}(1 - f_{\text{sc}})} \int \rho_{\text{cu}} dS \quad (2.56)$$

### Adjustment of conductor length

The 2D UDEs are independent of length. However, in a 3D coil, the turn length of each turn is different for a chosen cut, shown in Figure 2.9. The physical length  $L_c$  and magnetic length  $L_i$  are used for coupling resistive and inductive effects to the circuit, so the lengths impact the current and voltage in the electromagnetic model. Since each FEM area represents a different length of cable, the conductor physical length is adjusted in the real constants of each conductor piece for the calculation of resistance, voltage and current.

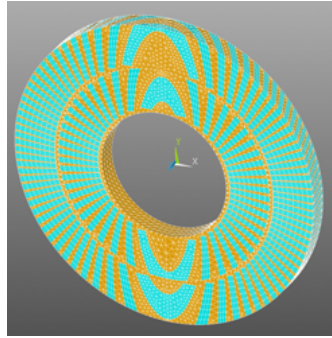


Figure 2.9 – Periodic slice model of a two-layer CCT-type coil.

A length factor  $f_l$  is defined as the real longitudinal cable length in a pitch distance  $l$  over the pitch distance  $p$ , given by  $f_l = l/p$ . Figure 2.10 illustrates the lengths used in the definition of the length factor.

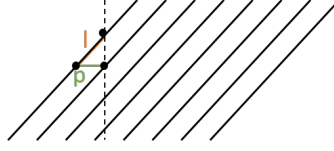


Figure 2.10 – Lengths used in the definition of the length factor.

In a CCT-type magnet, the magnetic length  $L_i$  is simply expressed as  $L_i = pn_p$ , where  $p$  is the pitch length and  $n_p$  the number of pitches. The pitch length is defined as the moving distance of a cable after one turn.

One turn length can be written as the sum of all the real longitudinal cable lengths in a pitch distance on a chosen 2D cut:  $\sum_s^{n_{sec}} l_s = \text{Turn length}$ . where  $n_{sec}$  is the number of cross-section slots on one cut area. Therefore each cable cross section  $s$  represents a physical conductor length of

$$L_{c,s} = f_{l,s} L_i \quad (2.57)$$

This length is calculated for each cross-section slot and involved in the voltage drop across the coil. In Eq. (2.46) and (2.49), we observe the importance of using right lengths, i.e.,  $L_c$  and  $L_i$ , to compute the voltage drop in a circuit-coupled model. Eq. (2.57) is then injected into Eq. (2.56) for the conductor length adjustment.

### 2.5.3 Validation of automated model generator

The automated 2D model generator is created for the CCT-type magnets. In this generator, the different protection cases can be pre-selected for the corresponding study, e.g., only energy extraction, or only CLIQ, or both of energy extraction and CLIQ, or natural decay without any protection system, with a cross-section turn already quenched at the beginning of the simulation. The delay time between the initiation of energy extraction and CLIQ can also be adjusted in the case when both are involved in the coupled simulation. Furthermore, an additional detection time can be introduced before turning on the protection methods to estimate the hot-spot temperature in the magnet after a quench.

As the test results of CD1 is not available within the period of my thesis, the existing test results of CCT4, a model magnet built at LBNL [86, 87, 88], are therefore used to compare with the simulation and to validate the model and the model generator, since this magnet is one of the closest magnets to CD1. Figure 2.11 shows the CCT4 coil assembly. The main parameters, as well as the magnet component materials are listed in Table 2.3. The dimensions of different layers are listed in Table 2.4. There are several differences between CD1 and CCT4, such as the

## 2.5. Electrothermal and magnetoquasistatic finite-element model

conductor and the mechanical structure. The CCT4 coil is surrounded by a large aluminum shell of a thickness of 55.2 mm and then an iron yoke of a thickness of 197.5 mm. Note that the yoke was clamped around the shell, thus the gap between the shell and yoke was eliminated.

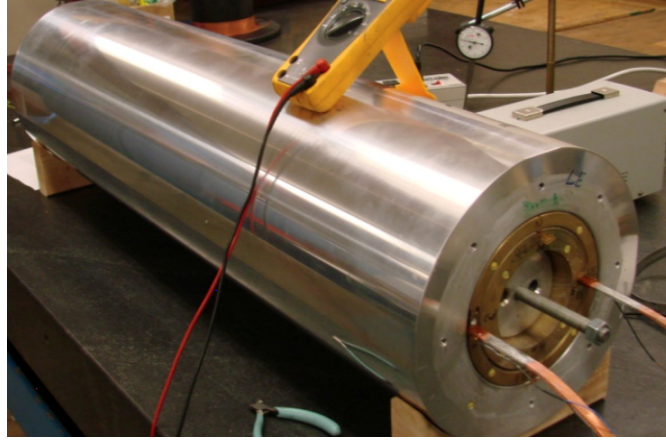


Figure 2.11 – CCT4 coil assembly at LBNL. The most-outer silver cylinder is the thick aluminum shell.

Table 2.3 – Main parameters of the CCT4 Nb<sub>3</sub>Sn dipole magnet of LBNL.

| Magnet parameter                | Value              |
|---------------------------------|--------------------|
| Nb turns                        | 64                 |
| Cable thickness                 | 1.4 mm             |
| Cable width                     | 10.1 mm            |
| Number of strands               | 23                 |
| Strand diameter                 | 0.8 mm             |
| Filament twist pitch            | 14 mm              |
| Insulation thickness            | 0.2 mm             |
| Measured Cu RRR                 | 300                |
| Non-Cu fraction                 | 0.54               |
| Short-sample current (4.2 K)    | 19.3 kA            |
| Short-sample bore field (4.2 K) | 10.4 T             |
| Coil physical length            | 1 m                |
| Coil magnetic length            | 0.5 m              |
| Magnet component                | Material           |
| Strand type                     | Nb <sub>3</sub> Sn |
| Former (spar, rib)              | Aluminum bronze    |
| Shell                           | Aluminum           |

The critical current fit functions in Eq. (2.25) and (2.26) are used in the case of the CCT4 with the following coefficients to match the short sample measurement:  $T_{c0} = 18$  K,  $B_{c20} = 28$  T and  $C = 4.5 \cdot 10^{10} \text{ A} \cdot \text{T}^{\frac{1}{2}} / \text{m}^2$ .

Table 2.4 – Dimensions of different layers of the CCT4 Nb<sub>3</sub>Sn dipole magnet of LBNL.

| Unit [mm]   | Inner diameter | Outer diameter | Thickness |
|-------------|----------------|----------------|-----------|
| Inner layer | 45             | 64.4           | 19.4      |
| Outer layer | 64.9           | 78.8           | 13.9      |
| Shell       | 79.8           | 135            | 55.2      |
| Yoke        | 137.5          | 335            | 197.5     |

When we compare the data, it is also important to match the 2D to 3D no-loss inductance as best as possible, with a single scaling parameter which in this case is the magnetic length. Since the iron saturates at fairly low current in the case of CCT4, the scaling factor is expected to be mostly constant with current. Therefore a constant length is used to match with the extraction current.

CCT4 has 64 turns with a pitch length of 7.93 mm, which in turn gives a magnetic length of 507.8 mm. As a start, this value is used in the simulation model without any loss. The no-loss inductance at the beginning of the decay is calculated and the value matches the one from the 3D model, which is 1.8 mH [54].

The CCT4 model magnet was protected only by an energy-extraction system. Simulations are run with  $R_{EE} = 30 \text{ m}\Omega$ . We proceed step by step, starting with a no-loss model, adding successively eddy currents in the aluminum shell, eddy currents in the spars, and inter-filament coupling currents, to obtain the results of a complete model. The simulation is started with the peak current. Figure 2.12 presents the contribution of different losses to the current decay behavior. We confirm that the eddy currents in the aluminum shell dominate the behavior by increasing the decay speed, leading to a deviation from the no-loss case [54]. The effect of the addition of eddy currents in the spars is negligible compared to the one of the shell. The contribution of IFCL only accelerates the current decay by a small amount.

The comparisons of current decay curves between simulation and test data at different excitation levels are presented in Figure 2.13. For these three current levels, a very good agreement is observed between the computed decay curves and the measurement. It is worth noting that for the excitation current of 13.6 kA, the current measurement saturates at 10 kA. Thus the comparison starts when the saturation ends by overlapping the timing for benchmarking at high currents. Besides, the large spike on the graph at extraction is due to noise from the switch opening.

To summarize, the 2D coupled model is capable to accurately predict the current decay behavior when the magnet is protected by an energy-extraction system. This can only be previously achieved by a full 3D model including the end effects, according to [54]. The fact that IFCL contributes relatively little to the overall shape of the current decay implies that the model validation is not complete. For completing validation, we need data from a CLIQ discharge, in which case IFCCs are the dominant effect in the first milliseconds.



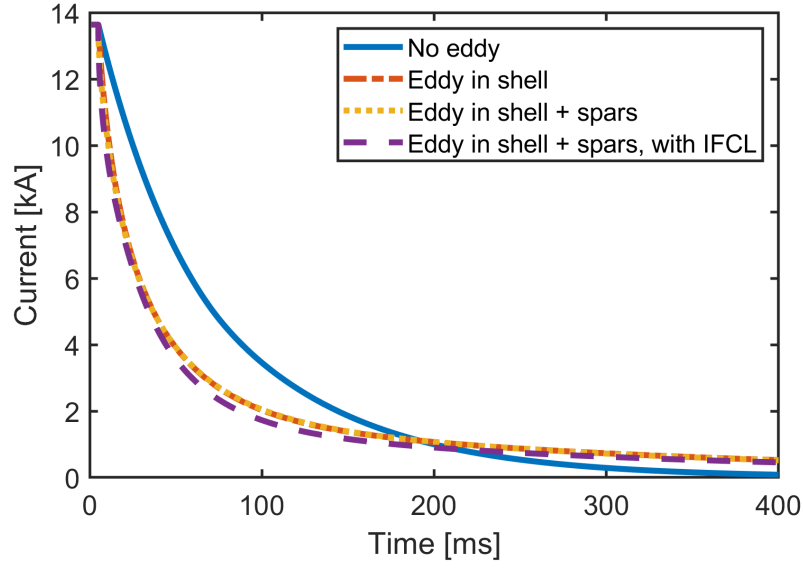


Figure 2.12 – Comparison of current decay curves from ANSYS with contributions of different losses in the CCT4 model magnet.

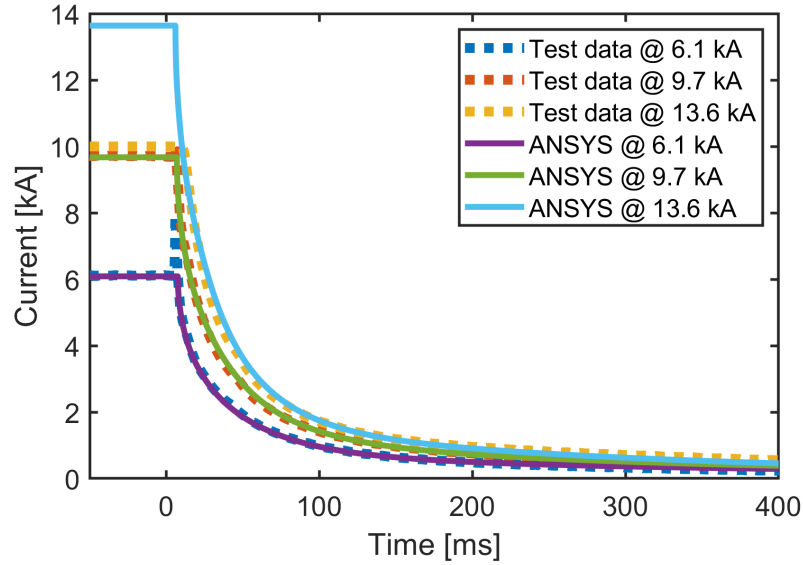


Figure 2.13 – Comparison of current decay curves between ANSYS simulation and test data at different current levels of the CCT4 model magnet, when the magnet is protected by a dump resistor of 30 mΩ.

However, the adopted equivalent magnetization formulation for homogenized cables, mentioned in Eq. (2.40) and (2.41), might not be appropriate for simulating fast transients, such as a CLIQ discharge. According to [29], a shorter time constant of  $\Delta B$  was obtained when the effect of IFCC was implemented using the homogenized formulation, with respect to a

multi-strand model. As a consequence, IFCLs are quantitatively different, leading to a different current decay curve.

The 2D model is therefore not fully conservative as the fast response from IFCLs may lead to a slight anticipation of the moment of quench. Nevertheless, it is still a good tool to predict the whole current decay profile in the coil. Since the used modeling technique has never been validated against experimental results for CLIQ-discharge transients, how big the impact is will be evaluated when the measurement results are available.

As CCT5 was also protected by the energy-extraction system, the CLIQ behavior needs to be verified after the test of the CD1 model magnet<sup>2</sup>. To conclude, the model and automated model generator could be partially validated based on the test results of CCT4, protected only by an energy-extraction system.

---

<sup>2</sup>Due to the outbreak of Coronavirus disease (COVID-19), CD1 could not be tested within the time frame of this thesis.

## 3 Quench Protection

### 3.1 Goals and overview

The final goal of my thesis is to develop an efficient quench detection and protection system of a two-layer CCT magnet. To achieve this, the development, construction, and test of a detection and protection system for PSI's two-layer model magnet CD1 is necessary. In this chapter, we aim to investigate the possibility via simulations to apply different protection methods, energy extraction, CLIQ, and co-wound copper tape, described in Chapter 1, to the CD1 short model. The protectability study with a dump resistor is first discussed in a 3D magnetostatic and electrothermal model, in Section 3.2. Then the CLIQ protection study is described in a 2D electrothermal and electrodynamic model using UDEs, in Section 3.3. The co-wound copper tape protection study is then explained in Section 3.4.

### 3.2 Energy extraction

In order to study the energy-extraction system with a value of  $R_{EE} = 40 \text{ m}\Omega$ , several steps are needed. A MIITs calculation is first computed for the CD1 cable to have an estimation of the time budget without exceeding a maximum temperature of 350 K. A magnetostatic/thermal model described in Section 2.4 is used to simulate the quench propagation scenario. With the temperature profiles obtained from the simulation, one can calculate the rising quench resistance in the coil using the adiabatic integrator, allowing the computation of a voltage detection time. Once the time is known, the total MIITs from the quench initiation to the end of the current decay can be calculated when the magnet is protected with a dump resistor.

For the study of CD1, the Summers critical current fit functions in Eq. (2.25) and (2.26) are used. The time budget for the detection phase is studied via MIITs calculation, which is explained in Subsection 2.2.2. The adiabatic integrator explained in Section 2.3 is involved to determine the detection time needed and the current decay for a selected dump resistor value. With the MIITs calculation introduced in Section 2.2, a worst-case estimate of the hot-spot temperature in the coil after a quench using the energy-extraction method is performed [89].

### 3.2.1 Time budget estimation

For quench detection, a voltage threshold and a validation time, explained in Section 1.5, need to be selected. A lower voltage threshold ( $\sim 100$  mV) implies a shorter  $\Delta t_{\text{thres}}$  but a longer  $\Delta t_{\text{val}}$ , since a voltage rise of a short duration caused by a flux jump is not considered as a quench. Only a continuous voltage rise can be confirmed as a quench in the magnet. On the contrary, a higher voltage threshold implies a longer  $\Delta t_{\text{thres}}$  but a shorter  $\Delta t_{\text{val}}$ .

When a high current flows in the superconductor, the fluxoids within the superconductor are subjected to forces that could lead to a flux flow causing a local heat deposition. This is called a flux jump. A flux jump can lead to eventually a local normal zone. If the induced heat amount is dissipated throughout the conductor, then the normal zone returns to the superconducting state. When there is a huge amount of heat generated by the flux jumps, it results in a magnet quench. All flux jumps induce voltage spikes, that are picked up by the detection electronics [90, 91].

In our study, a threshold of 500 mV is used, which means we can nearly suppress the validation time at high currents, where flux jumps do not cause detection problems any more [92]. This choice is made because of two reasons: 1) to avoid a false trigger due to flux jumps and noise; 2) higher thresholds are reached in a quick way at high operation currents due to the fast longitudinal quench propagation.

Therefore, assuming a threshold of 500 mV and a switch time  $\Delta t_{\text{switch}} \sim 5$  ms to turn on the quench protection system, the total detection time is defined as  $t_d = \Delta t_{\text{thres}} + \Delta t_{\text{switch}}$ . The time budget to reach the threshold  $\Delta t_{\text{thres,ref}}$  for different excitation levels is listed in Table 3.1, where  $\text{MIITs}_{\text{ref}}$  is the MIITs value for 350 K and  $\Delta t_{\text{thres,ref}}$  the time budget to reach a threshold of 500 mV. In addition to the nominal operation level (86%  $I_{\text{ss}} = 15545$  A), we take into account in our simulation a high operation level (90%  $I_{\text{ss}} = 16268$  A) and a low operation level (60%  $I_{\text{ss}} = 10845$  A).

Table 3.1 – Estimation of time budget by MIITs calculation for the CD1, when magnet is protected by a dump resistor of 40 m $\Omega$ .

| $I$ [A] | $B$ [T] | $\text{MIITs}_{\text{ref}}$ [MA <sup>2</sup> s] | $t_{\text{d,ref}}$ [ms] | $\Delta t_{\text{thres,ref}}$ [ms] |
|---------|---------|---|-------------------------|------------------------------------|
| 16268   | 9.4     | 10.6  | 20.2                    | 15.2                               |
| 15545   | 8.9     | 10.7  | 24.3                    | 19.3                               |
| 10845   | 6.2     | 11.4  | 75.4                    | 70.4                               |

By varying the RRR of copper in the strand, a sensitivity study on the time budget estimation by MIITs calculation for CD1 is conducted for different current levels. The results of the total time needed before the current discharge  $t_{\text{d,ref}}$  are shown in Table 3.2 to allow for a comparison. We remark that a higher RRR results in a higher total MIITs value and thus a longer detection time budget.

Table 3.2 – Sensitivity study of Cu RRR on time budget estimation by MIITs calculation for the CD1.

|  | RRR | 16268 A | 15545 A | 10845 A |
|--|-----|---------|---------|---------|
| MIITs <sub>ref</sub> [MA <sup>2</sup> s] | 100 | 10.3    | 10.4    | 11.0    |
|  | 150 | 10.6    | 10.7    | 11.4    |
|  | 250 | 10.9    | 11.0    | 11.8    |
| $t_{d,ref}$ [ms]                         | 100 | 19.1    | 23.0    | 71.8    |
|  | 150 | 20.2    | 24.3    | 75.4    |
|  | 250 | 21.3    | 25.5    | 78.8    |

### 3.2.2 Quench propagation simulation results

The longitudinal and turn-to-turn quench propagation of an inner layer of CD1 are investigated in ANSYS. The results of a simulation time of 30 ms are presented in Figure 3.1 when  $I = 15.5$  kA (86% of  $I_{ss}$ ),  $B = 8.9$  T and  $T_{cs} = 7.2$  K. The 3D coordinates of the cable centre are converted into a linear line for figure plotting purposes. The length of a turn is approximately 0.63 m.

In Figure 3.1a, the temperature profiles at different times are plotted. The quenching zone enlarges longitudinally with time. We remark that the longitudinal propagation is much faster than the turn-to-turn propagation since the heat has to go through a barrier of insulation and winding former. In Figure 3.1b, at a selected node, the temperature rises with time. As the first turn is assumed to be quenched at the beginning of the simulation, the variation of temperature in the first turn is therefore not taken into account since we are interested in the quench propagation in the longitudinal and transverse directions. The resistance in each small element in the second and third turns is calculated. The sum gives the total quench resistance. By multiplying this term by the operating current, we obtain the voltage rise in the coil. Figure 3.1c and 3.1d illustrate respectively the quench resistance and voltage rise in the coil over time.

At a current level of 1 kA, The temperature profile in the centre of the cable, along the coil at different times for a total simulation time of 8 s is presented in Figure 3.2. We remark that the onset of the turn-to-turn quench propagation is not evident compared to the longitudinal one.

### 3.2.3 Peak temperature estimation

From Figure 3.1d, the voltage-based detection time needed can be obtained for a threshold of 500 mV. The detection time  $\Delta t_{thres}$ , the total time needed before current decay  $t_d$ , the peak temperature  $T_{cable}$  predicted by MIITs, as well as the longitudinal propagation velocity  $v_p$  at different current levels are presented in Table 3.3. The layer-to-layer propagation is slow

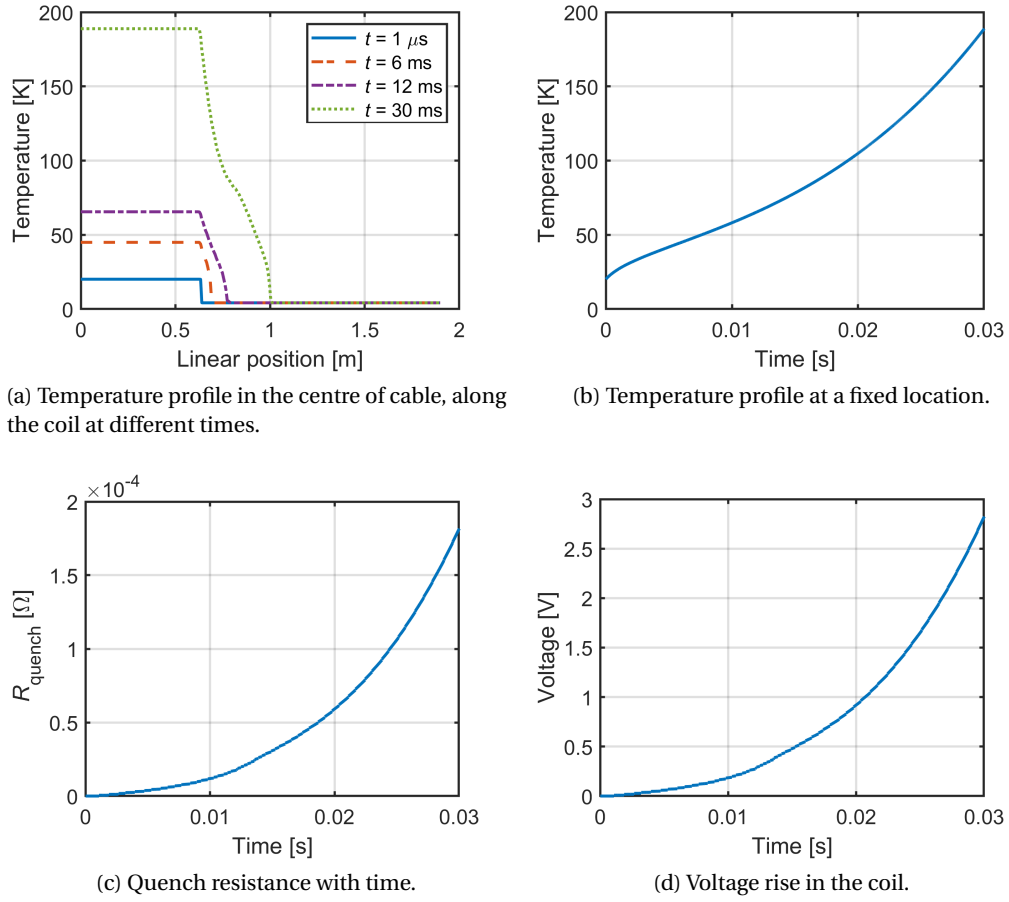


Figure 3.1 – Quench propagation simulation results of a 3-turn CD1 helical model at 15.5 kA.

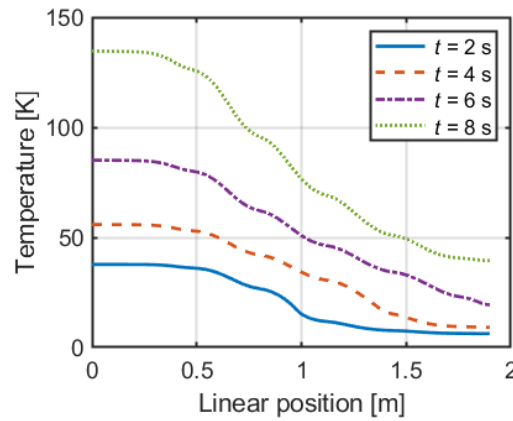


Figure 3.2 – Temperature profile in the centre of cable, of a 3-turn CD1 helical model in a quench propagation simulation at 1 kA, along the coil at different times.

and would not occur until well after detection and protection measures are active. With the energy-extraction system, the maximum temperature calculated in the coil after a quench is below 350 K, remaining on the safe side. The results obtained show that the system is capable to protect the CD1 model magnet in the case of a quench. The quantities, like  $v_p$ ,  $R_{\text{quench}}$  and voltage, are best measured when the quench goes into the third turn, as then we are independent of the initial conditions.

Table 3.3 – CD1 peak temperature estimation after a quench, when magnet is protected by a dump resistor of 40 m $\Omega$ .

| $I$ [A] | $\Delta t_{\text{thres}}$ [ms] | $t_d$ [ms] | $T_{\text{cable}}$ [K] | $v_p$ [m/s] |
|---------|--------------------------------|------------|------------------------|-------------|
| 16268   | 13.5                           | 18.5       | 316                    | 15          |
| 15545   | 15.0                           | 20.0       | 278                    | 12.7        |
| 10845   | 48.7                           | 53.7       | 197                    | 5.5         |

### 3.3 Coupling-Loss Induced Quench

In this section, the protection studies of CLIQ on the CD1 geometry at different current levels are presented, allowing us to assess its performance and to have an overview of the protectability of CLIQ on CCT magnets. A simplified schematic of the electrical circuit is first outlined in Subsection 3.3.1 to illustrate the connection between the magnet coil and different protection components.

The Subsection 3.3.2, 3.3.3 and 3.3.4 are dedicated for the protection studies using a given set of CLIQ parameters, available at LBNL, to study different cases listed in Table 3.4, e.g., when the magnet is protected by only CLIQ (Case 1), or only EE (Case 2), or by both EE and CLIQ [89]. These two protection systems can be initiated at the same time (Case 3), or with a delay time between them (Case 4). In Case 4, when the CLIQ is first fired, EE is turned on after a delay time  $t_{\text{EE}}$ . In this way, we can qualify the magnet's behavior to the CLIQ unit without damaging the magnet.

Table 3.4 – Different case studies in CLIQ quench protection simulation.

| Case | $t_d$ | CLIQ | EE | $t_{\text{EE}}$ |
|------|-------|------|----|-----------------|
| 1    |       | x    |    |                 |
| 2    |       |      | x  |                 |
| 3    |       | x    | x  | 0               |
| 4    |       | x    | x  | x               |
| 5    | x     | x    |    |                 |

The results of Case 1 at different current levels, as well as the comparison of results of Case 1, 2 and 3 at the same current level are shown in Subsection 3.3.2 and the results of Case 4 are shown in Subsection 3.3.3. By adding the necessary detection time, obtained in Subsection 3.2.3,

one can calculate the peak temperature after a quench, when the magnet is protected by only CLIQ (Case 5), explained in Subsection 3.3.4. Remind that  $t_d$  is the total time needed before current decay.

In addition to the CLIQ protection studies made for the CD1 short model magnet using the CLIQ unit with pre-defined parameters, a optimization study on the selection of CLIQ parameters is presented in Subsection 3.3.5 in the case of a short magnet and a long magnet using the CD1 geometry.

#### 3.3.1 Simplified schematic of the electrical circuit

A simplified schematic of the whole circuit with EE and CLIQ is illustrated in Figure 3.3.  $L_{1l}$  and  $L_{1r}$  respectively stand for all the stranded elements on the left and right side of the inner layer while  $L_{2l}$  and  $L_{2r}$  respectively stand for all the stranded elements on the left and right side of the outer layer. It is worth noting that in the simulation each cable cross section represents a stranded element. The main part of the energy-extraction system is a dump resistor  $R_{EE}$ , connected in series with the coil stranded elements. The components  $C_C$ ,  $R_C$  and  $V_C$  constitute the CLIQ unit. The CLIQ unit is connected to the extremities of the inner layer to introduce opposite current change in the coils that are physically adjacent for an efficient magnetic-field change. N signifies node and P signifies coupling between nodes. We control the function of the circuit by coupling or uncoupling the voltage degrees of freedom between nodes.

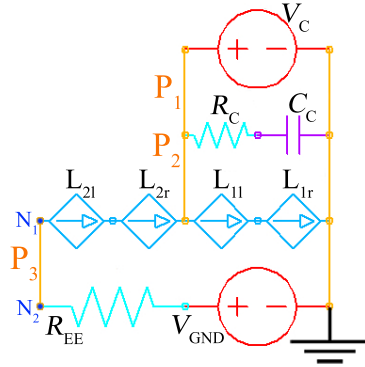


Figure 3.3 – Simplified CD1 electrical circuit with EE and CLIQ.

An example of the simulation steps is presented for Case 4. The electrical circuit in different time intervals in the simulation are illustrated in Figure 3.4. The procedure can be adapted to accommodate other cases. The start and end time of each step can be modified to adapt the modeling requirements.

Step 1 in Figure 3.4a lasts 5 ms from 0 to 5 ms. The coupling  $P_2$  is broken, while  $P_1$  and  $P_3$  exist. The first 5 ms of the simulation is dedicated to solving a static solution to charge the CLIQ capacitance and set up the current in the magnet.



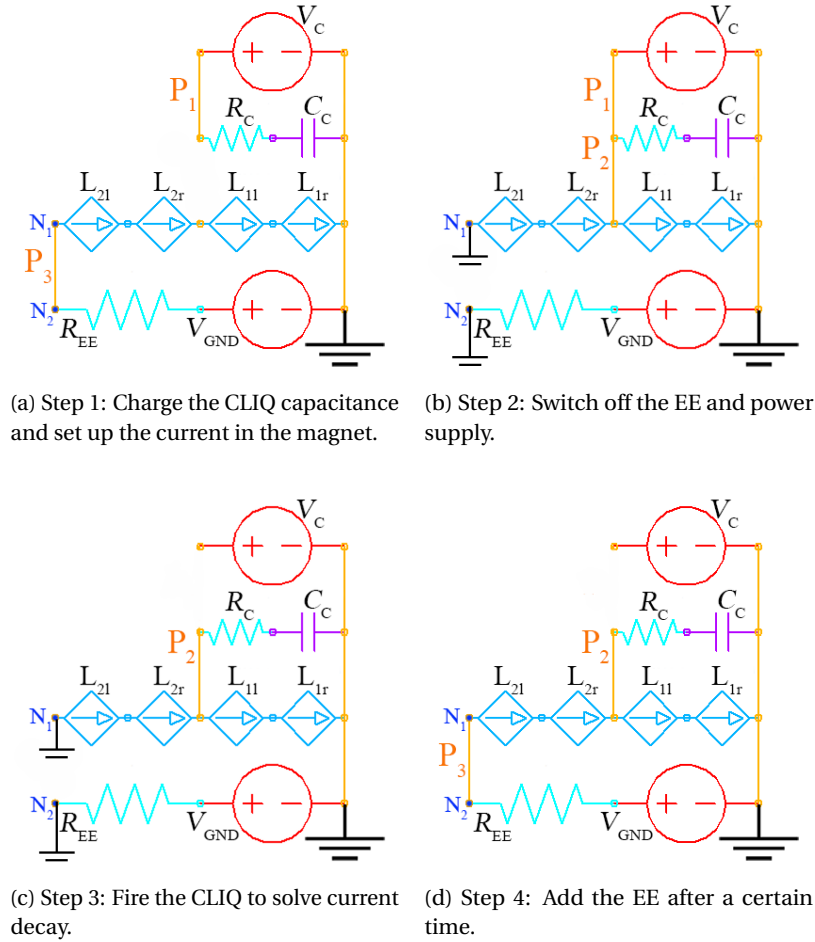


Figure 3.4 – Simplified CD1 electrical circuit with EE and CLIQ in different time intervals of a transient protection simulation.

Step 2 in Figure 3.4b lasts  $10 \mu\text{s}$  from 5.00 to 5.01 ms. The coupling  $P_3$  is broken. The voltage degree of freedom of  $N_1$  and  $N_2$  are defined as  $V = 0$ . The transient solutions algorithm is turned on. The voltage source in series with the dump resistor  $V_{\text{GND}}$  is turned off to zero in order to model the energy-extraction switch.

Step 3 in Figure 3.4c lasts  $10 \mu\text{s}$  from 5.01 to 5.02 ms. The coupling  $P_1$  is broken, while  $P_2$  is added. CLIQ is fired. The voltage across the CLIQ unit  $V_c$  is switched off to zero. The  $10 \mu\text{s}$  between 5.00 to 5.01 ms and 5.01 to 5.02 ms is used in the simulation to turn off the voltage supply and turn on the CLIQ in order to observe a smooth current transition to verify if the model is correct. The voltage switch used is a piecewise linear load. The transition has to be as small as possible. To be compatible with the model setup,  $10 \mu\text{s}$  is chosen. From 5.02 to  $(5.02 + t_{\text{EE}})$  ms, the current decay is solved.

Step 4 in Figure 3.4d starts from  $(5.02 + t_{\text{EE}})$  ms and ends at 100 ms. The voltage constraints

of  $N_1$  and  $N_2$  are deleted. The coupling  $P_3$  is added. EE is connected in the circuit again for current decay solution.

### 3.3.2 Case of CLIQ, or EE, or both initiated together

In the first set of simulations, the initial condition of temperature is  $T = 4.2$  K for all the single-turn areas. The cases with only CLIQ, or EE, or both EE and CLIQ initiated at the same time are studied. At a current level of 15.5 kA, the initial  $B$  field is presented in Figure 3.5. The peak  $B$  value on the conductor is 9.3 T while the peak  $B$  value in the bore region is 8.6 T.

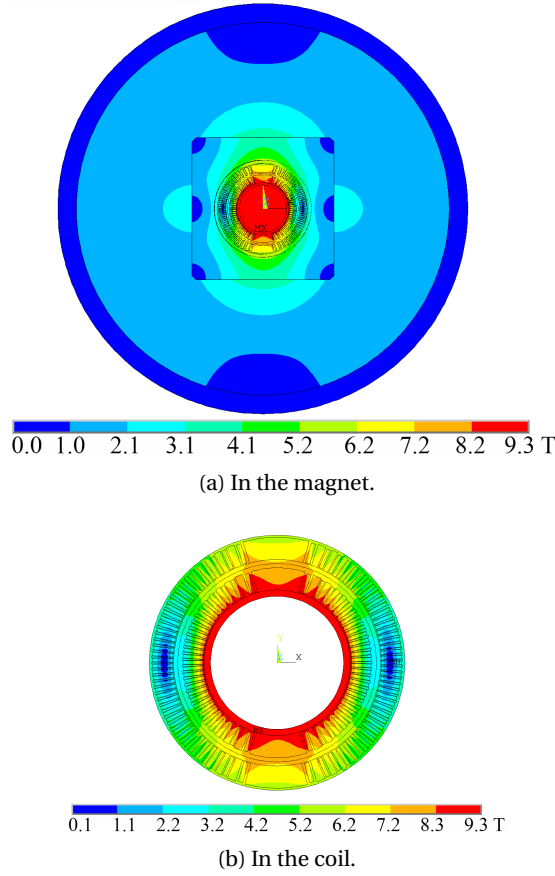


Figure 3.5 – CD1 initial electromagnetic field distribution at 15.5 kA.

Figure 3.6 shows the coupled simulation results of temperature, when the magnet is only protected by CLIQ or by both EE and CLIQ system initiated at the same time at  $I = 15.5$  kA. Recall that the dump resistor value  $R_{EE}$  is 40 m $\Omega$ . The parameters of the CLIQ unit are set as follows: the charging voltage  $V_C = 400$  V, the lead resistance  $R_C = 25$  m $\Omega$  and the internal capacitance  $C_C = 10$  mF, in agreement with LBNL's test facilities [39, 70]. After a simulation time of 100 ms, a variation in the temperature across the turns are observed because the material properties and losses vary across them, and also the cable turns in the pole regions quench earlier than others.

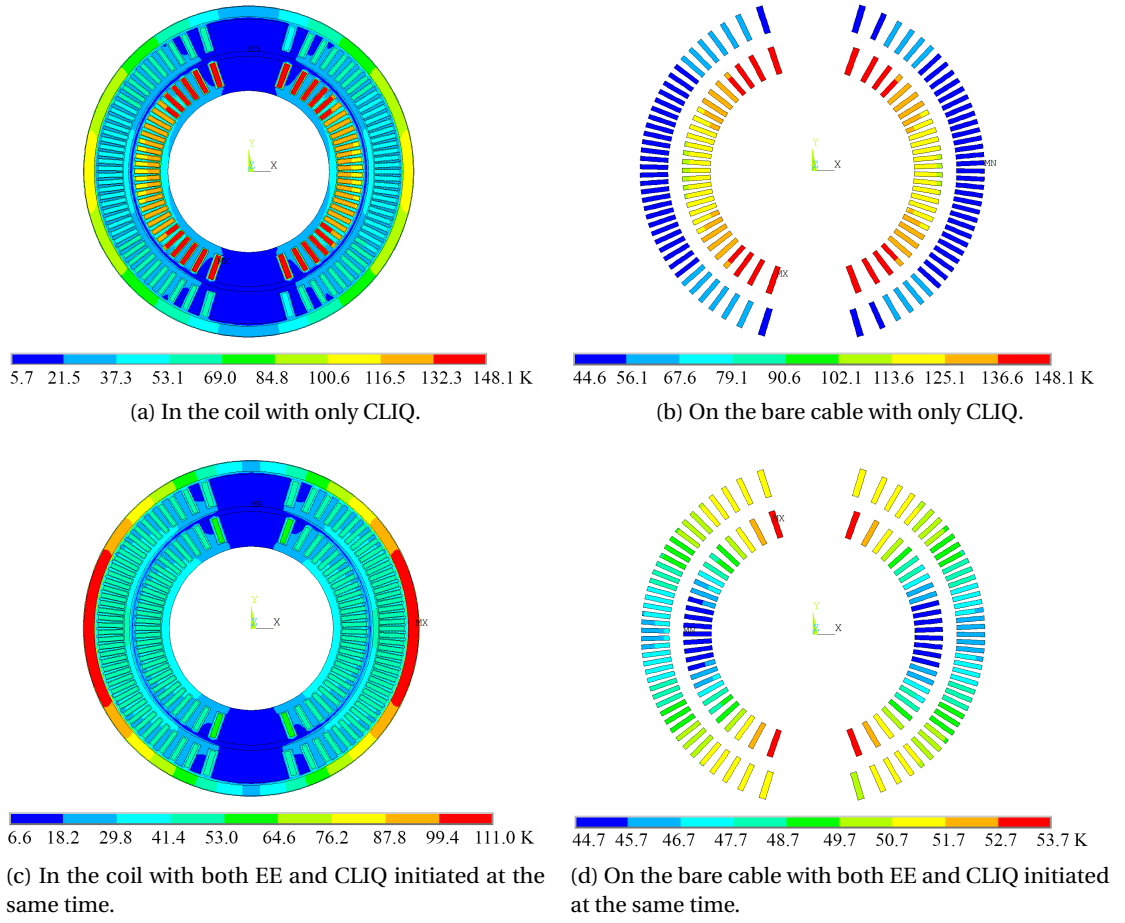
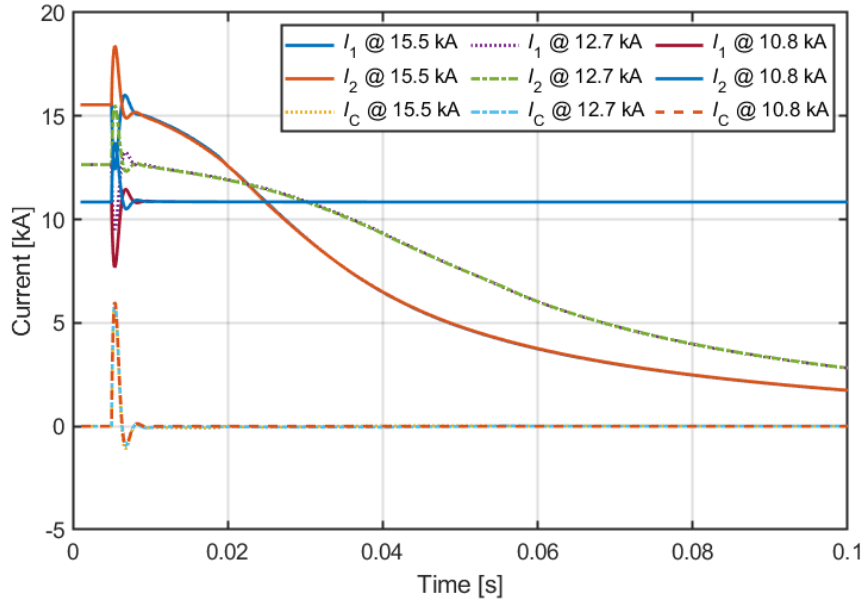


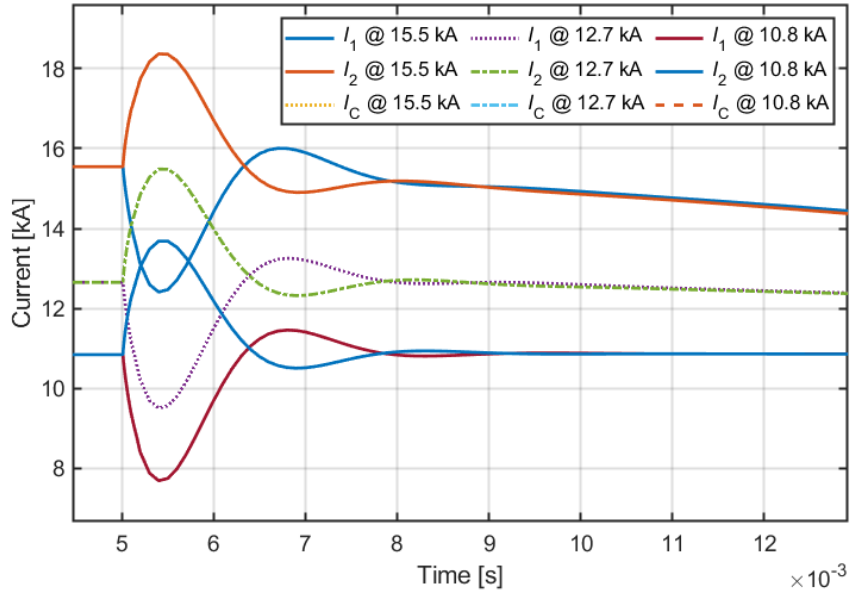
Figure 3.6 – CD1 temperature distribution at 15.5 kA after 100 ms, when magnet is protected by only CLIQ, or by both EE and CLIQ system initiated at the same time.

The current distributions at different operating currents in the cables are plotted in Figure 3.7 with only the CLIQ protection means to assess its performance. The amplitudes of the introduced oscillations are similar, whatever the current is in the magnet since  $I_C$  is nearly proportional to the capacitance value. The coupling losses induced scale with the field because this term is driven by  $\partial B / \partial t$  with a small effect of magneto-resistance. Meanwhile, the model confirmed that it is easier for the magnet to quench at high currents because the temperature margin is smaller. After a simulation time of 50 ms, 69.0% of the initial current is attenuated at  $I = 15.5$  kA. And after a simulation time of 100 ms, 88.6% of the initial current is attenuated.

As the 2D coupled model does not include the longitudinal quench propagation, one turn can quench without spreading of quenching zone along the cable. In reality, the quench will spread through the helical turn relatively quickly to quench the entire coil, even if CLIQ only quenches a tiny fraction of the cable initially. This is the case at 10.8 kA, where in the 2D simulation the fired CLIQ unit cannot bring down the current in the coil even though a few



(a) For a simulation of 100 ms.



(b) At the beginning of the simulation.

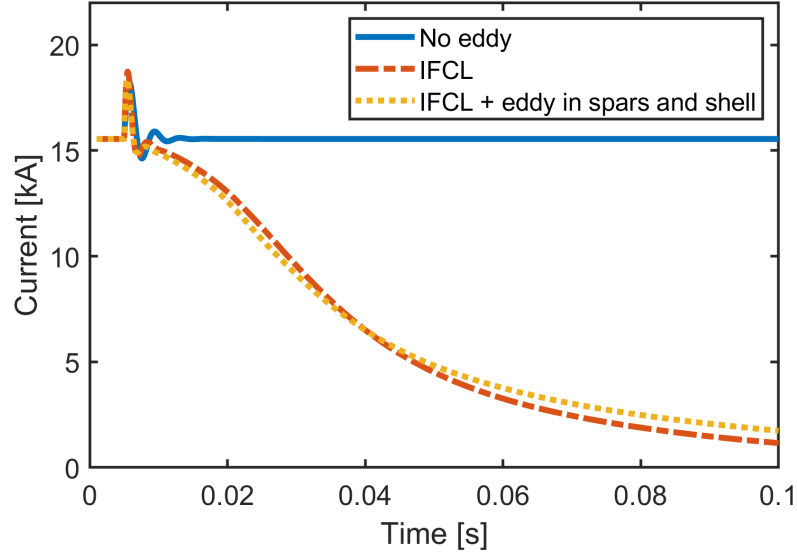
Figure 3.7 – Current profiles in the inner layer  $I_1$  and outer layer  $I_2$ , with  $I_C = I_2 - I_1$ , at different current levels, when the CD1 is protected by a CLIQ system of 400 V and 10 mF.

cable cross sections are quenched.

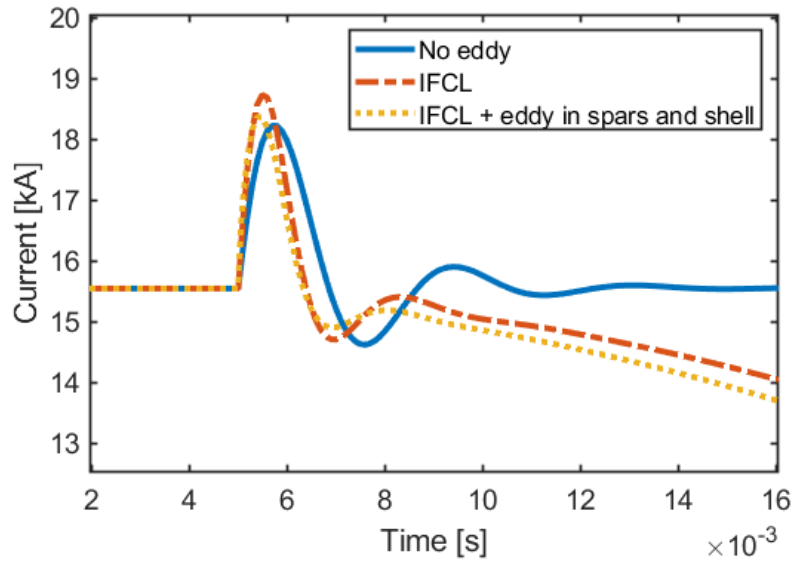
The contribution of different losses to the current decay behavior is presented in Figure 3.8. We start with a no-loss model, where the oscillation is damped only because of the lead resistance.

### 3.3. Coupling-Loss Induced Quench

Then we add successively inter-filament coupling currents and eddy currents in the spars and protective shell, to obtain the results of a complete model. The simulation is started with the nominal current. In this figure, we observe that the quench is initiated due to IFCLs when using CLIQ for the magnet protection.



(a) For a simulation of 100 ms.



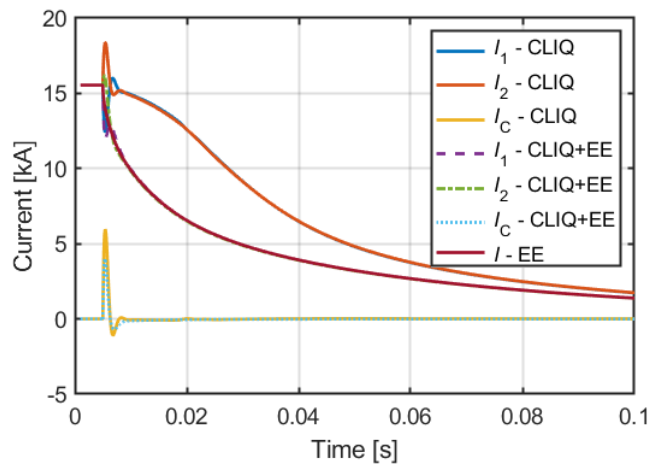
(b) At the beginning of the simulation.

Figure 3.8 – Comparison of current decay curves from ANSYS with contributions of different losses in the CD1 model magnet.

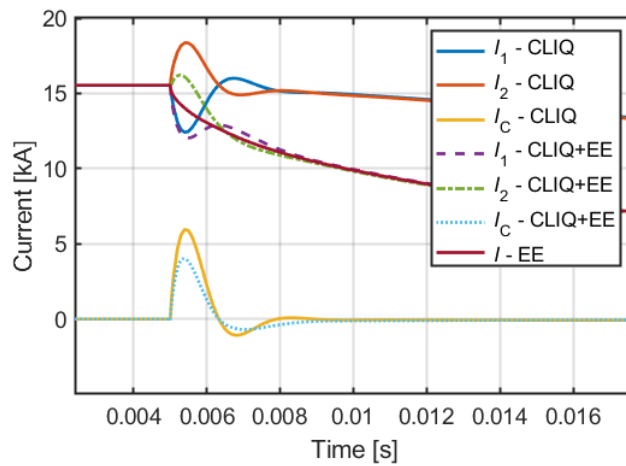
If we have a close look at the beginning of the simulation, displayed in Figure 3.8b, the initial current change rate of the induced oscillation, when we add the inter-filament coupling losses

in the model, is slightly higher than the no-loss case. This can be partially explained by the inappropriate adopted equivalent magnetization formulation for homogenized cables in the model for simulating fast transients, as mentioned in Subsection 2.5.3.

Besides, a comparison of the current profiles in the different protection configurations is illustrated in Figure 3.9 at  $I = 15.5$  kA. When the dump resistor and CLIQ are both fired at the same time, a faster current decay is observed compared to the case with only CLIQ. The amplitude of the alternating component of the current is reduced due to the energy dissipated in the energy-extraction resistor.



(a) For a simulation of 100 ms.



(b) At the beginning of the simulation.

Figure 3.9 – Current profile comparisons at 15.5 kA, when the CD1 is protected by only EE, or only CLIQ, or both EE and CLIQ initiated at the same time.

#### 3.3.3 Case of CLIQ and EE with an in-between initiation delay time

In the second set of simulations, the initial condition of temperature is still  $T = 4.2$  K for all the single-turn areas. The case with both EE and CLIQ, but initiated with a delay time between them, is studied.

When CLIQ is first triggered during a magnet test, the energy-extraction system should be included in the circuit for CD1 safety reasons. By delaying the triggering of the EE system, we can qualify the magnet's response to CLIQ without risking the magnet. The delay time between the CLIQ trigger and initial CLIQ-induced quench is 0.5 ms and 24 ms respectively when the operating current is 15.5 kA and 12.7 kA. In order to validate the UDE-based model, different delay times between the initiation of CLIQ and EE need to be selected for different current levels. For a nominal current (high current), we wait for the end of the damping of the CLIQ oscillations to avoid a too high voltage to ground due to voltage superposition. For a low current level, we may need a longer delay time to validate the behavior of CLIQ, e.g., 30 ms for a current level of 12.7 kA.

Three EE delay times are used in the study: 10, 20 and 30 ms when the magnet is powered at 15.5 kA. Figure 3.10 illustrates the temperature distribution in the coil and cable. A lower maximum temperature is observed after a simulation of 100 ms when the energy-extraction system is initiated at an earlier time, as expected. Furthermore, the position of the peak temperature is changed from the Al protective shell to the cable when the delay time of initiating the energy-extraction system increases.

Table 3.5 summarizes the maximum temperature obtained in the cable and in the Al protective shell with different delay times. Figure 3.11 shows the current discharge profile in the coil. It is confirmed that the addition of EE in the loop accelerates the current discharge in the coil.

Table 3.5 – CD1 peak temperature at 15.5 kA after 100 ms, when magnet is protected by both EE and CLIQ in the circuit, but initiated with different delay times.

| $t_{EE}$ [ms] | $T_{cable}$ [K] | $T_{Al\ shell}$ [K] |
|---------------|-----------------|---------------------|
| 10            | 72.7            | 112.9               |
| 20            | 104.4           | 114.6               |
| 30            | 123.5           | 123.5               |

The voltage to ground is calculated as the sum of the voltage on the magnet coils and voltage on the rest of the circuit. The voltage to ground in the circuit at 15.5 kA is illustrated in Figure 3.12a, when CLIQ and EE are initiated at the same time or with a 20 ms delay time. The initial voltage value (620 V) is because we set up the current in the magnet as illustrated in Figure 3.4a in ANSYS, which relies on the current level (15.5 kA) and the connected dump resistor value (40 m $\Omega$ ). A high voltage is observed when both protection systems are turned on at the same time. When the EE is initiated after a delay time of 20 ms, the voltage rise due to EE is also delayed, which can be seen in Figure 3.12a. A zoom at the beginning of the simulation

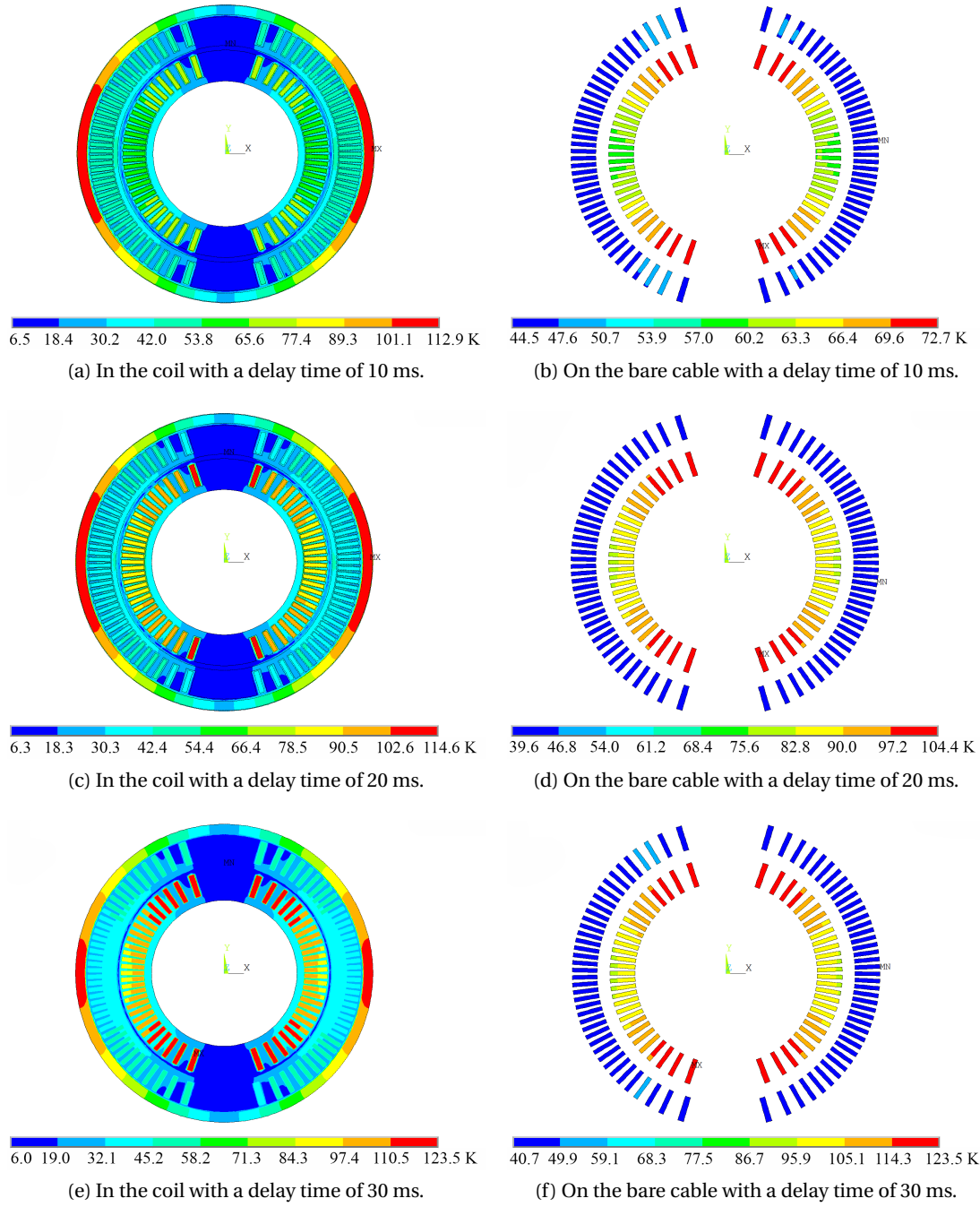


Figure 3.10 – CD1 temperature distribution at 15.5 kA after 100 ms, with both EE and CLIQ in the circuit, but initiated with different delay times.

is shown in Figure 3.12b. The voltage drops to zero between 0 and 10  $\mu$ s is because once we set up the current in the coil, the voltage (i.e., power supply) is switched off with a piecewise linear function. Then between 10  $\mu$ s and 20  $\mu$ s, CLIQ is turned on, therefore a voltage rise is observed.



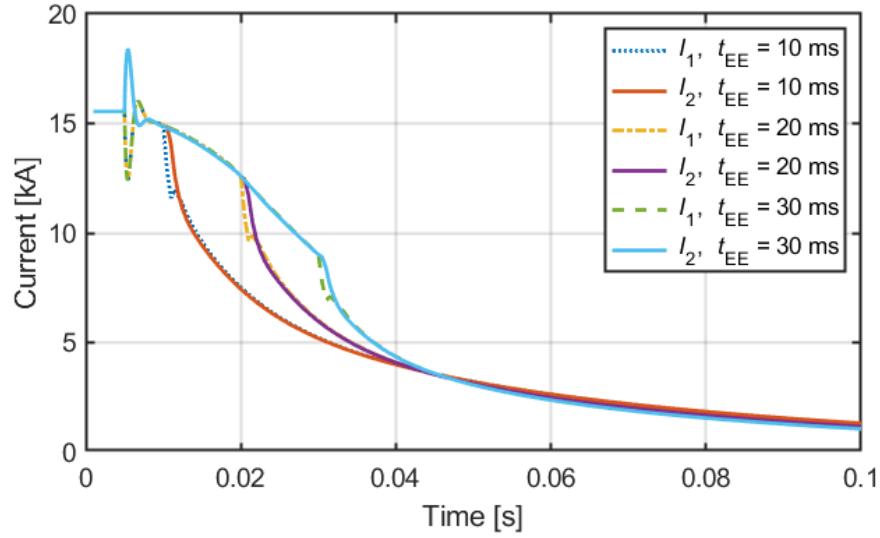


Figure 3.11 – Current profile comparisons at 15.5 kA, when the CD1 is protected by both EE and CLIQ in the circuit, but initiated with different delay times.

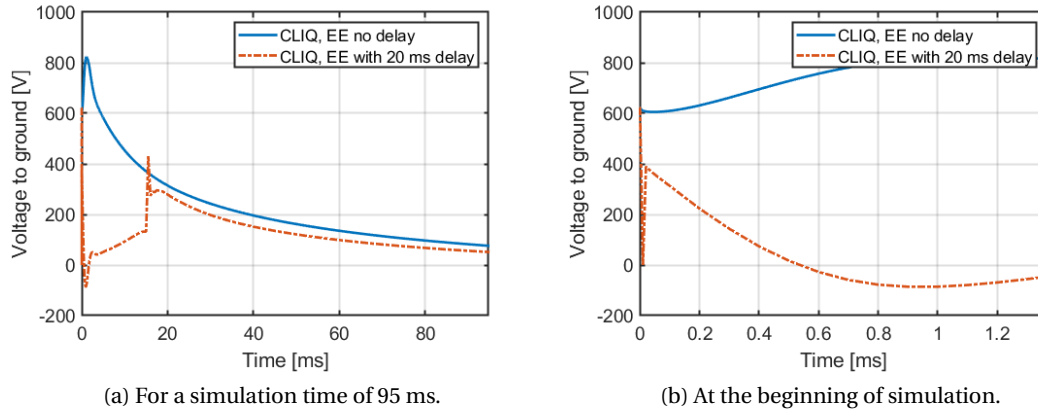


Figure 3.12 – CD1 voltage to ground in the circuit at 15.5 kA, when CLIQ and EE are initiated at the same time or with a delay time of 20 ms.

We investigate here the performance of protection methods from 4.2 K without considering the temperature rise during the quench detection phase, as CLIQ experiments on CD1 are foreseen to be carried out on current plateaus without a spontaneous quench. The peak temperature in the cable and coil at different currents are listed in Table 3.6 with only CLIQ and both EE and CLIQ with a delay time of 20 ms. With only CLIQ, the peak temperatures are observed in the cable pole turn regions. With both of them, the highest temperatures are found in the Al protective shell where the eddy currents are the strongest. This can be explained by the lower resistivity of the Al shell with respect to the aluminum-bronze former. The addition of EE in the loop significantly decreases the temperature in the pole turn regions.

Table 3.6 – CD1 peak temperature at different current levels after 100 ms, when magnet is protected by only CLIQ, and by both EE and CLIQ in the circuit, but initiated with a delay time of 20 ms.

| $I$ [A] | $B_{\text{bore}}$ [T] | CLIQ                   |                       | CLIQ+EE                |                       |
|---------|-----------------------|------------------------|-----------------------|------------------------|-----------------------|
|         |                       | $T_{\text{cable}}$ [K] | $T_{\text{coil}}$ [K] | $T_{\text{cable}}$ [K] | $T_{\text{coil}}$ [K] |
| 15545   | 8.9                   | 148.1                  | 148.1                 | 104.4                  | 114.6                 |
| 12653   | 7.3                   | 152.4                  | 152.4                 | 71.2                   | 93.8                  |

### 3.3.4 Peak temperature estimation

In a further study, we initiate one cable area, e.g., the first turn on the pole region of the inner layer, to the quenched state after a static solution of 5 ms. The initial condition of temperature for all the other single-turn areas remains to be  $T = 4.2$  K. We let the simulation run for the detection time calculated in Subsection 3.2.3, then we turn on the protection system. In this way, we are able to include the temperature rise during the quench detection phase. The detection time calculated in Table 3.3 is used in the coupled simulation with only CLIQ in the circuit.

A peak temperature of 319 K is obtained when we operate at 86% of the  $I_{\text{ss}}$ , which is 15.5 kA, while a peak temperature of 351 K is reached at 90% of the  $I_{\text{ss}}$ , which is 16.3 kA. If we compare these values with those in Table 3.3 when the magnet is protected only by EE, we observe a higher peak temperature in the case when the magnet is protected only by CLIQ. The obtained peak temperature results are close to the maximum allowed temperature 350 K in the system. In other words, it might be not sufficient when there is only CLIQ in the circuit to protect the CD1 model magnet at high current. That also implies that we put the EE system in the loop for safety reasons. Note, however, that the CLIQ parameters used for this study are not optimized for minimal peak temperatures and voltages.

### 3.3.5 CLIQ optimization

The CLIQ simulation study using LBNL's unit was previously presented. As that CLIQ unit is not optimized for CD1 protection, therefore in this subsection, we are seeking for a proper combination of CLIQ system parameters (charging voltage  $V_C$  and internal capacitance  $C_C$ ) to allow protecting the magnet at both low and high current using CLIQ as the only quench protection system.

The optimization study is conducted with the geometry of CD1, but with two different lengths, to evaluate the CLIQ protectability for selected CLIQ parameters. The first case is a short magnet, i.e., CD1 model magnet with a magnetic length of about 0.6 m. The second case is a long magnet, i.e., a full-scale FCC dipole magnet with a magnetic length of about 14.3 m.

We evaluate the quench protection for these two cases at different current levels. At high

current, low energy is needed to start a quench due to high energy density and fast quench propagation in the magnet. However at low current, high energy is needed to start a quench due to low energy density and slow quench propagation in the magnet. Quench protection at low-medium current could be challenging, since in this current range the margin to trigger a quench is significantly higher than the case of the nominal current, which requires more power and more energy to quench.

Prior to the CLIQ quench protection studies, the characteristics of a CLIQ discharge will be analyzed to evaluate the impact of varying CLIQ parameters on the quench protection performance.

#### Characteristics of a CLIQ discharge

For a given magnet and a given connection scheme of the CLIQ unit, the introduced current in the magnet after triggering depends on the characteristic parameters of the CLIQ unit. By changing these parameters, e.g., charging voltage  $V_C$  and internal capacitance  $C_C$ , we can assess their impact on the quench protection performance. A comparison of the induced current  $I_C$  in the CD1 coil at 15.5 kA after 5 ms is illustrated in Figure 3.13.

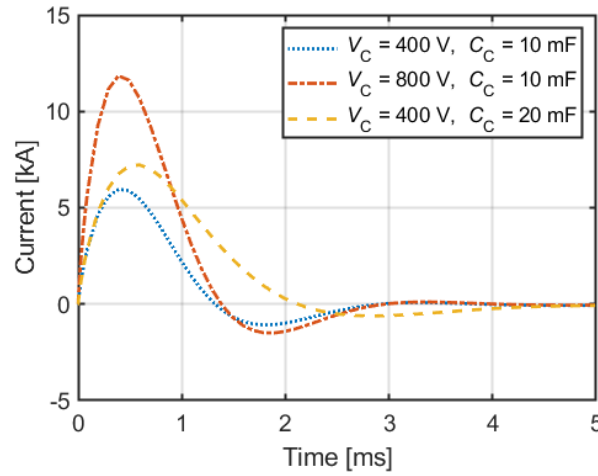


Figure 3.13 – Comparison of induced current  $I_C$  by CLIQ in the CD1 coil at 15.5 kA for different combinations of charging voltage  $V_C$  and internal capacitance  $C_C$ .

The induced current is given by  $I_C(t) = C_C \cdot dV_k(t)/dt$ , where  $V_k$  is the voltage across the capacitor  $C_C$ . The amplitude of the induced current is proportional to the charging voltage since  $V_k \propto V_C$ . The peak value of the induced current is reached after a quarter of oscillation and it can be approximated as

$$I_{C,peak} \approx V_C \sqrt{\frac{C_C}{L_{eq}}} \quad (3.1)$$

where  $L_{eq}$  is the equivalent inductance of the magnet. The formula is simply the inductance of two parallel opposing inductors, written as

$$L_{eq} = \frac{L_1 \cdot L_2 - M_{12}^2}{L_1 + L_2 + 2M_{12}} \quad (3.2)$$

where  $L_1$  and  $L_2$  are respectively the self-inductance of the coil branches 1 and 2, and  $M_{12}$  is their mutual inductance.

The initial current change is a key parameter of the CLIQ performance, and it can be approximated as

$$\frac{dI_C}{dt}(0) \approx \frac{V_C}{L_{eq}} \quad (3.3)$$

The initial current change does not depend on the capacitance. It is confirmed in Figure 3.13 that the initial current change rate is the same when a doubled value of capacitance is applied, with the same charging voltage.

According to the studies presented in [40, 71], we know that a large fraction of the stored energy in the CLIQ unit is deposited in the coil windings during the first current oscillation. Much of this energy is converted to heat which serves to quench the coil. For this reason, the CLIQ performance depends mainly on the initial peak power deposition. As the peak power loss is proportional to  $(V_C/L_{eq})^2$ , one can increase the charging voltage, without exceeding the maximum allowed voltage to ground in the circuit, to ensure the protection performance in the case of long magnets with a large inductance.

For a given magnet and a given CLIQ configuration, the internal capacitance of a CLIQ unit determines the time period of the current oscillations, as outlined in the equation

$$t_w = 2\pi\sqrt{L_{eq}C_C} \quad (3.4)$$

The total stored energy in the CLIQ unit depends on the charging voltage and capacitance, given by  $E_{CLIQ} = \frac{1}{2}C_C V_C^2$ . Therefore the peak power deposition lasts for a longer time with a larger value of capacitance.

For the CD1 magnet at 15.5 kA, we have  $L_1 = 0.234$  mH,  $L_2 = 0.465$  mH, and  $M_{12} = 0.263$  mH. With Eq. (3.2), we can calculate the CD1 equivalent inductance, which is  $L_{eq} = 0.032$  mH. The mentioned equations are used to calculate the current oscillation period length, induced current peak amplitude and initial current change rate in order to estimate the CLIQ performance. Take an example of the CLIQ unit of 400 V and 10 mF, the simulation results shown in Figure 3.13 give  $t_w \approx 3$  ms and  $I_{C,peak} \approx 6$  kA, while the numerical estimates using the above equations give respectively 3.6 ms and 7 kA. The estimated values are slightly higher than the simulation results, but they are still good for comparison. Regarding the initial current change rate, the simulation result is slightly higher than the estimated value, but both of them have the same order of magnitude. This is due to the wrong time constant in the homogenized

model, as explained in Subsection 2.5.3.

Figure 3.14 shows a comparison of the temperature distribution on the CD1 bare cable at 15.5 kA after 5 ms, when the magnet is protected by only CLIQ, for the same combinations of charging voltage  $V_C$  and internal capacitance  $C_C$ , as used in Figure 3.13.

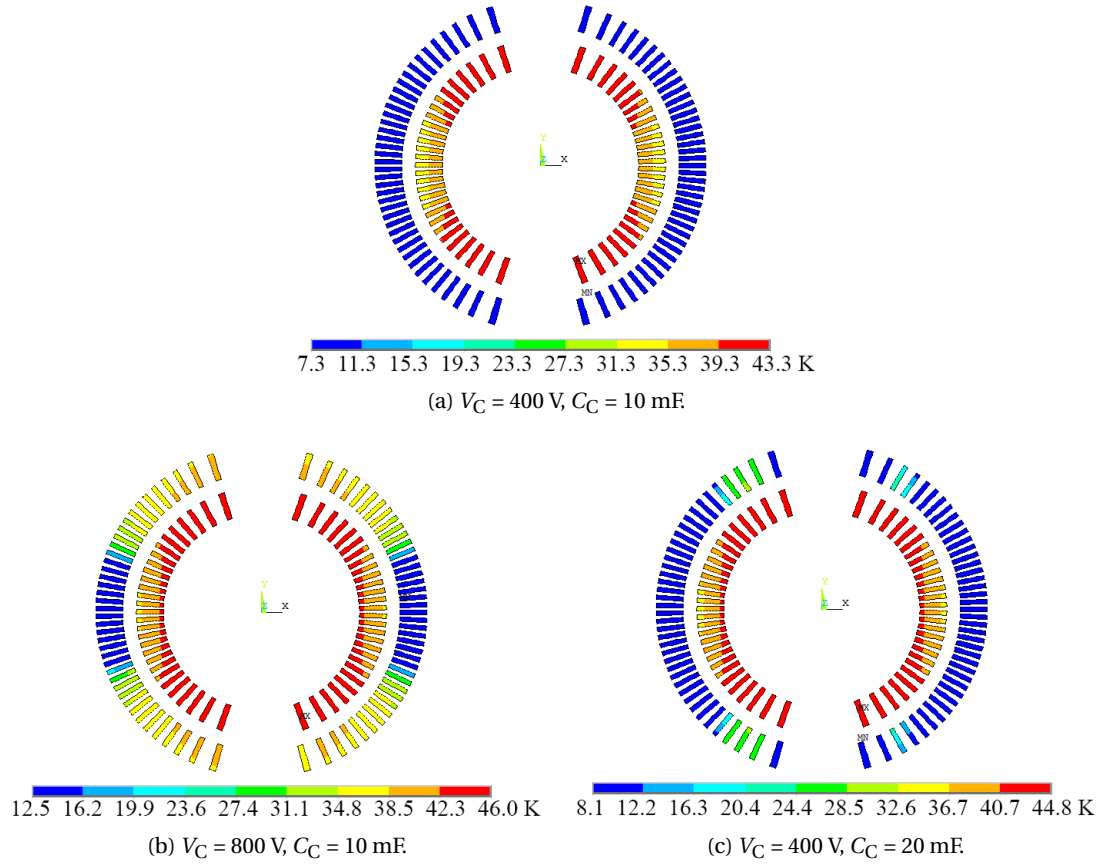


Figure 3.14 – CD1 temperature distribution on the bare cable at 15.5 kA after 5 ms, when magnet is protected by only CLIQ, for different combinations of charging voltage  $V_C$  and internal capacitance  $C_C$ .

From this figure, we find a very close peak temperature in the conductor after 5 ms of the current oscillation for different combinations of charging voltage  $V_C$  and internal capacitance  $C_C$ . Increasing the capacitance value can quench a few more cable turns due to a longer time for the peak power deposition. A higher charging voltage can quickly quench a big fraction of the conductor, resulting in a higher temperature distribution in the overall coil cross section. However, it is worth noting that the charging voltage of a CLIQ unit imposes directly a certain voltage to ground, which is limited by the coil circuit design for safety and risk reduction considerations.

### Case of a short magnet

In this paragraph, the optimization study using different CLIQ parameters on the CD1 with a magnetic length of 0.6 m is discussed.

#### Lowest current level for CD1 self-protection

Typically we design a quench protection system to protect the magnet in all operating conditions, unless it can be demonstrated that the magnet is self-protected. For example, at very low current some coils might recover from a quench, or at low current some coils develop sufficient quench resistance to slowly, but safely, discharge the magnet current. Each magnet is different and should be studied independently. For the short magnet CD1, the lowest current level for self-protection is 1.4 kA, i.e., 9% of its nominal current. This value is obtained based on a study via a quench propagation simulation and a calculation of current decay using the adiabatic integrator. Figure 3.15 shows the temperature profile in the centre of cable, along the coil at different times and the current discharge in the magnet with the growing quench resistance. The magnet is proved to be self-protected after the current discharge as the peak temperature in the coil is smaller than 350 K.

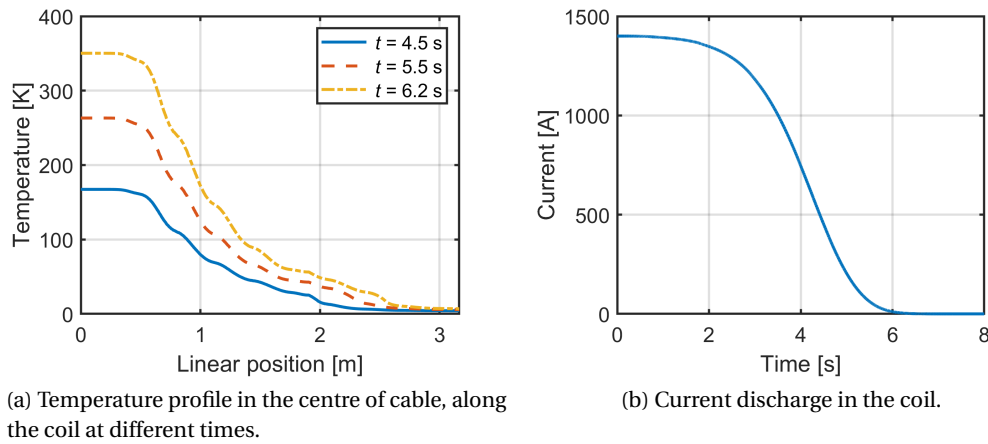


Figure 3.15 – Quench propagation simulation results of a 5-turn CD1 helical model at 1.4 kA for determination of the lowest current level to be self-protected.

#### LBNL CLIQ unit with increased charging voltage

In the previously presented CLIQ simulation in Subsection 3.3.2, we remark that a CLIQ unit with 400 V and 10 mF cannot bring down the current in the coil in the case at 10.8 kA, as shown in Figure 3.7. Indeed, the power supply of the CLIQ unit at LBNL can be charged up to 800 V.

This indicates that one can protect the magnet down to a lower current level. Such a CLIQ unit with 800 V and 10 mF is able to protect the coil down to 5.7 kA. Figure 3.16 illustrates a comparison of current decay curve at different current levels.

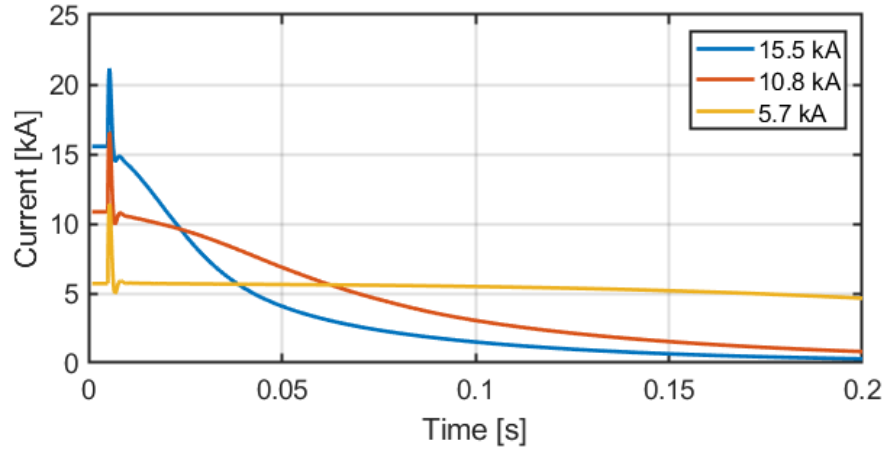


Figure 3.16 – Current discharge in the CD1, when magnet is protected by a CLIQ system of 800 V and 10 mF.

By fixing the peak temperature of 350 K in the coil and using the obtained current decay curves in Figure 3.16, one can compute, via a MIITs calculation, the total time budget before the discharge, which is written as  $t_d = \Delta t_{\text{thres}} + \Delta t_{\text{val}} + \Delta t_{\text{switch}}$ . The results are listed in Table 3.7.

Table 3.7 – Estimation of time budget by MIITs calculation, when the CD1 is protected by a CLIQ system of 800 V and 10 mF.

| $I$ [kA] | $t_{d,\text{ref}}$ [ms] |
|----------|-------------------------|
| 15.5     | 24.6                    |
| 10.8     | 51.2                    |
| 5.7      | 125.6                   |

If we compare  $t_{d,\text{ref}}$  with  $t_d$  obtained in Table 3.3, we remark that the magnet is safe at 15.5 kA, but not at 10.8 kA when we use a threshold of 500 mV in case of a voltage detection. In fact, the voltage threshold should be chosen carefully for each current because the quench propagation speed is different in Nb<sub>3</sub>Sn CCT magnets for different excitation levels, as shown in Table 3.3. Typically we adapt the pre-set threshold  $V_{\text{thres}}$  with the current level and add a validation time  $\Delta t_{\text{val}}$  at low current to avoid false trigger caused by flux jumps and noise. Thus for different current ranges, different combinations of  $V_{\text{thres}}$  and  $\Delta t_{\text{val}}$  are selected to constitute  $t_d$ .

A lower voltage threshold with some validation time can be used, along with this CLIQ unit to protect the magnet for the current range from 5.7 to 15.5 kA. As  $t_{d,\text{ref}}$  at low current (< 2 kA) is missing with a CLIQ unit of 800 V and 10 mF, a complete combination will be proposed later based on an optimized CLIQ unit applied to the CD1.

### Optimized CLIQ unit

Since the lowest current level for self-protection of CD1 is found to be 1.4 kA, the optimized CLIQ parameters will be selected in order to protect the magnet from this lowest value up to its nominal current.

As discussed before, the CLIQ charging voltage has a direct impact on the voltage to ground, which is limited by the circuit design. However, there is no obvious limitation in increasing the internal capacitance. It is worth noting that a big capacitance occupies more physical space for installation. So far the produced CLIQ units had a capacitance between 1 and 80 mF. A typical CLIQ unit of 40 mF and 1 kV has an approximate size of 50 cm in length, 50 cm in width and 100 cm in height, as a standard electronic rack.

With a capacitance of 40 mF, a charging voltage of 700 V is required to protect a short CD1 model magnet. If the capacitance is further increased to 80 mF, then the charging voltage can be reduced to 620 V. The simulation are run at four current levels: 1.4, 6.0, 10.8 and 15.5 kA to evaluate the protection performance at low, medium and high current. These values are respectively 8%, 33%, 60% and 86% of the short sample current, where the last one is the nominal current.

The same kind of study on the total time budget before the current discharge is conducted for these two CLIQ units at different current levels by fixing the maximum temperature of 350 K in the coil and using the obtained current decay profiles from simulation. The results are listed in Table 3.8.

Table 3.8 – Estimation of time budget by MIITs calculation, when the CD1 is protected by a CLIQ system of 700 V and 40 mF, or of 620 V and 80 mF.

| $t_{d,ref}$ [ms] | CLIQ: 700 V, 40 mF | CLIQ: 620 V, 80 mF |
|------------------|--------------------|--------------------|
| $I = 15.5$ kA    | 23.9               | 23.3               |
| $I = 10.8$ kA    | 59.0               | 55.2               |
| $I = 6.0$ kA     | 216.4              | 207.5              |
| $I = 1.4$ kA     | 6030.6             | 4913.3             |

If we compare the values of  $t_{d,ref}$  for both CLIQ units, a longer time budget is obtained with the CLIQ of 700 V, 40 mF. It is confirmed again that increasing the CLIQ charging voltage has a bigger effect than increasing the internal capacitance on the peak temperature reduction after a quench.

Using the CLIQ unit of 700 V, 40 mF as an example, a combination of  $V_{thres}$  and maximum  $\Delta t_{val}$  is proposed in Table 3.9 for different current levels. The time needed to reach the threshold is also listed in this table following the quench propagation simulation described in Section 2.4. To be conservative, a switch time  $\Delta t_{switch}$  of 5 ms is assumed to turn on the quench protection system.



### 3.3. Coupling-Loss Induced Quench

Table 3.9 – Proposed combination of voltage threshold, time to reach threshold, maximum validation time and switch time at different current levels when the CD1 is protected by a CLIQ system of 700 V and 40 mF

| $I$ [kA] | $V_{\text{thres}}$ [mV] | $\Delta t_{\text{thres}}$ [ms] | $\Delta t_{\text{val,max}}$ [ms] | $\Delta t_{\text{switch}}$ [ms] | $t_{\text{d,ref}}$ [ms] |
|----------|-------------------------|--------------------------------|----------------------------------|---------------------------------|-------------------------|
| 15.5     | 500                     | 15                             | 3.9                              | 5                               | 23.9                    |
| 10.8     | 100                     | 27                             | 27.0                             | 5                               | 59.0                    |
| 6.0      | 100                     | 113                            | 98.4                             | 5                               | 216.4                   |
| 1.4      | 100                     | 2912                           | 3113.6                           | 5                               | 6030.6                  |

With the assumption of 20 ms for the total time before current discharge, as presented in Table 3.3, the estimated peak temperatures are around 290 K at CD1 nominal current level for both proposed optimized CLIQ units and they are well below the limit of 350 K. For other current levels, a sufficient validation time is observed for detecting a quench, in addition to the time to reach the voltage threshold. If we summarize, both combinations of CLIQ parameters (700 V, 40 mF and 620 V, 80 mF), are well sufficient and efficient to protect the CD1 model magnet in case of a quench.

#### Case of a long magnet

In order to have further insights of CLIQ protection performance in an accelerator magnet, we study here the case using the CD1 geometry but with a magnetic length of 14.3 m, which is the length of an FCC dipole. Since the stored energy in this long magnet is approximately 24 times of that in the CD1 short magnet with a magnetic length of 0.6 m, the lowest current level for self-protection would be much lower due to the same quench propagation speed. In this situation, designing a proper CLIQ unit for an FCC CCT magnet could be difficult as large unrealistic CLIQ parameters would appear. A value of 1 kA was used as the lowest current level for the CLIQ protection studies, following the reasoning for other 16 T FCC-hh dipole magnets [47, 48]. This assumed value was selected because a similar assumption was made for the protection of LHC dipole magnets. In addition, a quench at such low current levels was never observed.

In this study, we fix the boundaries of the CLIQ parameters to find out the lowest current level that we can still protect the magnet with a realistic CLIQ unit. Based on [47], a charging voltage of 1.2 kV is selected to maintain the protection performance in case of a long magnet with a large inductance. Regarding the capacitance, we know that its value can be increased, if needed, to protect a longer or a more challenging magnet. However, a higher capacitance signifies a larger unit size and it would be inconvenient to use and integrate in the accelerator tunnel. It is also worth noting that the current decays after a first current oscillation induced by the CLIQ unit. Therefore, a bigger capacitance can result in a higher hot-spot temperature after a quench as the capacitance changes the current oscillation frequency. This is crucial for quench protection at high current. Thus we select the capacitance value in a way that the

estimated peak temperature at the nominal current after a quench is below 350 K. The chosen CLIQ unit has a charging voltage of 1.2 kV and a capacitance of 50 mF.

With this unit, we can protect the magnet down to a current level of approximately 1 kA. Table 3.10 outputs the total time budget before the current discharge and a proposed combination of  $V_{\text{thres}}$  and maximum  $\Delta t_{\text{val}}$  for different current levels, when the peak temperature is fixed to be 350 K in the coil and using the obtained current decay profiles from the coupled simulation. The time needed to reach the threshold is obtained via a quench propagation simulation and we assume always the same switch time  $\Delta t_{\text{switch}}$  of 5 ms. The validation time margin observed in the table for detecting a quench, in addition to the time to reach the voltage threshold, is sufficient and efficient to protect a long magnet with the geometry of CD1 by a CLIQ unit of 1.2 kV and 50 mF for the current range from 1.0 to 15.5 kA in case of a quench.

Table 3.10 – Proposed combination of voltage threshold, time to reach threshold, maximum validation time and switch time at different current levels, when a magnet having the CD1 geometry with a magnetic length of 14.3 m, is protected by a CLIQ system of 1.2 kV and 50 mF.

| $I$ [kA] | $V_{\text{thres}}$ [mV] | $\Delta t_{\text{thres}}$ [ms] | $\Delta t_{\text{val,max}}$ [ms] | $\Delta t_{\text{switch}}$ [ms] | $t_{\text{d,ref}}$ [ms] |
|----------|-------------------------|--------------------------------|----------------------------------|---------------------------------|-------------------------|
| 15.5     | 500                     | 15                             | 0                                | 5                               | 20.0                    |
| 10.8     | 100                     | 27                             | 9.1                              | 5                               | 41.1                    |
| 6.0      | 100                     | 113                            | 69.8                             | 5                               | 187.8                   |
| 1.0      | 100                     | 5773                           | 4602.0                           | 5                               | 10380.0                 |

### 3.4 Co-wound copper tape

The quench protection method by adding a co-wound copper tape beneath the superconducting cable in the channel is explained in this section. The goal of the co-wound copper tape is to dissipate a portion of the stored energy in the low-cost tape. As a consequence, the amount of copper in the strands can be reduced in favor of the amount of superconductor. We aim to find out if, in this way, the number of strands in the coil can be reduced to improve the efficiency in terms of usage of conductor<sup>1</sup>. It is worth noting that the co-wound copper tape is an add-on protection method as this solution is far from being sufficient to protect the magnet. It can be used when accompanied by another quench protection system to further accelerate the current discharge in the coil.

There are two variables in this study: the cuNc ratio in the strand and the co-wound copper tape thickness  $t_{\text{cu}}$ . The co-wound copper tape width is kept the same as the superconducting cable to fit in the channel. When changing the cuNc ratio, the number of strands is recalculated to keep the same current density in the superconducting material, leading to a change in cable dimension. If the cuNc ratio decreases, there is more superconductor than copper, supposing

<sup>1</sup>As this study is not generic for other magnets, the equations involved are described specifically in this section.

the same number of strands, thus the strand number should be reduced.

The new number of strands in a superconducting cable is calculated as

$$n_{s,n} = \frac{4A_{sc}}{\pi d_s^2 f_{sc,n}} \quad (3.5)$$

where  $n$  denotes new,  $d_s$  is the strand diameter, and  $f_{sc,n}$  the new superconductor fraction in a strand, which is defined as  $f_{sc,n} = 1/(1 + cuNc_n)$ , where  $cuNc_n$  is the new  $cuNc$  ratio in the strand. Note that the calculated value of  $n_{s,n}$  is rounded to the nearest positive integer.

As the cable thickness is assumed to be constant, with a small  $cuNc$  ratio, the cable width can be reduced. The new cable width is computed as  $c_{l,n} = c_l \cdot n_{s,n}/n_s$ , where  $c_l$  is the nominal cable width and  $c_{l,n}$  the new cable width.

Since we reduce the copper fraction in the strand, we have to compensate this fact by adding a co-wound copper tape to have enough material to dissipate a portion of the stored energy in case of a quench. The co-wound copper tape cannot be too thin to avoid high temperatures in it. In principle, there is no limitation on the copper tape thickness as long as the total amount of superconductor is reduced. However, adding a copper tape on the inner layer shifts the outer layers away from the aperture and makes the use of superconductors less efficient, leading to an increase in the cost. With these restrictions, a maximum copper tape thickness of 1 mm is used in this study. The feasibility of the co-wound copper tape is studied in a two-layer case, which is CD1.

The electrical circuit of the co-wound copper tape protection method is illustrated in Figure 3.17. The mutual coupling of primary and secondary is taken into account for solving the current in both circuits using the adiabatic-integrator method. To distinguish physical parameters, we denote the primary circuit as 1 and the secondary as 2. The resistance in the primary circuit equals the quench resistance ( $R_1 = R_{quench}$ ).

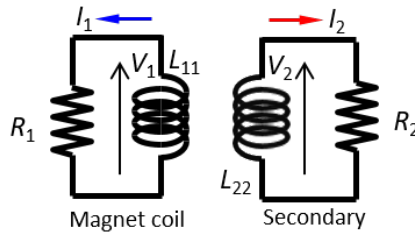


Figure 3.17 – Electrical circuit of inductive protection using a co-wound copper tape for the CD1.

The voltage on the coil ( $V_1$ ) and on the co-wound tape ( $V_2$ ) can be expressed by:

$$\begin{cases} V_1 = L_{11} \frac{dI_1}{dt} + M_{12} \frac{dI_2}{dt} = -R_1 I_1 \\ V_2 = M_{21} \frac{dI_1}{dt} + L_{22} \frac{dI_2}{dt} = -R_2 I_2 \end{cases} \quad (3.6)$$

Several approximations are made in this calculation. First, the inductance of superconducting cable and co-wound tape are considered to be the same:  $L_{11} = L_{22} = L$ , since both of the cable and tape follow the same winding form. Meantime, we know that the mutual inductance is the same on both sides:  $M_{12} = M_{21} = M$ . As these two circuits are extremely close to each other, ideally we can say  $M = L$ , nevertheless, a mutual coupling coefficient is added to maintain the system stability. This coefficient is computed in a ROXIE simulation. Thus we get a new relationship:  $M = 0.95L$ . The nonlinear coil inductance, extracted from Opera, is considered for calculation.

The implicit finite difference method is applied to solve the differential equations (3.6). If we write the system in the form of a matrix<sup>2</sup>, we have:

$$\frac{1}{\Delta t} \bar{L} \Delta I + \bar{R} I(t_n) = 0 \quad (3.7)$$

The backward difference is used to maintain the numerical stability, thus  $\Delta I = I(t_n) - I(t_{n-1})$ .  $n$  signifies the number of time substep. The system becomes:

$$\frac{1}{\Delta t} \bar{L} \Delta I + \bar{R} (I(t_{n-1}) + \Delta I) = 0 \quad (3.8)$$

After rearrangements, the current at instant  $n$  can be represented by one at the previous instant  $n - 1$ :

$$I(t_n) = -(\bar{L} + \Delta t \bar{R})^{-1} \Delta t \bar{R} I(t_{n-1}) + I(t_{n-1}) \quad (3.9)$$

with

$$I(t) = \begin{pmatrix} I_1(t) \\ I_2(t) \end{pmatrix}, \quad \bar{L}(t) = \begin{pmatrix} L(t) & 0.95L(t) \\ 0.95L(t) & L(t) \end{pmatrix}, \quad \bar{R}(t) = \begin{pmatrix} R_1(t) & 0 \\ 0 & R_2(t) \end{pmatrix} \quad (3.10)$$

Without any consideration on heat diffusion, the heat balance equation in both circuits is developed as:

$$\begin{cases} A_{\text{cab}} c_{v,\text{cab}} \frac{\partial T_1}{\partial t} = A_{\text{cu},1} \left( \frac{I_{\text{cu}}}{A_{\text{cu},1}} \right)^2 \rho_{\text{cu}} \\ A_{\text{cu},2} c_{v,\text{cu}} \frac{\partial T_2}{\partial t} = A_{\text{cu},2} \left( \frac{I_2}{A_{\text{cu},2}} \right)^2 \rho_{\text{cu}} \end{cases} \quad (3.11)$$

where  $A$  is the cross-section area. After some arrangements, the temperature at instant  $n + 1$  can be estimated based on the previous one  $n$  with small steps. The temperature evaluation for two circuits are:

$$\begin{cases} T_{1,n+1} = T_{1,n} + \frac{\rho_{\text{cu}} I_{\text{cu}}^2 \Delta t}{c_{v,\text{cab}} A_{\text{cab}} A_{\text{cu},1}} \\ T_{2,n+1} = T_{2,n} + \frac{\rho_{\text{cu}} I_2^2 \Delta t}{c_{v,\text{cu}} A_{\text{cu},2}^2} \end{cases} \quad (3.12)$$

---

<sup>2</sup>A variable with a bar on top means that it is a matrix.

We are studying the co-wound tape on the CD1 model magnet as a first check whether the tape could be useful to save conductor in a Nb<sub>3</sub>Sn high-field CCT magnet. The nominal cuNc ratio of CD1 is 1.15, considered as reference. According to [69], the minimum allowable cuNc value 0.8 is used for calculation, limited by superconductor stability reasons and strand fabrication restrictions [93, 94].

With the initial conditions or results of the last time step, we can update the material properties, resistance and inductance values for solving the mutual coupling matrix to obtain new currents and evaluate new temperatures. The initial condition of current is  $I_1(t=0) = I_{op} = 15.5$  kA and  $I_2(t=0) = 0$  with  $B(t=0) = 9.3$  T. In this analysis, it is assumed that the entire magnet is quenched. Thus the initial temperature is set right above  $T_{cs}$ . The  $B$ -field scaling law is done based on the sum of  $I_1$  and  $I_2$ . In this study, no current-sharing regime is considered for simplicity. We reach  $T_{cs}$  at the beginning of the simulation, and the total current goes into the stabilizer. The reference without co-wound tape can be obtained with the initial cuNc ratio, and zero width in the co-wound tape.

The simulation with and without co-wound tape are carried out in MATLAB. Three different cables are involved in the calculation. The first one is the nominal cable used in the CD1. Cable A and B have three fewer strands than the nominal cable. Both of them have the same cuNc ratio, number of strands, cable width, and co-wound copper tape thickness. The only difference is that the co-wound copper tape length  $L_{tape}$  in Cable B is 30% longer than the one in Cable A. By extending the length of the copper tape, we increase the copper resistance, and therefore the maximum temperature can be reduced in the tape. In reality, we can keep the same length of the co-wound copper tape with respect to the cable. The functionality of the extra 30% longer tape can be achieved by adding a resistor to the co-wound tape of an equal value.

The parameters of these cables are listed in Table 3.11, with  $L_{tape}/L_{cab}$  as the longitudinal length factor between the co-wound copper tape and superconducting cable. It is worth noting that the amount of the conductor required for the FCC dipoles is approximately 10 kt. The reduction of three strands indicates 14% less mass of superconducting cable, i.e., over 1 kt of conductor. As the conductor is the most expensive component of the magnet system [9], this would yield significant savings.

Table 3.11 – Cable parameters for inductive protection study in a two-layer CCT.

| Cable   | cuNc | $n_s$ | $c_l$ [mm] | $L_{tape}/L_{cab}$ | $t_{cu}$ [mm] |
|---------|------|-------|------------|--------------------|---------------|
| Nominal | 1.15 | 21    | 9.85       | 1                  | 0             |
| A       | 0.8  | 18    | 8.4        | 1                  | 1             |
| B       | 0.8  | 18    | 8.4        | 1.3                | 1             |

Figure 3.18 shows the variation of current and temperature with time for the nominal cable and Cable A while Figure 3.19 shows the results for the nominal cable and Cable B. At the beginning of the simulation displayed in Figure 3.18,  $T_1$  increases faster due to the generated

quenching heat in primary ( $T_1 > T_2$ ). After a few milliseconds, the balance is established ( $T_1 = T_2$ ), when we observe a reduction in  $I_1$  and an increase in  $I_2$ . After that,  $T_2$  becomes higher than  $T_1$  because more heat is generated in secondary ( $T_1 < T_2$ ). Moreover, the tape has a smaller surface area, so it heats up faster.

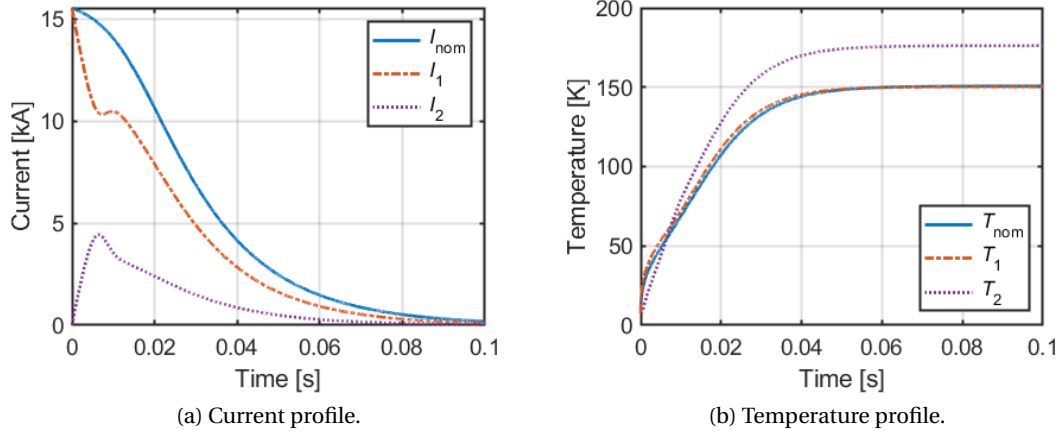


Figure 3.18 – Comparisons of current and temperature profiles, between the nominal CD1 cable, and the Cable A with a co-wound copper tape.

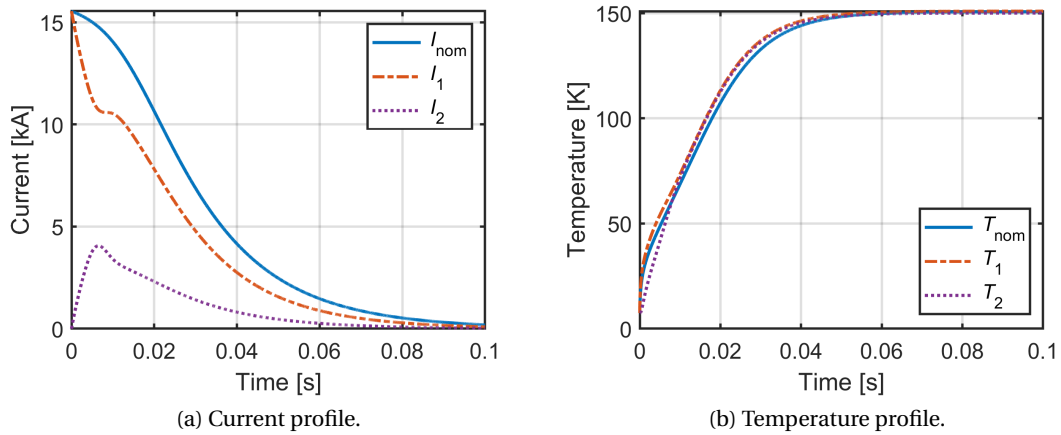


Figure 3.19 – Comparisons of current and temperature profiles, between the nominal CD1 cable, and the Cable B with a co-wound copper tape.

In general, we can remark from the results that by introducing a co-wound copper tape, a faster current decay is observed in the coil rather than the nominal case. The variation of  $T_1$  and  $T_{nom}$  are very similar because the effect of reducing the number of strands (temperature increase) and adding the copper tape (temperature drop) are balanced here. If we keep the same length for the cable and co-wound tape, a difference of temperature ( $T_2 > T_1$ ) is observed at the end of the current decay. By increasing the length of the co-wound copper tape, we could avoid a higher temperature in the secondary loop.

The simulation results are verified by comparison of stored magnetic energy and energy extracted on all the resistances.

$$W = \int_0^t (R_1 I_1^2 + R_2 I_2^2) dt = 0.21 \text{ MJ} \quad (3.13)$$

At 15.5 kA, the MIITs are computed for a maximum temperature of 350 K for the listed cables. The estimation of the time budget is presented in Table 3.12. For the case with a co-wound copper tape, the remaining time for detection and actuation 14 ms is very short compared to the nominal case. It is worth noting that in cables with a reduced number of strands, the quench propagation may be faster, but the quench resistance is also reduced for voltage detection due to a smaller fraction of copper in the conductor.

Table 3.12 – Estimation of time budget by MIITs calculation, when the CD1 is protected by a co-wound copper tape. MIITs is the total value from the quench detection to the end of current decay whereas MIITs<sub>decay</sub> is the value for the current decay after quench detection.

| Cable   | MIITs [MA <sup>2</sup> s] | MIITs <sub>decay</sub> [MA <sup>2</sup> s] | t <sub>d</sub> [ms] |
|---------|---------------------------|--|---------------------|
| Nominal | 10.7                      | 5.0  | 23.6                |
| A       | 6.3                       | 2.9  | 14.0                |
| B       | 6.3                       | 2.9  | 14.0                |

In this table, the MIITs accumulated during the current decay is significantly reduced using the co-wound tape. However, the addition of the tape cannot help during the detection phase when the primary current is constant. Moreover, the envisaged reduction in the number of strands leads to a faster temperature rise in the quenched portion of the cable. We, therefore, study the reduction in the detection time budget in the above cases. To conclude, the co-wound tape approach is interesting only if the MIITs accumulated during the detection phase are significantly smaller than those accumulated during the current decay, i.e., if a very efficient quench detection is available. This protection method is not used for the CD1 model magnet.





## 4 Quench Detection

### 4.1 Goals and overview

In this chapter, we aim to investigate the feasibility of three different detection methods, current, voltage and optical detection using co-wound wires, described in Subsection 1.6.1. This is a first-of-a-kind study on detection times for Nb<sub>3</sub>Sn magnets. The current detection method is studied through a subscale experiment and compared to the simulation, in Section 4.2. The implementation of the other two detection methods, voltage and optical detection were tried out on the CD1 coil, outlined in Section 4.3. The final CD1 configuration for cryogenic test is given at the end of this chapter.

### 4.2 Current detection subscale experiment

#### 4.2.1 Goals of the experiment

The detection time of a traditional voltage detection method includes the time for a detectable voltage rise on the quench resistance and the additional time for validation purposes. Our goal is to shorten the total time before current decay. In the case of a CCT-type magnet, the longitudinal heat propagation is much faster than the transverse one due to the former structure. Nevertheless, instead of waiting for a significant longitudinal normal zone spread to reach the detectable voltage threshold and/or the passage of the evaluation time, the idea of testing a co-wound Nb<sub>3</sub>Sn superconducting wire was raised.

The principal is to place a thin superconducting wire beneath the cable. If the main cable quenches, the heat will transmit transversely from the cable to the superconducting wire through the in-between insulation layers. When the superconducting wire reaches its critical temperature, it also quenches. If the electrical circuit of the superconducting wire is powered with a constant voltage source, a change of the current and the current derivative can be observed in the circuit at the moment when the superconducting wire becomes a normal-conducting wire. Instead of a conventional voltage measurement on the rising resistance of

the superconducting wire, a current derivative sensor is used since we expect to have less noise and a cleaner signal with this method, which shall help to reduce or even eliminate the validation time.

The superconducting material of the sensing wire is selected based on the operating conditions. Typically, the sensing wire should have the same critical field and critical temperature with respect to the magnet cables. Therefore in a Nb<sub>3</sub>Sn CCT-type magnet, the idea of a current-based detection method could be implemented by running a thin Nb<sub>3</sub>Sn sensing wire along the cable inside the glass-braid insulation to meet the requirement.

The general goal of this study is to test the feasibility and measure the detection time of this current-based method using a co-wound superconducting wire, to compare experimental results with the prediction from simulations, and compare with the predictions made for a voltage-based method. An improvement in detection speed is expected for the current-based detection method.

### 4.2.2 Nb<sub>3</sub>Sn wire characterization

A bare bronze-route Nb<sub>3</sub>Sn wire of diameter 0.5 mm from a company called Supercon, was used as the sensing wire for this study [95]. A barrel of Nb<sub>3</sub>Sn wire was prepared for the characterization test, which was done by the University of Geneva. Prior to that, the Nb<sub>3</sub>Sn wires went through a thermal cycle of 5 days at 680 °C for reaction in the furnace. The critical current profile as a function of the magnetic field was measured for a length of 849 mm on the barrel, shown in Figure 4.1.

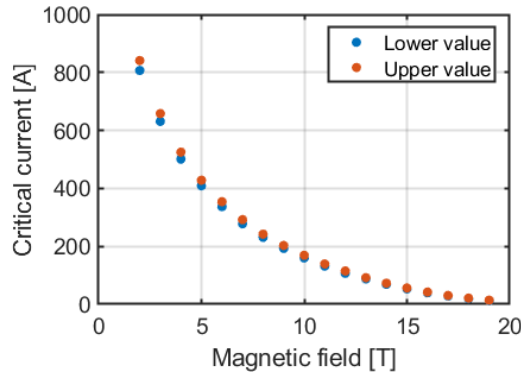


Figure 4.1 – Critical current profile as a function of magnetic field of the Nb<sub>3</sub>Sn sensing wire.

We are also interested in the critical temperature at zero field  $T_{c0}$  of this Nb<sub>3</sub>Sn wire. Furthermore, a  $T_{c0}$  experiment at PSI allows commissioning the cryogenic infrastructure and validating the test setup, as a step prior to the current detection test. The Gifford-McMahon cryocooler, in which the cooling agent moves back and forth inside a cylinder to perform adiabatic expansion of the refrigerant gas to generate a chill, from Sumitomo Heavy Industries is used to cool down the sample [96]. The two-stage cryogenic section secures a long-term

reliability in the 4 K temperature range.

The experiment proceeds as follows. When the Nb<sub>3</sub>Sn wire is cooled down to 4 K, the power supply of cryocooler is turned off so that the temperature inside the cryostat slowly increases due to the thermal conduction. As the superconducting wire is powered with a constant current, the voltage on the extremities of the Nb<sub>3</sub>Sn wire can be measured. When there is a quench, a voltage rise should be observed. Figure 4.2 shows the electrical circuit. The temperature drift speed is approximately 1 K per minute at cryogenic temperatures. It takes thus about 21 minutes for a temperature rise from 4 K to 25 K. The sample was clamped between two copper plates, called sample holder. A rectangular copper plate with holes was designed to connect the sample holder and the second stage of the cryocooler with screws. This plate covered the whole surface of the second stage ensuring a good contact for the cooling effect. One layer of 0.04 mm Kapton tape was placed on each inner side of the sample holder to isolate the sample from the copper sample holder.

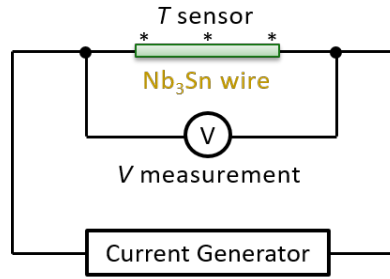


Figure 4.2 – Electrical circuit of  $T_{c0}$  experiment of Nb<sub>3</sub>Sn sample.

The Lake Shore Cernox thin film resistance cryogenic temperature sensors were selected for the temperature monitoring [97]. They can be easily mounted thanks to the small package size. In addition, they have been proven very stable over repeated thermal cycling. In total, four Cernox thermometers were attached and fixed on the outside of the sample holder, with two on each side, in order to record the temperature drift. The two different types of sensors used (SD and CU) are shown in Figure 4.3.

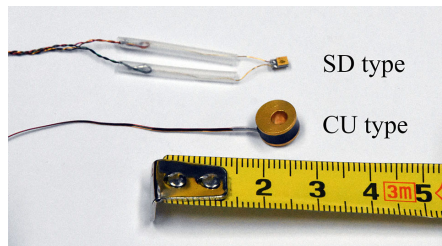


Figure 4.3 – Cernox cryogenic temperature sensors.

The SD type sensor has a smaller package size and a faster thermal response than the CU type. While the CU type sensor has a bigger package size, which is easy for mounting and gives a good lead thermal anchoring. Some indium foil and glue were used to ensure a good contact

between the sensors and copper sample holder. With a sampling frequency of 1 Hz, the limit of the Lake Shore temperature monitor used in the experiment, 60 data points were recorded in a minute, giving a resolution in the temperature reading of 0.0167 K.

The plate of the sample holder is 1 cm thick and the sensors are placed on the side that faces away from the sample. Moreover, between the sample and the sample holder, there is a layer of Kapton. With all these intermediate materials, the temperature measured by the Cernox thermometers is not exactly the value on the superconducting wire. Therefore a temperature offset determination and adjustment is necessary. By using the same setup and same principle, the  $T_{c0}$  of a Nb-Ti wire is measured, together with a Nb<sub>3</sub>Sn wire. The reason is that the Nb-Ti wire has a well-known critical temperature of 9.2 K at zero field [99]. The temperature difference between 9.2 K and the measured critical temperature value can be seen as a measurement offset for adjustment, that can be applied to a Nb<sub>3</sub>Sn wire.

To do that, a Nb-Ti wire was extracted from an LHC Rutherford cable, with the specification in [100]. This Nb-Ti wire was added in series with the Nb<sub>3</sub>Sn wire. Both of them were powered with a constant current. The voltage rise on both samples and temperature on the sample holder were recorded. Figure 4.4 shows the electrical circuit is presented. A piping and instrumentation diagram of the test is presented in Figure 4.5. The temperature range of interest is from 5 K to 15 K for Nb-Ti and from 10 K to 25 K for Nb<sub>3</sub>Sn.

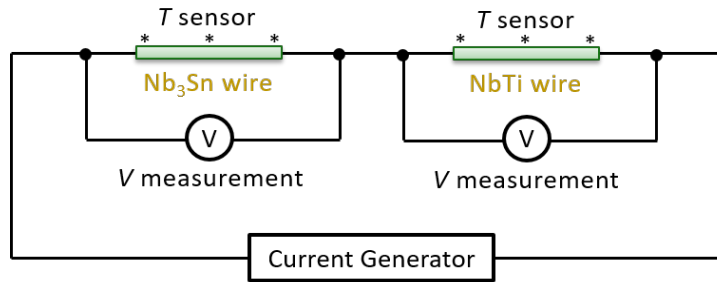


Figure 4.4 – Electrical circuit of  $T_{c0}$  experiment of Nb<sub>3</sub>Sn and Nb-Ti samples.

The reacted Nb<sub>3</sub>Sn wire is very brittle. It cannot stand alone without any solid support. The Nb<sub>3</sub>Sn wire was hence soldered with some tin along with an uninsulated copper wire of 1 mm in diameter. As mentioned above, a layer of Kapton tape on the inner sides of the sample holder can insulate the Nb-Ti wire and Nb<sub>3</sub>Sn wire from the copper sample holder. The Nb-Ti and Nb<sub>3</sub>Sn samples had different final diameters, they were fixed inside the sample holder by clamping them with screws.

The choice of connecting wire for the samples is based on the ohmic dissipation and heat transfer power to the cold end [98]. The heat leak from room temperature to the cold end of the connection wire must be minimized. Otherwise, the samples cannot be cooled to the desired temperature. A small diameter lead results in large amounts of ohmic dissipation and therefore the wire tends to become hot and the temperature gradient at the cold end increases. For a given temperature gradient, a large diameter lead can cause a high rate of heat transfer

0 1 2 3 4 5 6 7 8 9 10 11 12 13 14 15 16 17 18 19 20 21 22 23 24 25 26 27 28 29 30 31 32 33 34 35 36 37 38 39 40 41 42 43 44 45 46 47 48 49 50 51 52 53 54 55 56 57 58 59 60 61 62 63 64 65 66 67 68 69 70 71 72 73 74 75 76 77 78 79 80 81 82 83 84 85 86 87 88 89 90 91 92 93 94 95 96 97 98 99

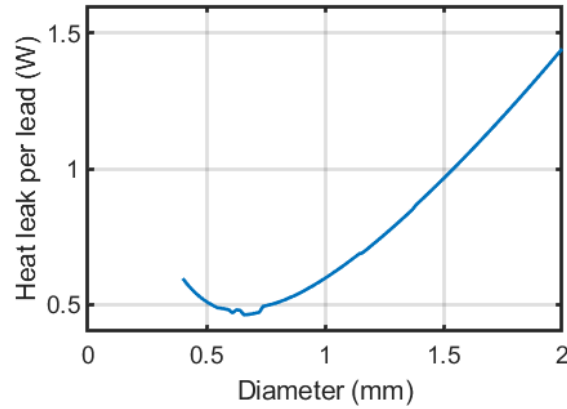


Figure 4.6 – Heat leak to the cold end of each current lead as a function of wire diameter, when the current is 6 A and wire length is 1.5 m long.

The experiment lasts for about 20 minutes. Note that there is a short part of the wire between the top shield and the flange which is always at room temperature, illustrated in Figure 4.5. The distance between the top shield and flange is approximately 10 cm. We consider that a slight higher current than its ampacity should not damage the wires due to the overload. The connection wires are twisted and wrapped around the first and second stage of the cryocooler. Outside the cryostat, wide-diameter insulated cables guide all the signals to different devices.

The Nb-Ti and final Nb<sub>3</sub>Sn sample are respectively shown in Figure 4.7a and 4.7b. The inner side of the copper sample holder with the Kapton tape is shown in Figure 4.8a. The samples were first fixed on one side of the sample holder with some thermal grease, presented in Figure 4.8b. Then we clamped the two sides of the sample holder together. Figure 4.9 shows the setup of the  $T_{c0}$  experiment of those two superconducting wires from different views. The  $T_{c0}$  experiment results of both Nb-Ti and Nb<sub>3</sub>Sn wire are plotted in Figure 4.10 when the samples are powered with a constant current of 6.2 A.



(a) Nb-Ti sample. Note that the connection wires in the figure are not the final ones used in the test.



(b) Final Nb<sub>3</sub>Sn sample, soldered with a copper wire of 1 mm diameter.

Figure 4.7 – Nb-Ti and Nb<sub>3</sub>Sn samples for  $T_{c0}$  experiment.

Note that the CU-type thermometer was placed on the top of the sample holder while the

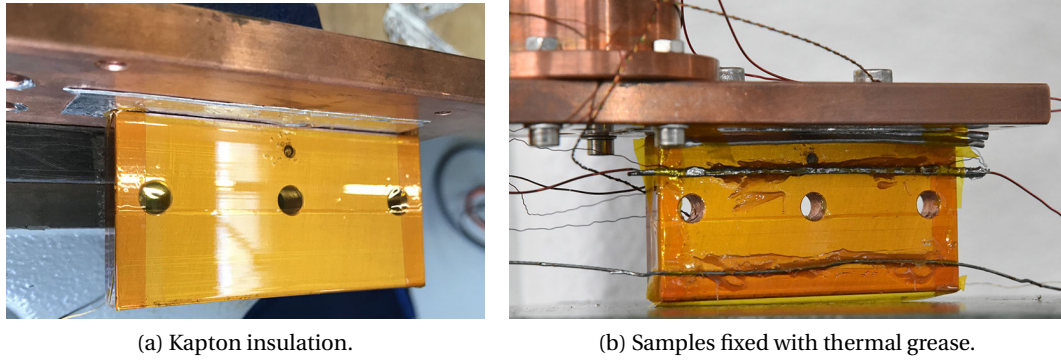


Figure 4.8 – Sample holder insulation for  $T_{c0}$  experiment.

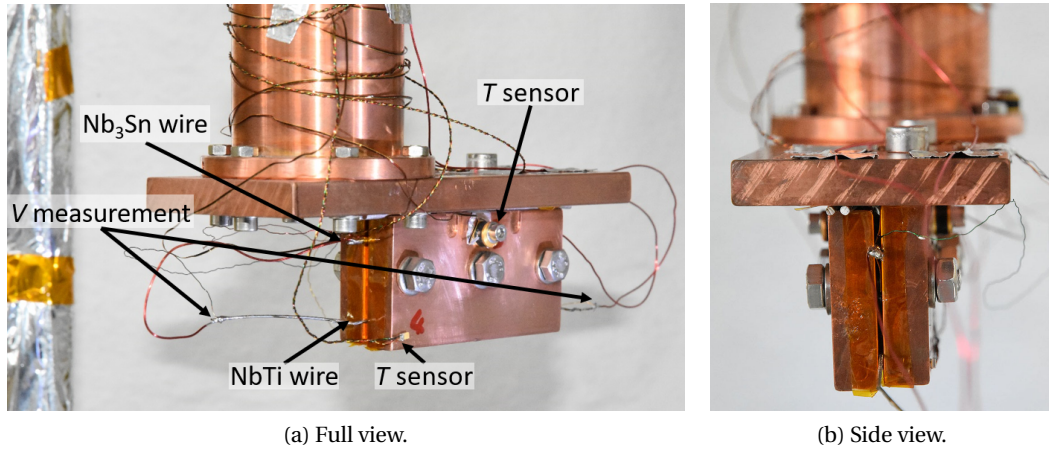


Figure 4.9 – Experimental setup of  $T_{c0}$  experiment of superconducting wires.

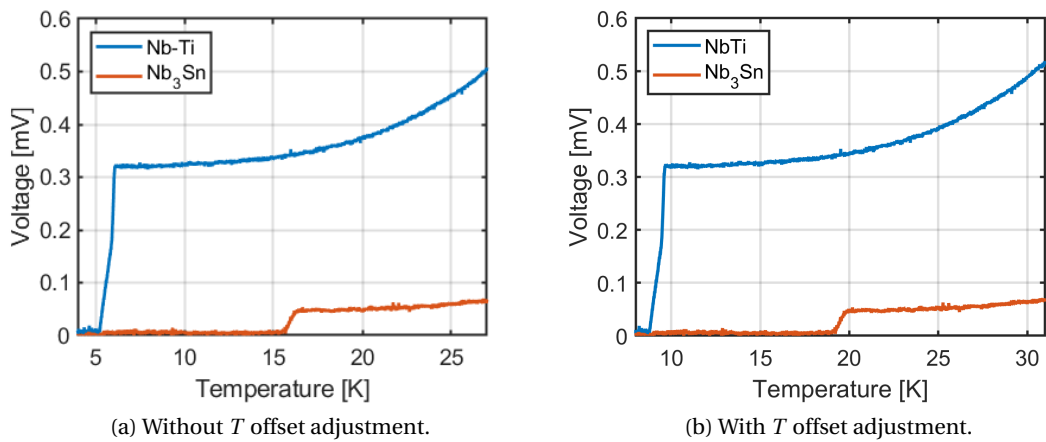


Figure 4.10 –  $T_{c0}$  experiment results of Nb<sub>3</sub>Sn and Nb-Ti wires, when the current is 6.2 A.

## Chapter 4. Quench Detection

SD-type thermometer was placed on the bottom of the sample holder. The same configuration was applied on the other side of the sample holder. An average temperature value of the readings of the four temperature thermometers is used for plotting.

The mid temperature point of the quench transition is used for correcting the measurement offset since the temperature difference may be not uniform across the sample. After an offset adjustment of 3.5 K, from the Nb-Ti measurement, we find that the Nb<sub>3</sub>Sn sample starts to quench around 19.1 K. This value is larger than the expected one, which is 18 K [101]. The possible reason could be a different temperature difference between the averaged  $T$  and the Nb-Ti wire, and between the averaged  $T$  and the Nb<sub>3</sub>Sn wire. In this experiment, only the order of magnitude of the critical temperature of the Nb<sub>3</sub>Sn wire was verified. The Cernox sensors must be placed as close as possible to the samples, allowing a precise temperature measurement, which was not the case described here.

Table 4.1 lists the parameters of the two sample wires with the calculated and measured voltage. A value of  $2 \times 10^{-10} \Omega \cdot \text{m}$  is used for copper resistivity at 20 K. The resistivity of tin is taken from [102], which is  $9 \times 10^{-10} \Omega \cdot \text{m}$  at 20 K. Note that the final cross-section diameter of the Nb<sub>3</sub>Sn sample is not longitudinally homogeneous and varies between 2.5 and 3.0 mm. The resistance of the whole sample is a parallel resistance of three parts: the copper part in the Nb<sub>3</sub>Sn wire, the soldered copper support wire and tin. For both sample wires, the measured and calculated voltage are reasonably close. In this  $T_{c0}$  experiment, we confirm that the test setup, as well as the cooling system work well.

Table 4.1 – Sample wire parameters with calculated and measured voltage for  $T_{c0}$  experiment when a current of 6.2 A is applied.

| Nb-Ti sample                               |                      |
|--|----------------------|
| Cu fraction                                | 0.667                |
| Wire diameter                              | 8.25e-4 m            |
| Wire length                                | 0.12 m               |
| Calculated voltage                         | 4.18e-4 V            |
| Measured voltage                           | 3.21e-4 V            |
| Measured/Calculated voltage $\times 100\%$ | 76.84 %              |
| Nb <sub>3</sub> Sn sample                  |                      |
| Cu fraction                                | 0.2                  |
| Nb <sub>3</sub> Sn wire diameter           | 5e-4 m               |
| Wire length                                | 0.08 m               |
| Soldered Cu wire diameter                  | 1e-3 m               |
| Calculated voltage                         | [5.84e-5; 4.56e-5] V |
| Measured voltage                           | 4.3e-5 V             |
| Measured/Calculated voltage $\times 100\%$ | [73.57; 94.38] %     |



### 4.2.3 Principle of current detection test setup

In the current detection test, we aim to simulate a quench scenario in a co-wound loop composed of a thin superconducting wire, which is placed beneath the quenching cable. The principle relies on a transverse heat propagation from the cable to the co-wound superconducting sensing wire. To test this idea in a subscale model, a thin stainless-steel heater strip is used to mimick a quenching cable and a Nb<sub>3</sub>Sn wire is placed beneath the heater strip with several in-between layers of insulation. This design allows the transverse heat propagation from the heater to the superconducting wire, as in a real superconducting cable.

A simple electrical schema is illustrated in Figure 4.11. There are two circuits in this test setup. One is the heater strip circuit and the other one is the superconducting sensing wire circuit. The green block represents the sample, which was placed in the cryostat and tested at a cryogenic temperature of about 4 K. The remaining parts were in ambient temperature. A piping and instrumentation diagram of the test is presented in Figure 4.12. The test setup is shown in Figure 4.13. The same thermometer position was applied in this test as mentioned in the  $T_{c0}$  experiment: CU-type on the top and SD-type on the bottom of the sample holder.

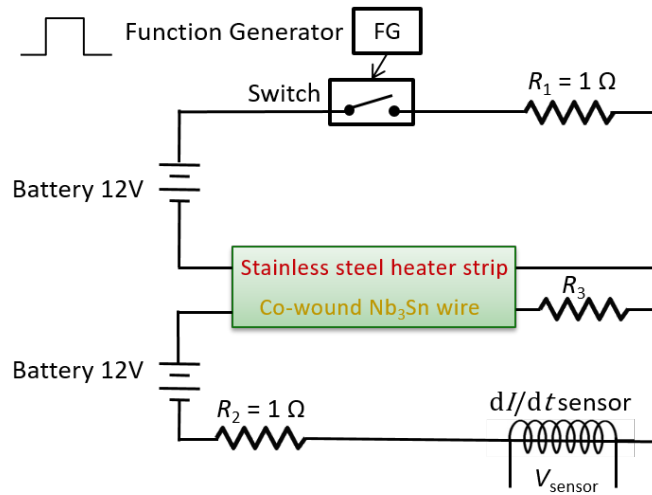


Figure 4.11 – Electrical circuit of current detection test.

Both circuits are powered with a constant voltage. In order to reduce the noise level on the output signal, batteries replace power supplies in both circuits. The circuit of the heater strip is commanded by a solid-state switch, an electronic switching device that switches on or off when a small external voltage is applied across its control terminals. The solid-state relay has fast switching speeds compared with an electromechanical relay. The specifications of the solid-state relay used are described in Table 4.2 [103]. When the control voltage is above 3 V, the load circuit is closed and when the control voltage is below 1 V, the load circuit is open. In the experiment, we deliver a rectangular heat pulse. A function generator is connected between the control terminals of the solid-state switch to control the heater strip load circuit. By using a function generator, one can customize the heat pulse by adjusting the amplitude,

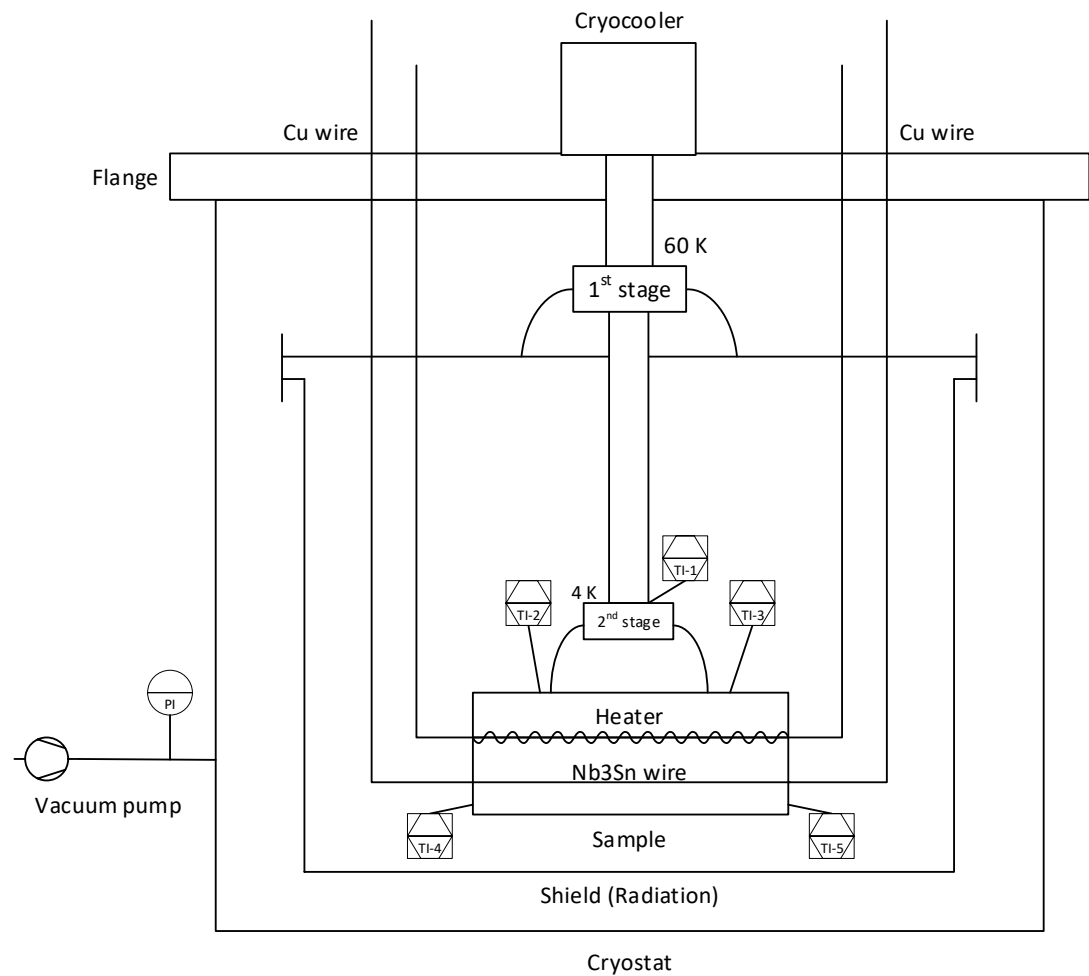
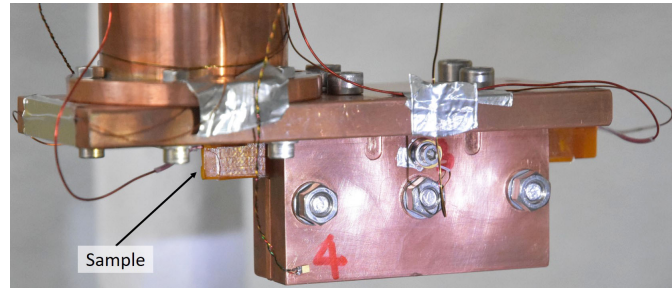


Figure 4.12 – Piping and instrumentation diagram of current detection test with current leads (not-to-scale).

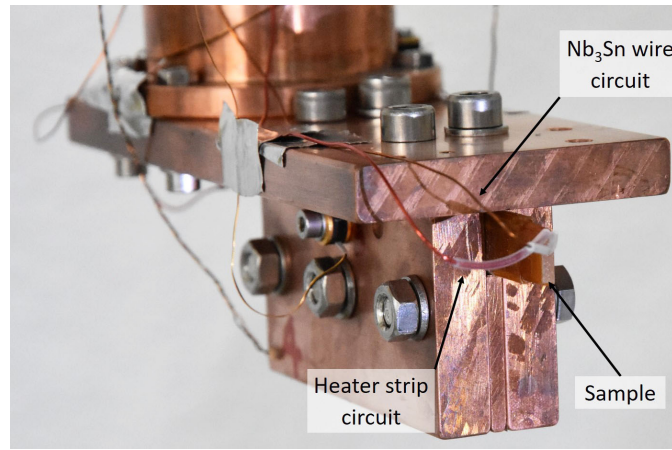
offset, pulse width, and frequency of a rectangular pulse signal.

Table 4.2 – Solid state relay specifications.

| Input Specifications    |              |
|-------------------------|--------------|
| Control Voltage Range   | 3 - 10 VDC   |
| Max Turn-On Voltage     | 3 VDC        |
| Min Turn-Off Voltage    | 1 VDC        |
| Max Turn-On Time        | 1 msec       |
| Max Turn-Off Time       | 0.3 msec     |
| Nominal Input Impedance | 300 $\Omega$ |
| Output Specifications   |              |
| Operating Voltage       | 0 - 100 VDC  |



(a) Full view.



(b) Side view.

Figure 4.13 – Experimental setup of current detection.

In Figure 4.11,  $R_1$  and  $R_2$  are two value-known resistors. By measuring the voltage on each resistor, the current in the respective circuit is monitored.  $R_3$  is used to regulate the current level in the circuit of superconducting wire since the battery has a fixed voltage level. Besides,  $R_3$  can be any other reasonable value to have several amperes in the superconducting circuit. In this test, the value of  $R_3$  is either  $3.3 \, \Omega$  or  $1 \, \Omega$ . The wire of the superconducting circuit constitutes the primary of the current derivative sensor and the response is obtained on the secondary of the sensor. The current drop in the primary and the voltage peak on the secondary are both measured in the experiment.

The cable sample design is based on an initial design of CD1 superconducting cable. A G10 block is used as the main support of a cable. A stainless-steel heater strip is made to trigger a quench. The ensemble of both constitutes a quenching cable. The sample cross-section design is shown in Figure 4.14. In this figure,  $x$  is the thickness of all the insulation layers between stainless steel heater strip and  $\text{Nb}_3\text{Sn}$  wire, and  $y$  is the resin thickness between the mica sheet and  $\text{Nb}_3\text{Sn}$  wire. These two parameters are not precisely known before cutting the sample since the resin thickness is not well controlled during the impregnation process.  $x$  and  $y$  are crucial in the experiment since they impact on the transverse propagation time, and thus the detection time. The dimension of the sample is described in Table 4.3.

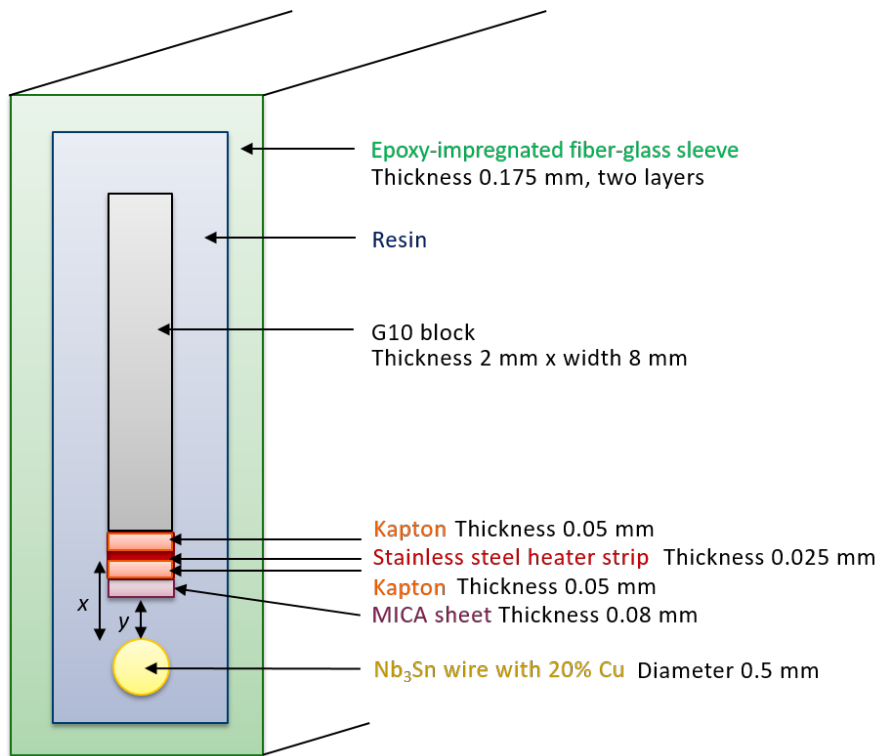


Figure 4.14 – Sample cross-section design for current detection test (not-to-scale).

Table 4.3 – Sample main parameters for current detection test.

| G10 block dimension             |                    |
|---------------------------------|--------------------|
| Block width                     | 8 mm               |
| Block thickness                 | 2 mm               |
| Block length                    | 12 cm              |
| Insulation thickness            |                    |
| Mica layer                      | 0.08 mm            |
| Fiber braiding                  | 0.175 mm           |
| Heater strip                    |                    |
| Heater strip thickness          | 2 mm               |
| Heater strip length             | 100 mm             |
| Stainless steel strip thickness | 0.025 mm           |
| Kapton thickness                | 0.05 mm            |
| Co-wound superconducting wire   |                    |
| Strand type                     | Nb <sub>3</sub> Sn |
| Strand diameter                 | 0.5 mm             |
| Cu percent                      | 20 %               |

Figure 4.15 shows a sample overview. The sample overall length is 12 cm. The effective length for the test is 8 cm. The 2 cm on both sides are reserved for soldering and fixing purposes. The choice of copper connection wire in the detection circuit mainly depends on the heat leak to the cold end. A wire of small diameter has a low heat leak. In this test, the same considerations are taken into account as in the critical temperature experiment for the connection wire of the heater strip, to use an insulated wire of 0.6 mm. Concerning the connections wire of the superconducting sensing wire, an insulated copper wire of 0.5 mm is used. The explanation for the selection choice is given in Subsection 4.2.4.

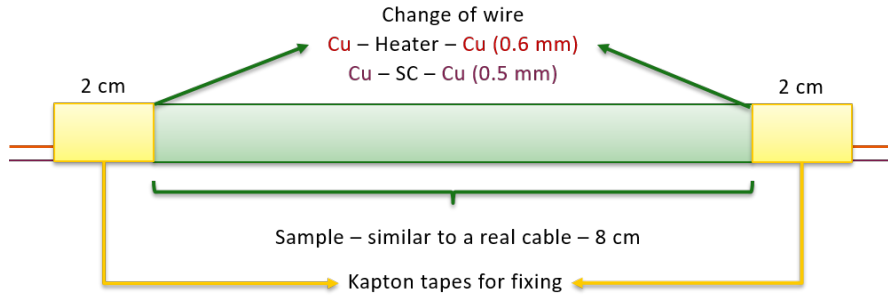


Figure 4.15 – Sample overview with connection wires for current detection test (not-to-scale).

When the heater strip delivers a pulse, the  $\text{Nb}_3\text{Sn}$  superconducting wire heats up. Once it quenches, the resistance  $R_{\text{quench}}(t)$  increases with temperature. A constant resistance  $R_{\text{wire}}$  is considered for the copper connection wires. The current profile in the detection circuit is thus written as  $I = U / (R_{\text{quench}}(t) + R_0)$ , with  $R_0 = R_2 + R_3 + R_{\text{wire}}$ .

The wires are twisted to avoid large loops to reduce the inductance in the circuit. Note that since the current flowing in the  $\text{Nb}_3\text{Sn}$  wire is very small, the contribution of Joule heating of the wire during the quench is negligible. The current flowing inside the superconducting wire could also induce a magnetic field. The strength of this field depends on the level of the current. When the field is strong enough, it may speed up the quench process. However, in this case, the current in the  $\text{Nb}_3\text{Sn}$  wire is very small thus the induced field is weak (in the order of 0.1 T, calculated in Subsection 4.2.5). The critical temperature of the wire roughly equals to  $T_{c0}$ .

The process of heating up the sample from the initial temperature 4 K to the critical temperature is slow, compared to the case in a high-field magnet, since the temperature margin is big. In a high-field magnet, the temperature change from the operating point to the current-sharing temperature is only several kelvins (about 2-3 K) for a superconducting cable, resulting in a significantly shorter quench detection time using the current-based detection method. For example, in the case of CD1 at a current level of 15.5 kA, a quench occurs when the temperature rises from 4.2 K to 7.2 K in the high-field zone of the inner-layer coil, as described in Subsection 2.4.3. For a small current flowing in the  $\text{Nb}_3\text{Sn}$  wire ( $< 5$  A), the critical temperature is almost at zero field, which is equivalent to 18 K. In this experiment, with 4 K initial sample temperature, the temperature increase needed to initiate a quench is about 14 K. The recorded

experimental detection time is therefore longer. Nevertheless, a similar temperature margin can be reproduced by increasing the sample initial temperature to about 15 K, to conduct the experiment.

### 4.2.4 Sample manufacturing

The sample preparation starts by building a heater. The heater is composed of a stainless-steel strip which is covered by a layer of Kapton tape on each side for electrical insulation purposes. The extremities of the stainless-steel strip are soldered to the copper connection wires ( $\approx 1.5$  m long). The length of the heater strip is 10 cm. We reserve 1 cm for soldering on each side. Therefore the effective length of the sample is 8 cm. With the heater dimension outlined in Table 4.3, the calculated heater resistance is  $1.1 \Omega$  at  $20^\circ\text{C}$ , using the value of  $6.9\text{e-}7 \Omega \cdot \text{m}$  for the stainless-steel resistivity. The measured manufactured heater resistance is  $1.3 \Omega$ . When the connecting wires are soldered, the total resistance with wires is  $1.7 \Omega$  at room temperature. Once the heater strip is prepared, it is fixed on a G10 support on the extremities. A mica strip is then added above the heater strip to simulate the insulation between the superconducting cable and the sensing wire.

A reacted  $\text{Nb}_3\text{Sn}$  wire soldered with the copper connection wires ( $\approx 1.5$  m long) is fixed on the mica strip. Theoretically, if a thick connection wire is used (low resistance in the circuit), a large step is expected in the current due to the quench, which can be picked up by the current derivative sensor. However, the heat leak of the thick wire to the cold end also increases, which is not desired in the experiment. If a thin wire is used (high resistance in the circuit), a small step in the current may not be able to be picked up by the sensor.

In fact, the resistance of the connection wire has at least one order of magnitude smaller than other resistors ( $R_2$  and  $R_3$ , both in the order of magnitude of ohm) in the sensing loop, as shown in Figure 4.11. The diameter of the connection wire has little contribution to the current step that we want to measure. The dominant factor is the heat leak of the wire to the cold end, as presented in Figure 4.6 for a current of 6 A. Since a smaller current (than 6 A) is running in the  $\text{Nb}_3\text{Sn}$  wire, the minimum heat leak level is also reduced. For a current level of 5 A, the minimum heat leak is obtained when the wire diameter is about 0.5 mm. Theoretically this wire can carry 2.1 A in the ambient environment. The wire dimension should be big enough to carry the desired current level. Because each experiment only lasts for a few seconds, we assume that it is safe to use a copper connection wire of 0.5 mm in diameter for the  $\text{Nb}_3\text{Sn}$  wire at cryogenic temperatures.

Finally, a fiberglass band is wrapped on the whole sample to push all the components as close as possible to make a tight sample since the distance between the heater and the  $\text{Nb}_3\text{Sn}$  sensing wire is crucial for a fast current-based detection. Note that some grooves were made on the extremities of the G10 support, which provide space for the wire soldering. Some photos of the sample manufacturing process are shown in Figure 4.16 for the current detection test.

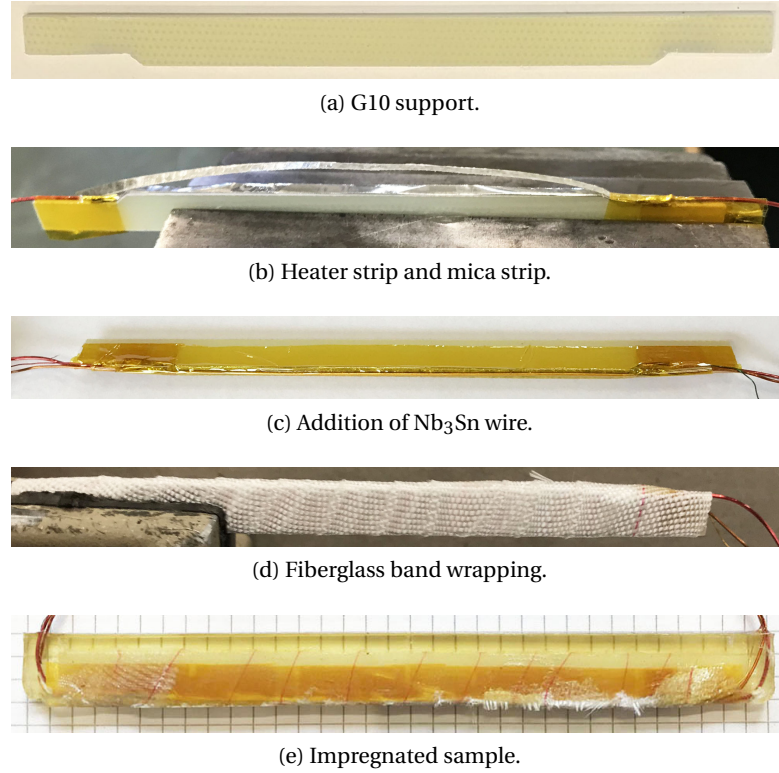


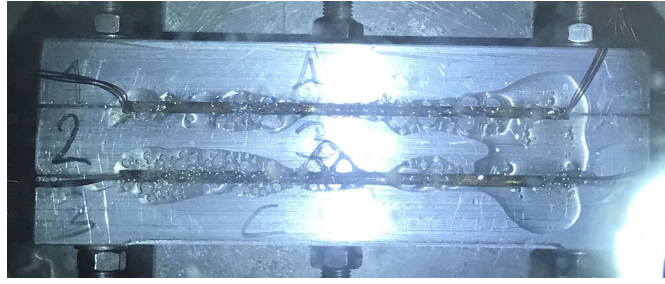
Figure 4.16 – Sample construction process for current detection test.

The sample needs to go through the impregnation process to simulate the real superconducting cable. The epoxy resin FSU mix-61 [104], the same one used in the CD1 model magnet, was applied in the sample. After a degassing of 15 minutes of the resin mixture in a vacuum, we dripped the mixture on the samples, that were placed in an open mold in the ambient environment. We put then the samples as well as the mold in the vacuum again to degas for another 30 minutes in order to let the mixture flow through the entire sample. If the mixture goes to the bottom of the mold, there is not enough mixture on the top any more. Additional resin needs to be added and degassed to complete the procedure.

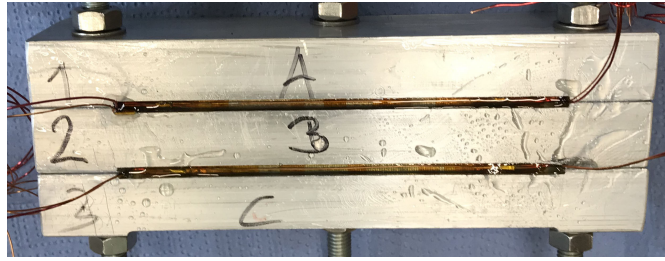
Once the samples are covered by the resin mixture, the mold is placed into the furnace for polymerization. The curing cycle is 16 hours at 60 °C and the post curing is 24 hours at 120 °C. When everything cools down, we can unmold the samples and machine the surfaces to be smooth. In this impregnation way, almost no bubbles are observed in the samples. Figure 4.17 shows the sample impregnation process for the test.

### 4.2.5 Current derivative sensor

In order to measure the voltage peak at the moment of the quench, a dedicated current derivative sensor is constructed, according to the study discussed in [105]. Figure 4.18 illustrates the sensor design, where  $I_1$  is the primary current,  $n_1$  the number of turns in the primary loop,  $I_2$



(a) In vacuum for degassing.



(b) In ambient environment.

Figure 4.17 – Sample with mold during impregnation process for current detection test.

the secondary current,  $n_2$  the number of turns in the secondary loop,  $l_c$  the coil length,  $l_a$  the air gap,  $\Phi$  the magnetic flux in the coil, and  $U(t)$  the voltage in the secondary loop.

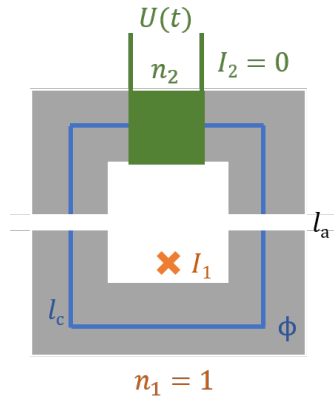


Figure 4.18 – Current derivative sensor design (following [105]).

Ampere's law gives

$$\oint H \cdot dl = NI \quad (4.1)$$

where  $H$  is the magnetic-field strength,  $l$  the mean path length of a solenoid or the circumference of a toroid,  $N$  the number of turns in the coil, and  $I$  the electric current through the circuit.



## 4.2. Current detection subscale experiment

The magnetic Kirchhoff law tells  $F = \Phi R$ , where  $\Phi$  is the magnetic flux and  $R$  the magnetic reluctance of the circuit. For a uniform flux and magnetic field inside a rectangular or toroidal element, the magnetomotive force (MMF) between the ends of element is  $F = Hl$  with  $H = B/\mu$  and  $B = \Phi/A_c$ , where  $B$  is the magnetic field,  $\mu$  the material permeability, and  $A_c$  the core area. The MMF can be thus written as  $F = \Phi \cdot l/(\mu A_c)$  with the reluctance of element  $R = l/(\mu A_c)$ .

The sensor model has two core parts and two air gaps, the whole equation is given by

$$F_a + F_c + F_a = \Phi(R_c + 2R_a) = I_1 \quad (4.2)$$

with the core reluctance  $R_c = l_c/(\mu_c A_c)$  and the air gap reluctance  $R_a = l_a/(\mu_0 A_c)$ , where  $\mu_c = \mu_0 \mu_r$ . By injecting the reluctance equations into Eq. (4.2), the magnetic flux is written as

$$\Phi = \frac{I_1}{R_c + 2R_a} = \frac{I_1}{\frac{l_c}{\mu_c A_c} + \frac{2l_a}{\mu_0 A_c}} = \frac{\mu_0 A_c I_1}{\frac{l_c}{\mu_r} + 2l_a} \quad (4.3)$$

According to Faraday's law, the voltage in the secondary is  $U(t) = n_2 \cdot d\Phi/dt$ . Note that not only the current depends on time, but also the reluctance  $R_c$  depends on current and therefore on time. The final sensor response is thus given by

$$U(t) = n_2 \mu_0 A_c \frac{\left( \frac{l_c}{\mu_r} + 2l_a \right) \frac{\partial I_1}{\partial t} - l_c I_1 \frac{\partial}{\partial t} \left( \frac{1}{\mu_r} \right)}{\left( \frac{l_c}{\mu_r} + 2l_a \right)^2} \quad (4.4)$$

There is another simple way to calculate the sensor response. As we know  $\Phi = B \cdot A_c$ , and the flux lines are perpendicular to the core cross section and the cross section is constant in our case, therefore any change in magnetic field results in a change in flux  $\Delta\Phi = \Delta B A_c$ . So the sensor response becomes:

$$U(t) = n_2 \frac{d\Phi}{dt} = n_2 A_c \frac{dB}{dt} \quad (4.5)$$

For a given current in the primary loop, we can derive the following relationship from Eq. (4.1):

$$I = \oint \frac{B}{\mu} dl = \frac{2Bl_a}{\mu_0} + \frac{Bl_c}{\mu_c} \quad (4.6)$$

Therefore the  $B$  field can be written as

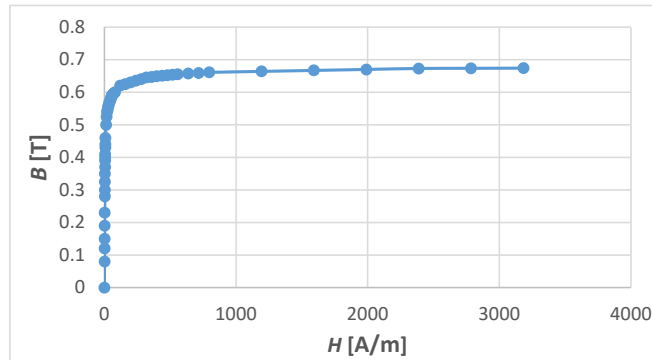
$$B = \frac{I}{\frac{2l_a}{\mu_0} + \frac{l_c}{\mu_c}} \quad (4.7)$$

and the  $H$  field in the core is  $H_c = \frac{B}{\mu_c}$ . By repeating several iterations in the calculation, we can

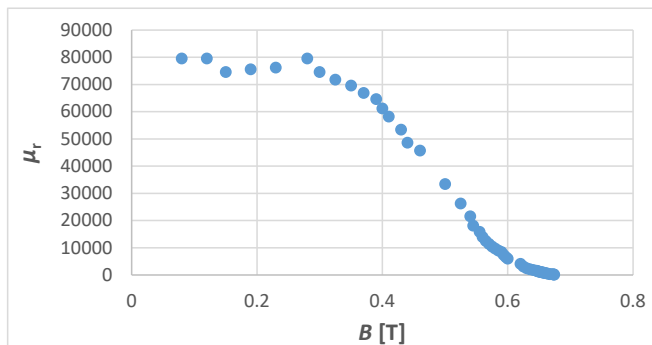
obtain the correct  $B$  field and core permeability by looking up if the values match with the  $B$ - $H$  curve of such a material. From that, we can calculate the sensor response with Eq. (4.5).

Our goal is to have a measurable voltage peak for a given  $\partial I / \partial t$  at a given current level. The factors that have an impact on the sensor performance are the number of turns in the primary and secondary, the air gap thickness, the core area, and the core permeability. A core with high permeability at low field, a small air gap, a big number of turns in the primary and secondary, and a big core area gives a high sensitivity. Note that we must make sure that the core does not saturate with the number of turns placed in the primary and secondary.

To meet the requirement, mumetal is selected as a suitable material for the test. It is a nickel-iron soft ferromagnetic alloy with high permeability, often used for shielding sensitive electronic equipment against static or low-frequency magnetic fields. Annealing the mumetal objects helps increase the magnetic permeability. The annealing process alters the material's crystal structure, to align the grains and remove some impurities. An annealed toroidal mumetal core was purchased from Magnetic Shield [106] to construct a dedicated current derivative sensor in-house. The core is made of a mumetal strip of 0.2 mm thickness. This kind of lamination suppresses eddy currents. The typical  $B$ - $H$  curve and the relative permeability with  $B$  field are shown in Figure 4.19.



(a)  $B$ - $H$  curve.



(b) Relative permeability with  $B$  field.

Figure 4.19 – Properties of mumetal (Data from [106]).

## 4.2. Current detection subscale experiment

The core geometry is illustrated in Figure 4.20, with OD (outer diameter) = 80 mm, ID (inner diameter) = 40 mm, H (height) = 20 mm. To make a current derivative sensor, the toroidal core needs to be cut into two parts. As the core is formed by a long and thin strip. If we cut, it will fall apart. Hence before cutting, the core was impregnated with FSU mix-61 in order to keep it in the initial form and to preserve its packing factor. The impregnation procedure was the same as the one described for the sample.

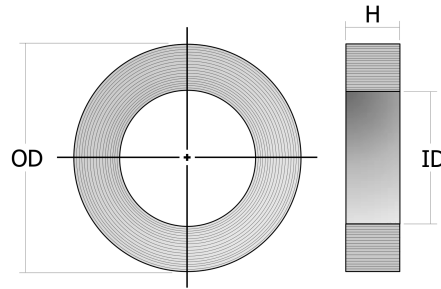


Figure 4.20 – Current derivative sensor core shape for current detection test.

In fact, any mechanical shock after annealing of the mumetal objects could disrupt the grain alignment of the material, leading to a decrease in the permeability of the affected areas. In order to reduce any possible permeability damage during the construction process, the impregnated core was cut with wire electrical discharge machining technique. The material was removed by a series of rapidly recurring current discharges between two electrodes, separated by a dielectric liquid and subject to an electric voltage.

Once we have two separate parts, on one part, 3000 turns of a copper wire of 0.3 mm diameter, were wound onto the core with a plastic support in order to avoid any short circuit with the round core. If the copper winding wire is too small, it is difficult to handle during the winding process and may lose some performance. If a big wire is used, in a given space, the number of turns is reduced, affecting the detection sensitivity. Thus there is a compromise between the dimension of winding wire and the performance of the sensor. A copper winding wire of 0.3 mm in diameter was chosen.

The cut surfaces of the core were polished into the smooth surfaces so that the air gap is small when the two parts of the core were clamped. By wrapping some layers of Kapton tapes on the outer side of the whole sensor, the two parts were assembled together. Some pressure was needed to enhance the contact between the parts. Note that the mumetal core saturates at low magnetic fields, which is approximately 0.67 T. Therefore the number of turns in the primary is chosen to be 1 in order not to saturate the material. In addition, the relative permeability is very low when the core is saturated, as shown in Figure 4.19b. The main parameters of the current derivative sensor are listed in Table 4.4. Some pictures of the fabrication process of the current derivative sensor are presented in Figure 4.21, and the final sensor is displayed in Figure 4.22.

In fact, a change in current (and also in  $B$ ) in the case without an air gap causes a very small

Table 4.4 – Main parameters of the constructed current derivative sensor.

| $A_c$ [m <sup>2</sup> ] | $l_c$ [m] | $l_a$ [m] | $n_1$ | $n_2$ |
|-------------------------|-----------|-----------|-------|-------|
| 4e-4                    | 0.1885    | 7.5e-6    | 1     | 3000  |

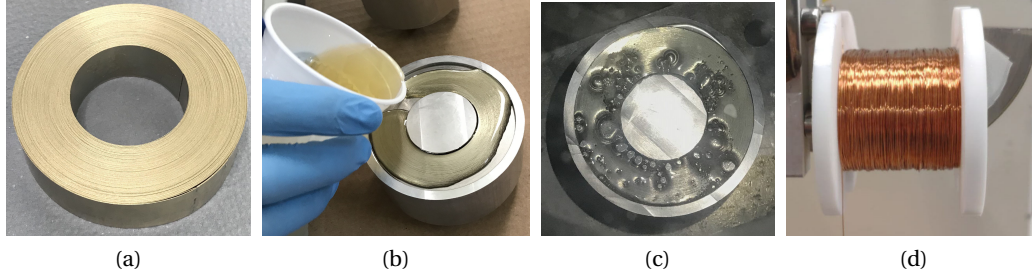


Figure 4.21 – Current derivative sensor fabrication process. (a) Initial toroidal mumetal core; (b) Pour epoxy resin on mumetal core for impregnation; (c) Degas in vacuum; (d) Put windings on half core.



Figure 4.22 – Final current derivative sensor in an iron shield box.

change (almost zero) in flux because the operating point situates in the flat part of the mumetal  $B$ - $H$  curve. We thus need to set the air gap to a value that puts the operating point into the steep part of the  $B$ - $H$  curve in order to obtain a high detectable voltage amplitude. Moreover, the signal size in  $\Delta H$  is small enough to ensure linear conditions around the operating point.

There is an optimum air gap thickness when the voltage reaches its maximum value. A rate of current change of at least 1 A/s is expected in the primary circuit during the process of heating up the sample to its critical temperature. Assuming that a 2 A current flows in the primary circuit, the calculated voltage on the current derivative sensor versus different air gap thicknesses is plotted in Figure 4.23 when a current drop of 1 mA in 1 ms has to be detected.

In this figure, a maximum voltage value is observed when a total air gap thickness is 5  $\mu\text{m}$ , which is difficult to achieve in reality. In our setup, an equivalent air gap thickness of  $2l_a = 15 \mu\text{m}$ , is used for calculation of the sensor response. This value is estimated based on a test of

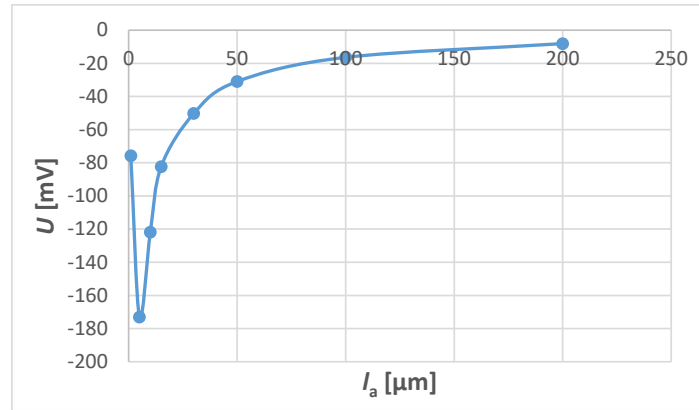


Figure 4.23 – Calculated voltage on the current derivative sensor versus different air gap thicknesses, assuming a 2 A current flows in the primary circuit, with a current drop of 1 mA in 1 ms to be detected.

the sensor performance with a triangle waveform in the primary.

When we have a current of 2 A in the primary circuit, by doing an iterative calculation of Eq. (4.6), a  $B$ -field value of 0.15 T is obtained. The mumetal relative permeability at this level is approximately 75000. With the core parameters listed in Table 4.4, the mutual inductance of the current derivative sensor is estimated as 46.4 mH.

### 4.2.6 Data acquisition system (DAQ)

The batteries are used in the experiment to reduce the noise. Furthermore, all the components and circuits are shielded in order to have a small noise-to-signal ratio. The current derivative sensor, the heater strip circuit, as well as the superconducting wire circuit are placed into three different boxes made of iron to eliminate any possible fluctuations from the environment, and to reduce the cross-talk between the circuits.

In the experiment illustrated in Figure 4.11, three signals are recorded. The first one is the current in the heater strip circuit. The second one is the current in the superconducting circuit, and the last one is the voltage on the current derivative sensor.

The output signal is recorded with a National Instruments PCI-6036E NI DAQ card 16-bit with a maximum sampling rate of 200 kS/s (multiplexing) [107]. The minimum range provided is  $\pm 50$  mV and the minimum voltage step is  $100 \text{ mV} / 2^{16} = 1.53 \mu\text{V}$ . An appropriate range needs to be selected for data acquisition in order to achieve the best signal resolution for each signal. Moreover, a sampling rate of 60 kS/s is used for each channel to get signals with high precision.

As each signal has its own properties, different signal connection schemes are applied in order to produce the best signal for each one. In general, all the signals are measured using the differential signal connection to reduce noise pickup and avoid ground loops.

To get a value for the differential measurement, two analog inputs (AI) are used and paired. The hardware measures the difference between the AI+ and AI- signals, and output this measurement. Caution needs to be taken in the differential mode since the instrumentation amplifier input bias currents could move the voltage level of the source out of the valid range of the input stage of a data acquisition device. To anchor this voltage level to a reference, bias resistors are used for each analog input. Consequently, two resistors of equal value are used for each channel in order to maintain a balanced system. These resistors provide a DC path from the instrumentation amplifier inputs to the instrumentation amplifier ground. According to the recommendation of National Instruments [107],  $R = 100\text{ k}\Omega$  is used since the value of these bias resistors should be large enough to allow the source to float with respect to the measurement reference (AI GND) and not load the signal source, but small enough to keep the voltage in the range of the input stage of the device.

The complete connection schemes for three signals are described in the following paragraphs.

### Current in the heater strip circuit

The connection scheme for the current signal in the heater circuit, measured on  $R_1$ , is illustrated in Figure 4.24. The current in the heater strip circuit is obtained by measuring the voltage on a  $1\text{ }\Omega$  resistance. A range of  $\pm 5\text{ V}$  is selected for data acquisition. We only apply the differential connection for this channel as the signal amplitude is big (several volts) resulting in a small noise-to-signal ratio.

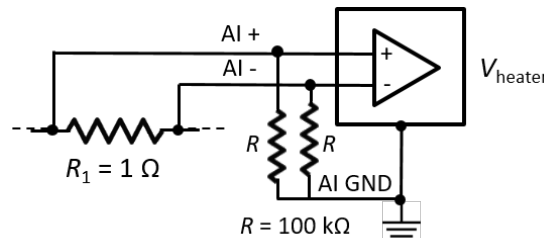


Figure 4.24 – Connection scheme for the current signal in the heater circuit, measured on  $R_1$ .

### Voltage on the current derivative sensor

The connection scheme for the voltage signal on the secondary of the current derivative sensor is illustrated in Figure 4.25. As the voltage on the sensor is sensitive to the current change in the primary, the signal is always centered around zero except when there is a change of current in the circuit.

In reality, the data acquisition system also introduces some noise to the measured signal. This noise is minimized by selecting the smallest range available on the acquisition card to have the lowest noise produced internally from the system. The minimum range of  $\pm 50\text{ mV}$  is therefore chosen. In addition to the differential connection, a capacitor ( $10\text{ }\mu\text{F}$ ) is added on

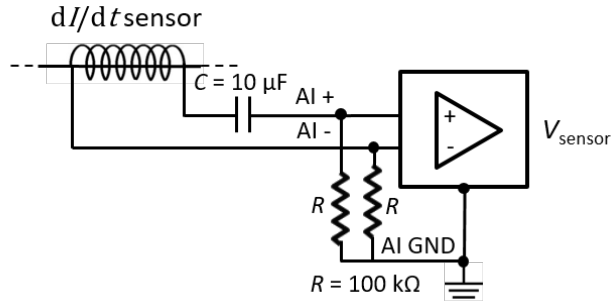


Figure 4.25 – Connection scheme for the voltage signal on the secondary of the current derivative sensor.

AI+ input to build a high-pass filter with the bias resistor (100 kΩ), giving a time constant of 1 s. The high-pass filter only passes signals above the selected cut-off frequency, eliminating any low-frequency signals from the waveform. The cut-off frequency is  $f_c = 1/(2\pi RC) = 0.16$  Hz.

### Current in the superconducting circuit

The connection scheme for the current signal in the superconducting circuit, measured on  $R_2$ , is illustrated in Figure 4.26. The current in the superconducting circuit is obtained by measuring the voltage on a 1 Ω resistance. For a current of 2 A flowing in the circuit, a current drop of approximately 0.2 mA is expected (explanation in Subsection 4.2.7). In order to have a clean signal with a noise level as small as possible, the minimum range of  $\pm 50$  mV is used. In this approach, a voltage compensation measurement method is involved. The principle is described as follows. if a voltage of 2 V is measured, then an equal-value and opposite-direction voltage is applied in parallel with the acquisition channel, canceling the initial signal level before the data acquisition. Therefore only the signal change, i.e., a current drop when there is a quench, is recorded.

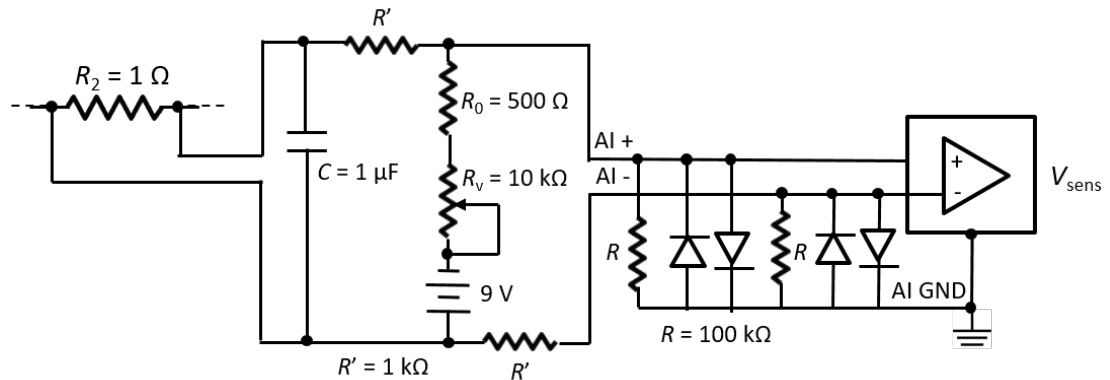


Figure 4.26 – Connection scheme for the current signal in the superconducting circuit, measured on  $R_2$ .

To realize that, a 9 V battery, a fixed resistor and a variable resistor are added in series between the AI+ and AI- inputs. We can regulate the signal level around zero by tuning the variable resistor before firing the heater strip. Since a voltage source (9 V battery) is involved in the data acquisition system, additional electrical components are added to avoid a high current flowing into the data acquisition system. First, resistors  $R'$  are connected in the branches of the AI+ and AI- inputs. Second, some diodes are connected in parallel with the bias resistors to protect the analog inputs. When the voltage over the diodes is below 0.6 V, there is no current passing through them.

In addition, a capacitor  $C$  (1  $\mu\text{F}$ ) is added in parallel with the AI+ and AI- inputs to build a low-pass filter with the resistor  $R_2$  (1  $\Omega$ ), giving a time constant of 1  $\mu\text{s}$ . A low-pass filter passes signals with a frequency lower than a selected cut-off frequency and attenuates signals with frequencies higher than the cut-off frequency. The cut-off frequency is  $f_c = 1/(2\pi R_2 C) = 159.2$  kHz.

### 4.2.7 Results and analysis

Since the samples were made manually, they show different characteristics. For the first samples, the distance between the heater and superconducting wire was very large thus more energy was needed, than expected, to trigger a quench in the sensing wire. The fabrication process of samples was improved in order to keep the distances  $x$  and  $y$  as small as possible. In this subsection, the results of two samples with different test configurations are presented. The variable parameters are the length and the amplitude of the rectangular heat pulse, the current level in the superconducting circuit, as well as the initial temperature of the test setup. Eventually, the impregnated samples are cut to measure the distance between the heater strip and the  $\text{Nb}_3\text{Sn}$  wire for a detailed investigation.

#### Test results of Sample 1

##### Proof of concept with a fixed heat pulse and current in the sensing wire

For a given heat pulse illustrated in Figure 4.27, the test results of Sample 1 are shown in Figure 4.28. The heat pulse has an amplitude of 5.2 A and it lasts for 20 ms. Its power density is 439 W/m. The energy delivered is calculated as  $\Delta E = I^2 R \Delta t$ . An energy of 0.7 J is released where the heater strip's resistance is 1.3  $\Omega$ , measured at cold with the current leads. In the superconducting wire circuit,  $R_3 = 3.3$   $\Omega$  is used. As a consequence, there is a current of approximately 2.5 A flowing in the circuit, with the existence of a measured 0.4  $\Omega$  resistance of the connection wire.

Figure 4.28a shows the current in the superconducting wire circuit. A current drop is observed around 3.9 s and after about 1.3 s the current goes back to its initial level. The current drop is due to the quench of the  $\text{Nb}_3\text{Sn}$  wire. The normal state lasts for a certain time when the



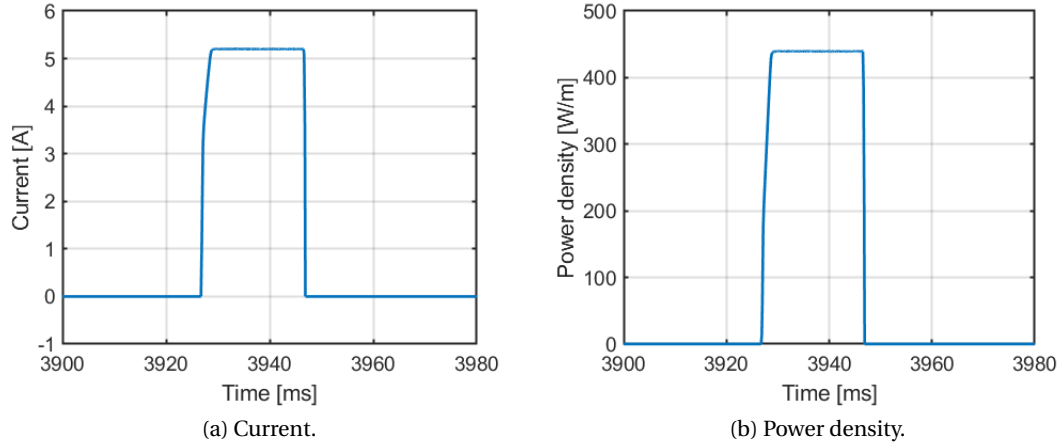


Figure 4.27 – Heat pulse delivered in the heater strip over time. Its amplitude is 5.2 A and length is 20 ms.

residual power is larger than the cooling power of the cryocooler. When the cooling power exceeds the heating, the sensing wire starts to get cold again slowly since the cryocooler is working all the time. The wire recovers to the superconductive state.

Figure 4.28b shows the voltage signal on the current derivative sensor. Note that the heat pulse induces some inductive disturbances on the signal  $I_{\text{sens}}$  and  $V_{\text{sensor}}$ , which is the disadvantage of using a heater with a rectangular heat pulse to mimic the quenching cable. In a real quench-detection setup, the current in the quenching cable would initially stay constant and this perturbation would not be present.

With a zoom around the moment of quench, and a superposition of the plots of  $I_{\text{sens}}$  and  $V_{\text{sensor}}$ , we obtain Figure 4.28c. In the time interval [3925; 3930] ms, there are some residual effects linked to the heater discharge. This feature is also present in room-temperature measurements and therefore does not constitute a quench, but an inductive effect linked to the heater firing. In the time interval [3935; 3940] ms, we observe the quench of the sample, on both signals. The current  $I_{\text{sens}}$  decreases twice with a brief plateau in between the slopes. Therefore we have two peaks on the current derivative sensor, shown in Figure 4.28d. This can be explained by the inhomogeneous distance between the heater strip and the sensing wire. A certain length of the superconducting wire is close to the heater strip while the remaining part is not as close to the heater strip. A second transverse quench propagation occurs in the wire following a first transverse one from the heater strip to the wire.

It is worth noting that a slight slope is observed when measuring the current in both circuits of the heater strip and the superconducting wire due to the battery's loss in the output voltage over time. For this reason, the data of the measured currents in Figure 4.28 was corrected for the linear slope.

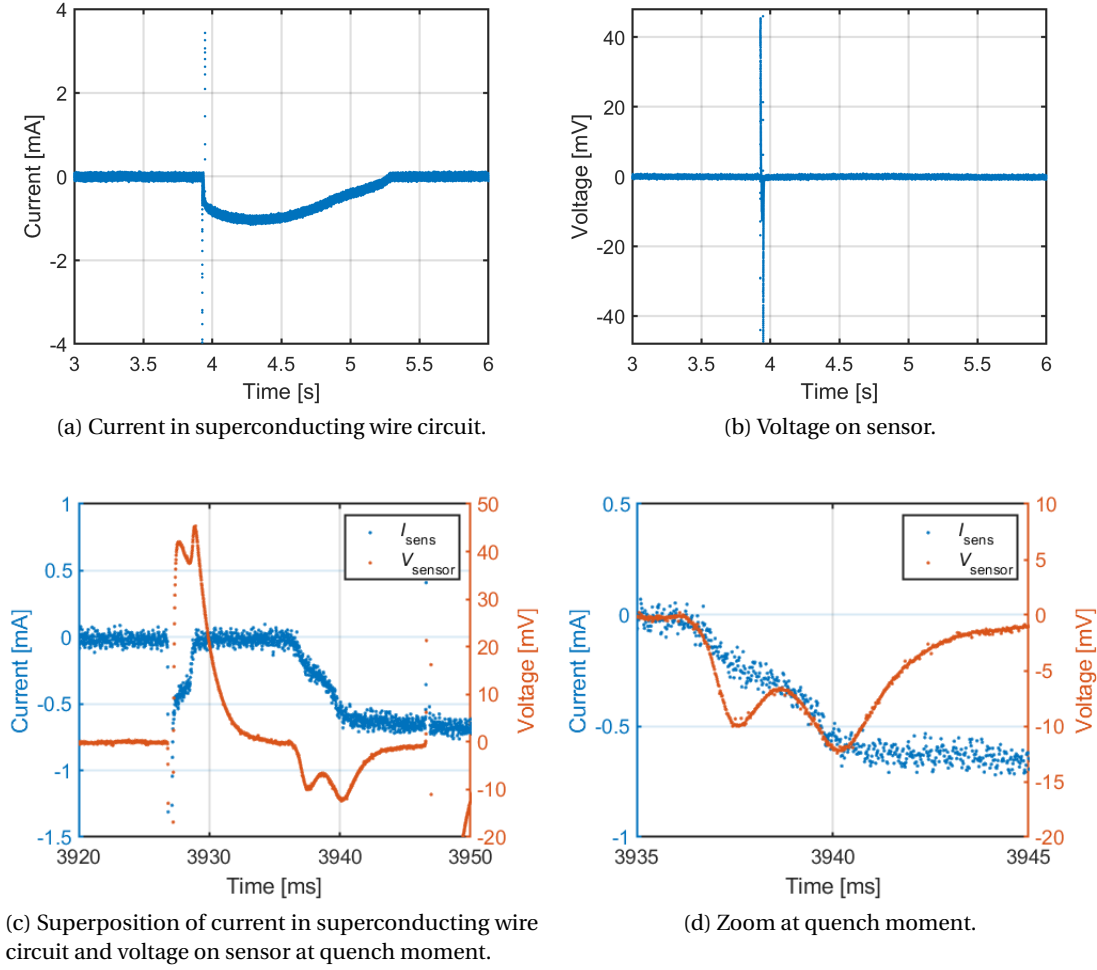


Figure 4.28 – Current detection results on Sample 1 with  $R_3 = 3.3 \, \Omega$ , when a heat pulse of 5.2 A is applied for 20 ms .

The quench delay time between the initiation of the heater and the first peak is approximately 10.7 ms for a temperature rise from 4 K to 18 K. The current drop of  $I_{\text{sens}}$  is 0.62 mA when  $I_{\text{sens}} = 2.5$  A. Theoretically, if considering the resistance of the sensing wire in the sample is  $0.4 \, \text{m}\Omega$  at 20 K, a current drop of 0.21 mA is expected. The simulation assumes one step-like transition at 18 K, whereas the transition in the experiment lasted for several milliseconds. The average sample temperature at the end of the transition was, therefore higher than 18 K. In addition, the measured resistance drop could also include some lead resistance change.

The current change rates in the superconducting wire are  $[0.21; 0.26] \, \text{A/s}$  for the first and second part of the current drop. The measured  $V_{\text{sensor}}$  peaks are  $[10; 12.4] \, \text{mV}$ . This is consistent with the mutual inductance of the sensor as indicated in Subsection 4.2.5. With the present setup, only the peaks at the moment of quench can be detected. The drift part of the quench recovery is invisible on the current derivative sensor.

### Comparison of simulation and test results of Sample 1

In a 2D adiabatic sample cross-section simulation without any cooling effect, the temperature profile on the heater strip and Nb<sub>3</sub>Sn sensing wire are simulated, when a heat pulse with a form shown in Figure 4.27, is initiated at  $t = 0$ . The goal is to mimick a quenching cable, that heats up to 85 K in 20 ms with a background field of around 10 T. The resistance growth and the current profile in the sensing wire as a function of time are calculated in order to have an estimation of current variation. The predefined values  $x = 150 \mu\text{m}$  and  $y = 20 \mu\text{m}$  are used in the simulation. Actually these parameters impact the quench delay time, however, we only study in this paragraph the temperature in the heater strip, as well as the signal forms. Thus the values of  $x$  and  $y$  are not crucial here. The simulation results are plotted in Figure 4.29.

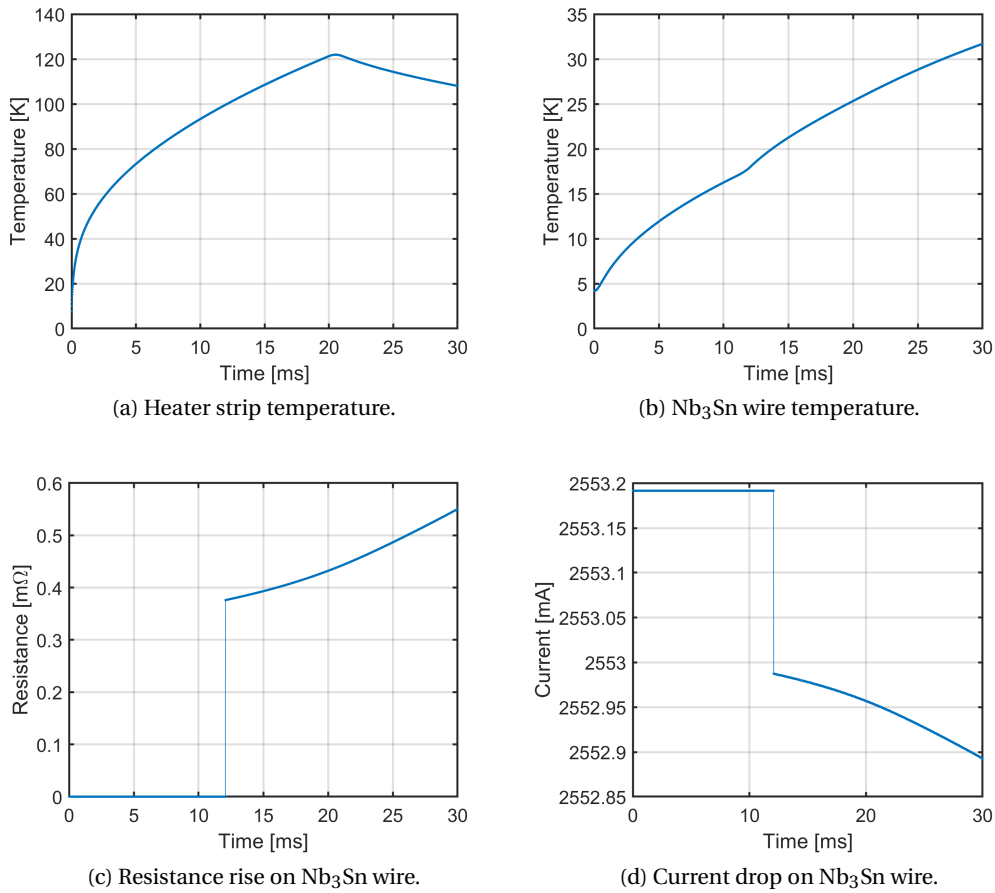


Figure 4.29 – Simulation results for current detection, when a heat pulse of 5.2 A is applied for 20 ms.

We remark that the temperature rise in the heater strip is approximately 116 K in 20 ms, a higher value than the one in a quenching cable with a background field of around 10 T, but it is still a quite good approximation to mimick a quench cable by using a heater strip. In

fact, an instantaneous quench occurs on the superconducting wire cut section, illustrated in Figure 4.29, which means a big  $\partial I / \partial t$  and a big voltage peak on the sensor. However, in the measurement, a slow quench slope is observed and this low quench speed results in smaller peaks (only about 10 mV) on the sensor than expected (about 50 mV).

### Impact of the change in the pulse amplitude and length

We are interested in changing the heat pulse amplitude and duration to see the effects on the detection in the experiment. For a constant amplitude, we vary its duration. When a heat pulse has a power density of 439 W/m (same amplitude of 5.2 A as before) and it lasts for 5 ms, the quench happens after the delivery of the pulse, as shown in Figure 4.30a. If the heat pulse amplitude or the duration is further reduced, then no more quench can be observed any more. Figure 4.30b illustrates this effect when a heat pulse has an amplitude of 3.6 A for 5 ms. From these tests, an experimental minimum quench energy can be derived for Sample 1, which is about 0.18 J.

For a constant heat pulse amplitude, the energy density of different durations versus the measured delay time is plotted in Figure 4.31. When the heat pulse duration of 20 ms is applied, the quench transition happens before the end of the pulse, as displayed in Figure 4.28c. When the heat pulse lasts for 15 ms, part of the transition happens before the end of the pulse. These two cases both have the same delay time of 10.7 ms. As long as the quench happens within the heat pulse duration, the delay time is always the same, confirmed by the simulation. When the heat pulse duration becomes shorter (e.g., 10 and 5 ms), the quench transition happens after the end of the pulse, the detection delay time becomes longer, until no more quench can be observed, i.e., an infinite delay time. In short, we can only observe the delay time difference once the quench happens after the heater pulse when its duration is short.

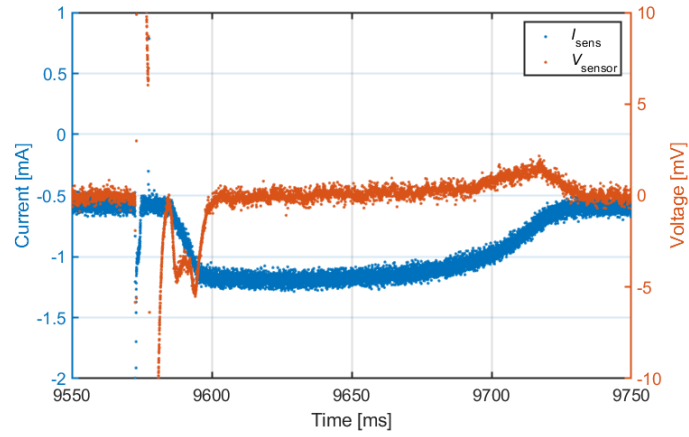
The impact of pulse length on temperature of heater strip and sensing wire is studied only in the simulation as the temperature monitoring is not precise in these fast transients with the present experiment setup. Under the same condition, the simulation is launched for a pulse time of 20 ms and 30 ms. By increasing the pulse time, the temperature rise on the Nb<sub>3</sub>Sn wire is smaller than the one on the heater strip, which is not efficient from the point of view of the experiment design. Thus a short pulse is more beneficial.

To summarize, with a shorter pulse length and a higher heater power, the detection delay time is shorter and the heating process is faster. With a longer pulse length and a lower heater power, the detection delay time is longer and the heating process is slower.

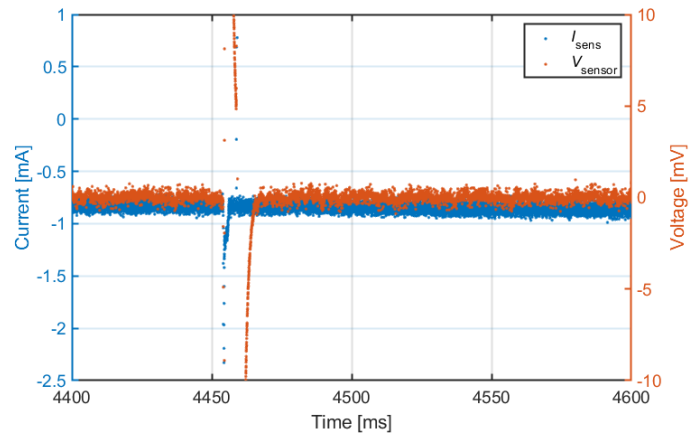
### Measurement of the distance between the heater strip and the sensing wire

As mentioned before, the distances  $x$  and  $y$ , illustrated in Figure 4.14, are not precisely known

## 4.2. Current detection subscale experiment



(a) Quench happens after the end of the pulse when a heat pulse of 5.2 A for 5 ms applied.



(b) No quench observation when a heat pulse of 3.6 A is applied for 5 ms.

Figure 4.30 – Current detection test results on Sample 1 with  $R_3 = 3.3 \Omega$ , when varying the length and amplitude of the applied heat pulse to determine minimum quench energy.

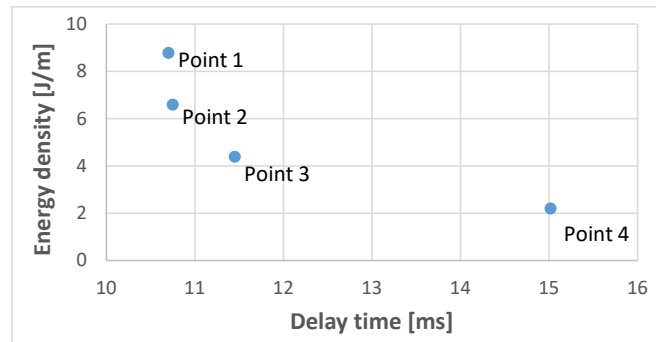


Figure 4.31 – Energy density versus measured quench delay time. The Point 1 to 4 correspond respectively a heat pulse duration of 20, 15, 10 and 5 ms.

before cutting the samples, due to the impregnation process. These distances impact on the time to quench. Once the minimum quench energy is found experimentally, one can use this value and the delay time  $t_{\text{delay}}$  between the initiation of the heater pulse and quench to estimate the distances that most closely fit the existing measurement data in the 2D cross-section simulation. For Sample 1,  $x = 150 \mu\text{m}$  and  $y = 20 \mu\text{m}$  are found and applied when fixing the delay time obtained from the measurement in the simulation.

In order to validate the assumptions on these values, the sample was cut into several pieces as shown in Figure 4.32. The cutting surfaces from A to D were polished for measuring the distances  $x$  and  $y$ . As the saw for cutting has a thickness of 1 mm, and the polishing process also took away some additional material, the cutting surfaces at the same location, e.g., B and C, are not mirrored as expected. Figure 4.33 presents the cutting surfaces of Sample 1 at different locations.

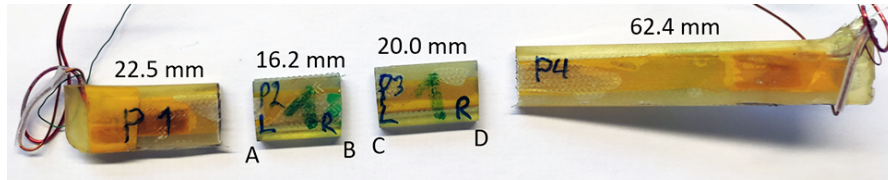


Figure 4.32 – Locations of cutting surfaces of Sample 1.

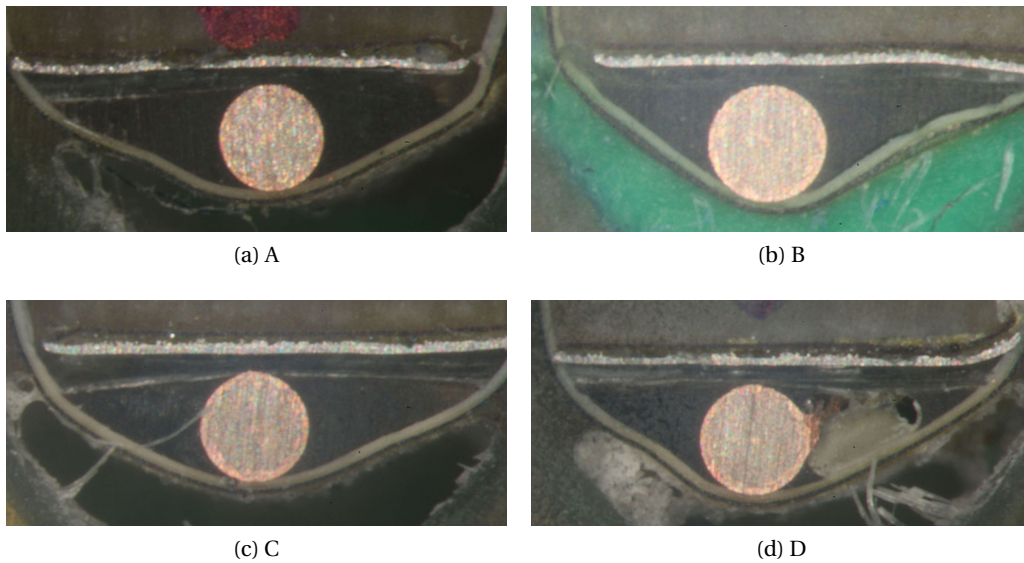


Figure 4.33 – Cutting surfaces of Sample 1 for determination of the distance between the heater strip and the edge of superconducting wire, as well as the transverse thickness of epoxy resin.

From top to bottom, the observed steel layer is the heater strip. The measurement of  $x$  is considered from the bottom level of the silver layer to the edge of the superconducting wire with a certain error margin. It is however difficult to distinguish the layers of Kapton, mica and epoxy resin from the pictures in between the heater strip and superconducting wire. Therefore

## 4.2. Current detection subscale experiment

the parameter  $y$  is only presented for the cutting surfaces where the material boundary can be clearly seen. Considering the superconducting wire of 0.5 mm in diameter as a reference, the measured distances  $x$  and  $y$  are tabulated in Table 4.5.

Table 4.5 – Measured distances between the heater strip and superconducting wire, and resin thickness on cutting surfaces of Sample 1.

| Distance              | A          | B          | C          | D          |
|-----------------------|------------|------------|------------|------------|
| $x$ [ $\mu\text{m}$ ] | $90 \pm 3$ | $88 \pm 5$ | $83 \pm 2$ | $87 \pm 2$ |
| $y$ [ $\mu\text{m}$ ] | /          | $27 \pm 3$ | /          | $21 \pm 2$ |

From these data, a small variation of distance  $x$  is noticed at different locations. Due to the limited number of cuts, larger variations along the sample cannot be excluded. Quench first happens in the superconducting wire when it is at the closest location to the heater strip. Despite the smallest value of  $x$  is found at surface C, the parameter  $y$  can not be measured at this position. Thus the set of values at the cutting surface D are used and compared to the simulation. Theoretically, one should get 130  $\mu\text{m}$  for the Kapton and mica strip. Therefore the value of  $x$  should be larger than 130  $\mu\text{m}$ . However, the measured value of  $x$  is smaller than expected which is due to the material compression. Nevertheless, we confirm, on the sample edge, the measured total thickness of the Kapton and mica strip is between 130  $\mu\text{m}$  and 140  $\mu\text{m}$ . The extra thickness can be explained by the filling of the epoxy resin. The measured value of  $y$  gets very close to the assumption.

The quench delay time is calculated in the simulation again using the measured distances  $x$  and  $y$  at the cutting surface D. The involved thickness of Kapton and mica layer are adjusted due to the material compression. The thicknesses for Kapton, mica and epoxy resin are respectively 25  $\mu\text{m}$ , 41  $\mu\text{m}$  and 21  $\mu\text{m}$ . In this case, the quench delay time is 7.7 ms in the simulation versus 10.7 ms in the experiment, when a pulse in Figure 4.27 is applied. The time difference can be explained by the inhomogeneous heat transfer along the sample and a cooling effect that is not taken into account in the model.

### Impact of the change in the current level in the superconducting sensing circuit

By increasing the current in the superconducting wire, we can increase the signal amplitude in both current drop and sensor voltage measurement. This time,  $R_3 = 1 \Omega$  is used, which means a current of 5 A in the sensing circuit. With the same heat pulse shape illustrated in Figure 4.27, the results are plotted in Figure 4.34.

The measured current drop of  $I_{\text{sens}}$  is 1.3 mA when  $I_{\text{sens}} = 5$  A. Theoretically, if considering the resistance of the sensing wire in the sample is 0.4 m $\Omega$  at 20 K, a current drop of 0.81 mA is expected. The experimental current drop caused by the quench is higher than the calculated value due to the same reason described in Subsection 4.2.7.

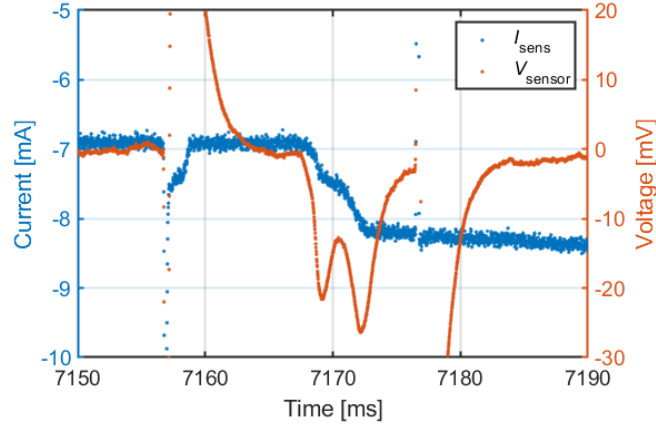


Figure 4.34 – Current detection results on Sample 1 with  $R_3 = 1 \Omega$ , when a heat pulse of 5.2 A is applied for 20 ms.

The current change rates in the superconducting wire circuit are [0.41; 0.43] A/s for the first and second peak on the current derivative sensor signal. The measured values are [21.6; 26.4] mV on  $V_{\text{sensor}}$ . The peak amplitude is doubled in this configuration. However, we cannot put too much current in the primary circuit because the permeability of mumetal decreases when the magnetic field increases. A different choice of material may allow for further optimization of signal strength.

### Impact of the change of the initial temperature in the setup

With a pulse duration of 20 ms, the quench delay time  $t_{\text{delay}}$  is measured for different temperature ranges. By turning off the cryocooler, we let the temperature drift to the desired initial temperature  $T_{\text{init}}$  and then we start the experiment. When  $T_{\text{init}}$  gets close to  $T_{c0}$ , the temperature margin becomes small for triggering a quench. In this way, temperature margins present in a high-field magnet in the high-field zone of the coil can be reproduced. And therefore a short  $t_{\text{delay}}$  is expected.

When the initial temperature ( $> 14$  K) approaches the critical temperature, the delay time can not be measured any more since the sensor peak is embedded in the disturbances. In order to extrapolate experimental results towards faster detection times, i.e., into a region where a clean measurement is not possible due to the inductive noise from the heater circuit. We select the length parameters of  $x$  and  $y$  that most closely fit the existing measurement data for initial temperatures smaller than 14 K. The quench delay time is thus calculated in the simulation using  $x = 150 \mu\text{m}$  and  $y = 20 \mu\text{m}$ . In this way, we can get the best approximation of delay time for  $T_{\text{init}} > 14$  K in the 2D simulation, taking into account the inhomogeneous transverse heat transfer along the sample. The quench delay times obtained from the experiment and simulation with different initial temperatures are presented in Figure 4.35.



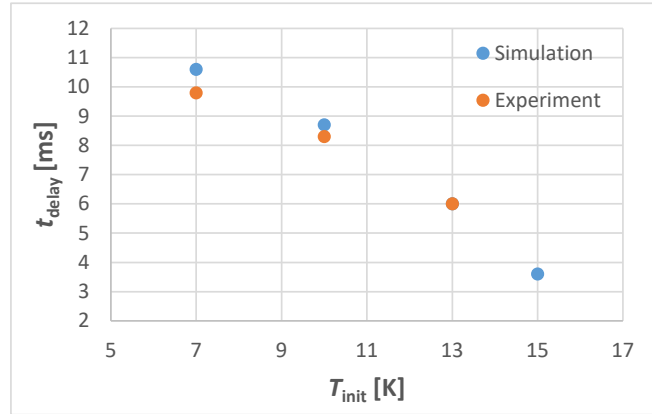


Figure 4.35 – Transverse quench delay time (from heater initiation to first peak on the sensor) obtained from the experiment and simulation with different  $T_{init}$  in the current detection test.

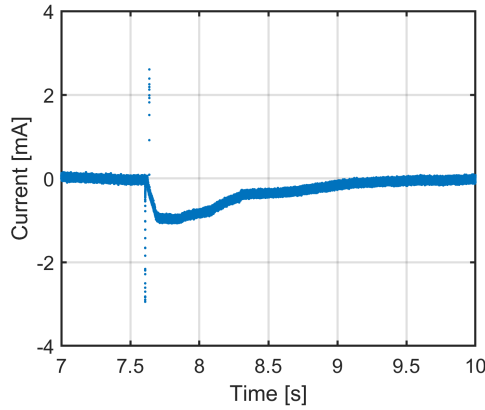
Note that the measured distances  $x$  and  $y$ , which are obtained and discussed in Subsection 4.2.7, are not used here because of the large time difference found due to the inhomogeneous transverse heat transfer.

### Test results of Sample 2

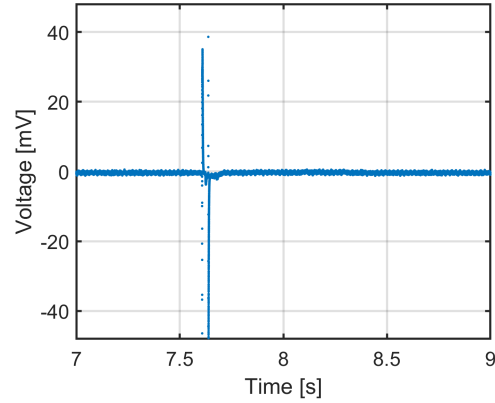
Figure 4.36 shows the results of Sample 2, with  $R_3 = 3.3 \, \Omega$ , when a heat pulse shape illustrated in Figure 4.27 with a duration of 30 ms is applied. For this sample, only one peak is observed on the sensor signal. The current drop is approximately 0.87 mA, resulting in a slope of 0.014 A/s. The current drops over a duration of 63.9 ms, indicating a rather long delay between the most- and the least-heated point along the sensing wire.

If we zoom in Figure 4.36c and look at Figure 4.36d, the current drop slope at the very beginning of the quench is about 0.06 A/s, which gives a theoretical peak value of 2.8 mV on the sensor. In the experiment, a value of 3.7 mV is measured. Compared to the results of Sample 1, we have a smaller peak amplitude of  $V_{sensor}$  and a much slower quench speed. There is still a clear signal on the sensor, despite the slow quench. From that, we can derive that the distance between the heater strip and sensing wire is not well-controlled in Sample 2, and considerably larger than the one in Sample 1.

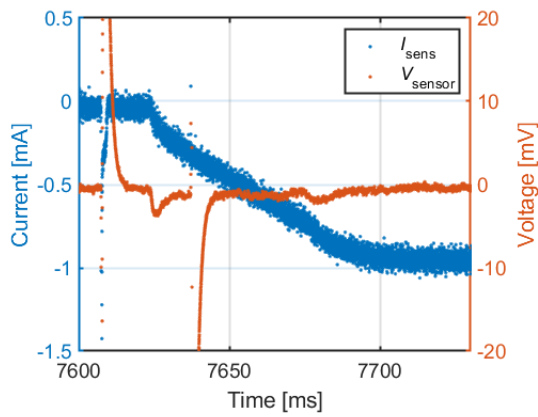
In order to validate the findings, the sample was cut into several pieces as shown in Figure 4.37. The polished cutting surfaces from A to F are displayed in Figure 4.38. The same considerations of measuring  $x$  and  $y$  described for Sample 1 are used for Sample 2. The measured distances are outlined in Table 4.6. From these data, an inhomogeneous distance  $x$  is noticed at different locations. The longitudinal variation of the distance is bigger than the one for Sample 1. Furthermore, a considerably big distance between the heater and the sensing wire is confirmed from the measured data. The material compression only occurs at some locations, e.g., B and D, since the distance  $x$  is smaller than the theoretical value 130  $\mu\text{m}$ . Besides, because this



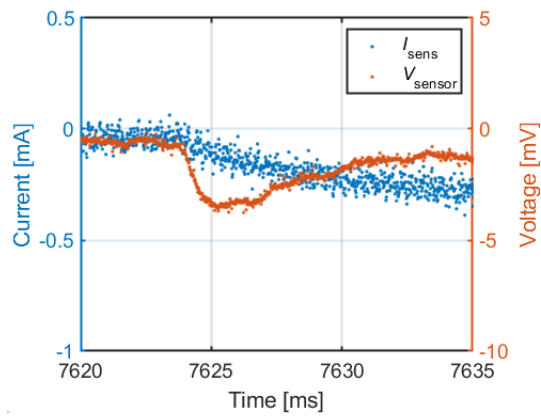
(a) Current in superconducting wire circuit.



(b) Voltage on sensor.



(c) Superposition of current in superconducting wire circuit and voltage on sensor at quench moment.



(d) Zoom at quench moment.

Figure 4.36 – Current detection results on Sample 2 with  $R_3 = 3.3 \Omega$ , when a heat pulse of 5.2 A is applied for 30 ms.

sample was not well compressed, an amount of epoxy resin exists in between the heater strip and superconducting wire, e.g., at locations A, C, E and F.

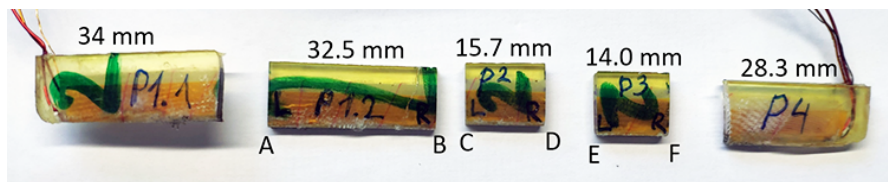


Figure 4.37 – Locations of cutting surfaces of Sample 2.

As the quench first happens in the superconducting wire when it is at the closest location to the heater strip, the smallest value of  $x$  found at surface B is applied in the simulation. After a thickness adjustment due to the material compression, the thicknesses for Kapton, mica

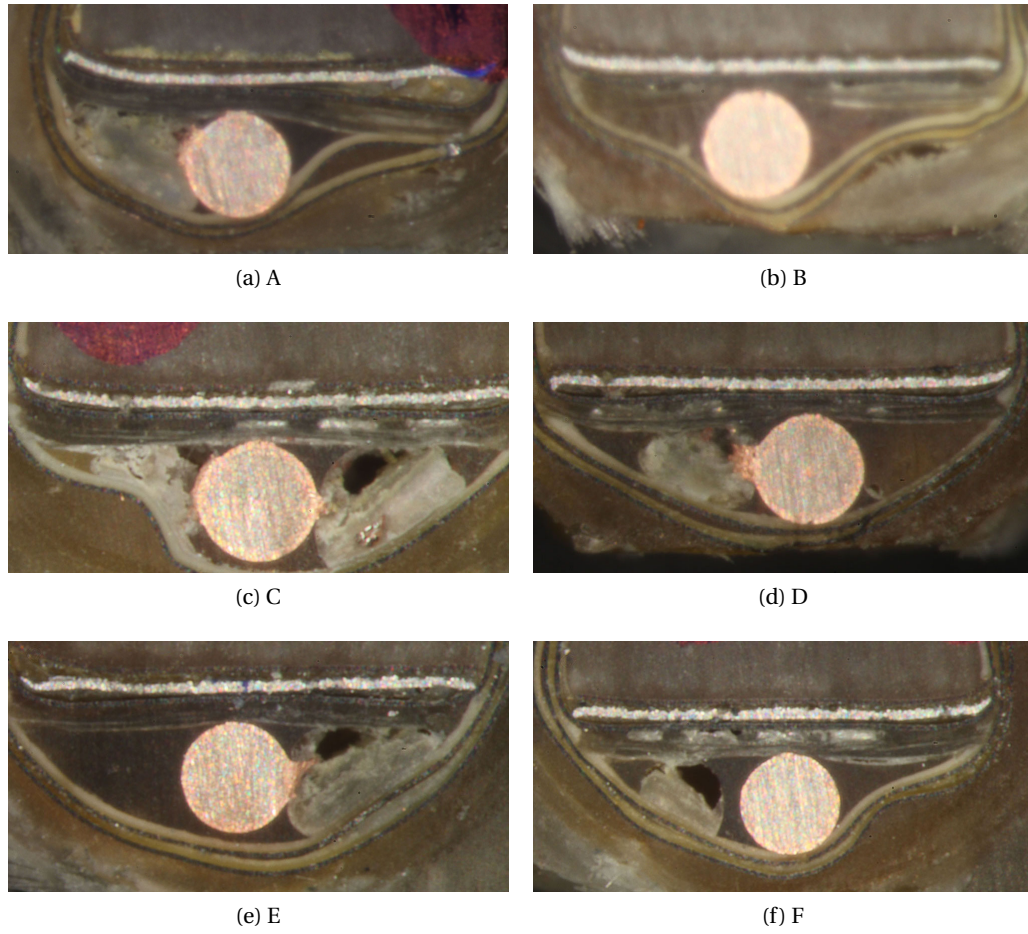


Figure 4.38 – Cutting surfaces of Sample 2 for determination of the distance between the heater strip and the edge of superconducting wire, as well as the transverse thickness of epoxy resin.

Table 4.6 – Measured distances between the heater strip and superconducting wire, and resin thickness on cutting surfaces of Sample 2.

| Distance              | A           | B           | C           | D           | E           | F           |
|-----------------------|-------------|-------------|-------------|-------------|-------------|-------------|
| $x$ [ $\mu\text{m}$ ] | $131 \pm 2$ | $115 \pm 2$ | $141 \pm 2$ | $118 \pm 2$ | $137 \pm 3$ | $170 \pm 2$ |
| $y$ [ $\mu\text{m}$ ] | /           | $28 \pm 3$  | /           | $26 \pm 2$  | /           | /           |

and epoxy resin are respectively  $33 \mu\text{m}$ ,  $54 \mu\text{m}$  and  $28 \mu\text{m}$ . The calculated detection delay time is 9.6 ms from 4 K, compared to a measured value of 17 ms in the experiment. This time difference can be explained by the fact that during the heating period, heat may diffuse longitudinally in the sensing wire from the most heated position towards the less heated portions, thus slowing down the transition.

### Comparison with the voltage-based detection method

The real quench is a growing hot-spot, this needs to be taken into account in the detection delay calculation. In the previous study of quench propagation presented in Table 3.3 for the CD1 model magnet, we found that the time needed to reach a 500 mV threshold for a current level of 15.5 kA is 15 ms for a voltage-based method. In the case of the current-based method, for a temperature margin of 3 K, based on the simulation results in Figure 4.35, a prediction of 3.6 ms is obtained to have a quench on the cross section of the superconducting sensing wire from the initiation of heater pulse.

The minimum propagating zone is very small, only 2-3 mm, for the Nb<sub>3</sub>Sn cables [108, 109]. From the experiments, a measurable signal is obtained for a quench zone of 8 cm in length. Therefore, 6.3 ms is needed for a longitudinal heat propagation in a cable length of 8 cm, at a velocity of 12.7 m/s when the magnet operates at 15.5 kA, using the quench propagation velocity calculated in Table 3.3. This time should also be taken into account in this method. If we sum these two values, the detection time in the current-based method is 9.9 ms, which is slightly shorter than the traditional voltage detection one, i.e., 15 ms to reach the pre-set threshold of 500 mV and 20 ms with the validation time.

As the quench propagation evolves in the conductor, the current drop amplitude should also be significant large in the co-wound circuit. However, 500 mV is set arbitrarily and final comparison is needed when the voltage-spike spectrum of magnet is available. Moreover, in the real high-field magnets, some small fluctuations have the possibility to trigger a spike in the secondary of current derivative sensor, e.g., a nearby power converter or a device shut-down at emergency situations. In this case, some validation time may be necessary.

### Conclusions and discussion

The detection method using a co-wound superconducting sensing wire was studied via both a 2D simulation and a subscale experiment. The purposes are to study its suitability for CCT-type magnets, to compare this current-based method with the traditional voltage-based method.

In the current detection experiment, two types of measurement are used, a direct current signal in the sensing wire and an indirect voltage signal on the current derivative sensor. The advantages and disadvantages of each method are described here.

On one hand, the superconducting wire allows measuring the current directly, without picking much noise in a co-wound loop. With a series resistance, we ensure that a voltage perturbation does not have a large impact on the current measurement. Therefore the direct current drop is a straightforward quench detection method. The direct current measurement allows the introduction of an evaluation time, if needed.

On the other hand, there are some uncertainties and difficulties using the current derivative

sensor to measure an indirect voltage signal. First, the permeability of the current derivative sensor might change during the fabrication process. Second, the sensor picks any possible fluctuations in the environment, causing an unstable signal in the measurement. In the experiment, the voltage peaks are detectable at the moment of the quench. However, the obtained peak amplitude is relatively small (about 10 mV) compared to the threshold used in the voltage-based method, which is 500 mV. The main responsible reason is that, the distance between the heater strip and the sensing wire is not well maintained along the sample causing a slow transverse quench propagation in the sensing wire. Nevertheless, this method is better suited to measure slow transitions as the sensors are sensitive. Moreover, the current derivative sensor should give a larger signal-to-noise ratio for the actual quench than the one in the subscale experiment.

From my experience, the direct current signal in the co-wound superconducting sensing wire is easier to obtain and more reliable than the indirect voltage signal. However, whether it is a direct or indirect measurement, the current-based detection method does not give full immunity from noise.

As mentioned before, the application of the current detection relies on a small and uniform distance between the quenching cable and the superconducting sensing wire along the coil windings in order to have a fast transverse heat propagation from the cable to the wire for the wire to quench, if we want to realize this detection method in a CCT-type magnet. Even though the calculated current-based detection time is shorter than the traditional voltage detection one at the example of CD1 at its nominal operating current, it may still be difficult to achieve the homogeneously small distance throughout an entire magnet. Besides, the thin sensing wire has the possibility to break during the manufacturing of the coil. In this case, we may need technical support from specialized companies to overcome the implementation issues in a full-size magnet. However, the current-based method may be well suited for the protection of busbars in between magnets [41, 42], where the delay times are less critical. Nb-Ti wires could also be used in that case.

### 4.3 Instrumentation of CD1

At LBNL, five CCT model magnets have already been tested in order to reach the design dipole field and to improve the magnet performance [88]. The instrumentation of LBNL's model magnets is briefly described in [34]. LBNL used traditional voltage detection to learn about the quench origin and propagation velocity. A special voltage tap arrangement was made in the multi-layer CCT geometry for measuring quench propagation velocity. In terms of quench protection, LBNL only used a dump resistor to extract the stored magnetic energy [110].

In addition, some diagnostic instrumentation was added to analyze the event during a quench. A spot heater, shown in Figure 4.39a, is able to trigger a quench in a controlled way and, thus, determine the heat propagation speed. An acoustic emission detection system identifies the origin of mechanical events (e.g., crack or friction) by means of triangulation and allows for

studying their "acoustic signature" (a form of the signal) [36].

The polyamide traces were fabricated to make voltage tap connections (Figure 4.39b) and the traces were soldered to flags that were brazed to the cable during heat treatment. Grooves were made in the mandrels along the pole azimuthal locations to accommodate the traces.

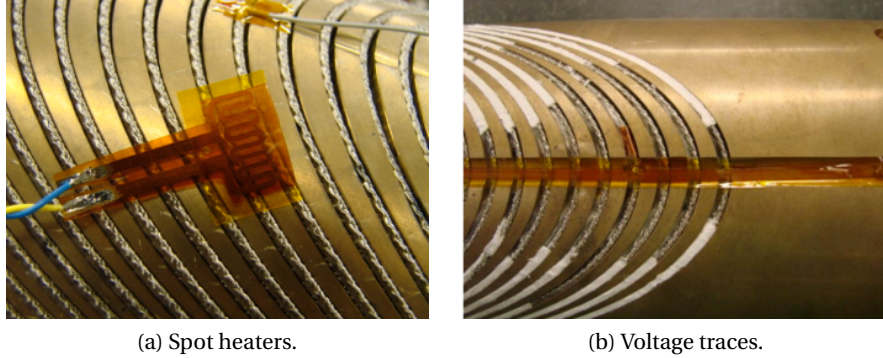


Figure 4.39 – Quench instrumentation of LBNL's model magnets.

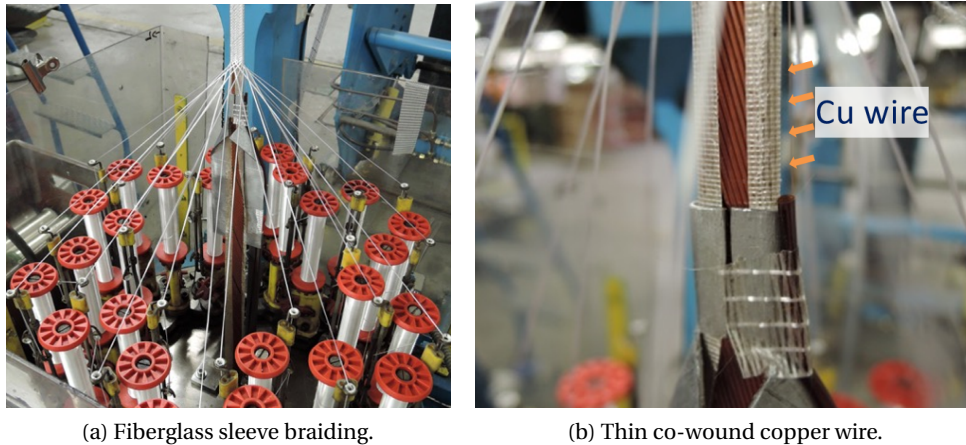
Since our model magnet CD1 was shipped to LBNL for a test at cryogenic temperature, the instrumentation of CD1 was based on that of the LBNL's two-layer model magnets, in particular, CCT4 and CCT5. According to the previously presented protection study results of the two-layer model magnet CD1, described in Chapter 3, the energy extraction and CLIQ system are selected for the magnet test. In addition, a spot heater and several acoustic emission sensors are mounted for diagnostics purposes in the longitudinal direction. On the detection side, we chose to study the feasibility of the voltage-based method with inductive compensation using a co-wound copper wire and optical detection using a co-wound optical fiber.

### 4.3.1 Voltage detection using a co-wound copper wire

In the method of voltage detection with inductive compensation using a co-wound copper wire, a pure voltage rise on the quench resistance is measured, resulting in a smaller voltage threshold and hence a shorter detection time. A company called CGP [111], demonstrated that a copper wire of 0.1 mm in diameter could be co-braided with mica and Rutherford cable, shown in Figure 4.40.

With this co-braided copper wire embedded in the Rutherford cable, a first winding process in the mandrel was carried out. During the process, we found that the braided fiberglass insulation of the cable was weak. Numerous short circuit signals, extremely on the pole regions where the cables are bent at these locations, were observed between superconducting cable and the former. Therefore the cable insulation was improved. The co-braided copper wire, mica sheets and fiberglass insulation were removed. Instead, a thicker fiberglass sleeve was applied. Furthermore, additional fiberglass band was placed on the pole regions. This time, a ceramic-insulated copper wire was placed beneath the insulated cable in the channel





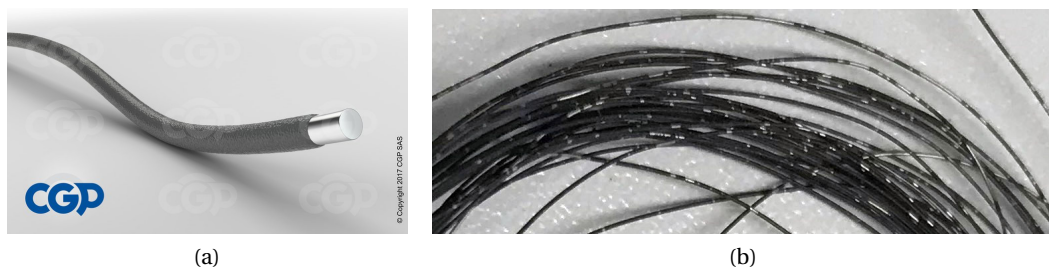
(a) Fiberglass sleeve braiding.

(b) Thin co-wound copper wire.

Figure 4.40 – Insulation braiding with a thin co-wound copper wire.

on the outer layer of CD1.

The wire used was CERAFIL from CGP [112], a ceramic insulation conductor wire for very high temperatures. The wire's nominal operating temperature ranges from  $-90\text{ }^{\circ}\text{C}$  to  $500\text{ }^{\circ}\text{C}$  with a peak temperature of  $1000\text{ }^{\circ}\text{C}$ . According to the thermal characteristics, the wire is able to withstand a temperature of  $800\text{ }^{\circ}\text{C}$  for 240 hours, which is similar to the reaction cycle of the  $\text{Nb}_3\text{Sn}$  superconducting cables. Unfortunately, after the heat treatment of the coil, part of the ceramic insulation of the copper wire peeled off, leading to short circuits to the former. Figure 4.42 shows this wire before and after the heat treatment.



(a)

(b)

Figure 4.41 – Ceramic-insulated copper wire before and after the thermal cycle. (a) Before thermal cycle; (b) Ceramic peeled off after thermal cycle.

In this situation, the co-wound voltage detection could not be tested on the CD1 coil. The traditional voltage taps were prepared and implemented at several locations in the coil for quench detection and localization. Alternative wires with high-temperature insulation systems need to be studied to further investigate this method in order to confirm the wire stability for use in the next CCT-type demonstrator.

### 4.3.2 Optical detection using a co-wound optical fiber

In the method of optical detection using a co-wound optical fiber, the wire was co-wound along the superconducting cable in the channel allowing a distributed sensing approach. During the implementation, placing the fiber on the bottom of the channel prior to the coil-winding, led to fiber breakage after the heat treatment, most likely due to the different thermal expansion coefficients of the metal former and glass fiber. Moreover, the mounting of the fiber atop of the reacted cable was proved to be laborious and unreliable. Therefore additional studies are needed in order to find a reliable method of placing the sensing fibers for the next CCT-type demonstrator.

### 4.3.3 Final configuration

Based on the detection studies outlined in this chapter, the voltage detection using voltage taps, as shown in Figure 4.42a, will be used in the final CD1 instrumentation. Based on the protection studies described in the previous chapter, the energy extraction and CLIQ system of LBNL, presented respectively in Figure 4.42b and 4.42c, will be connected to the finished CD1 magnet assembly, illustrated in Figure 4.43, for the cryogenic test.

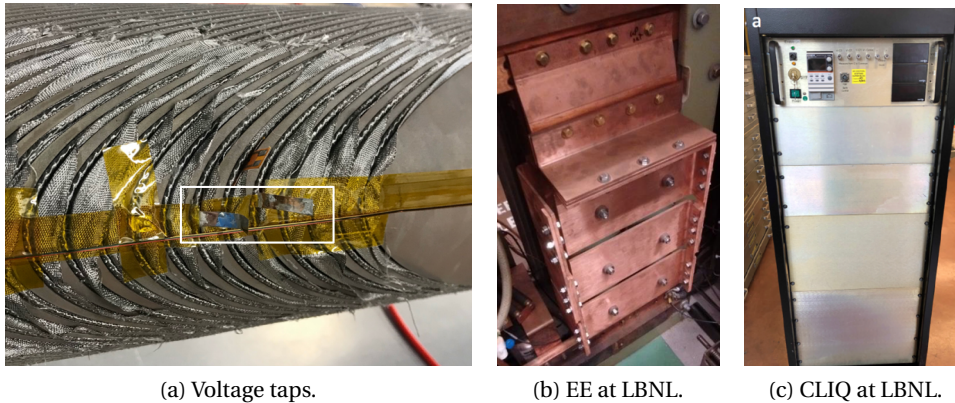


Figure 4.42 – Final CD1 instrumentation.

Due to the time constraint, the test of CD1 model magnet is not foreseen within the time frame of the thesis, thus the data analysis of CD1 test results is not included here.



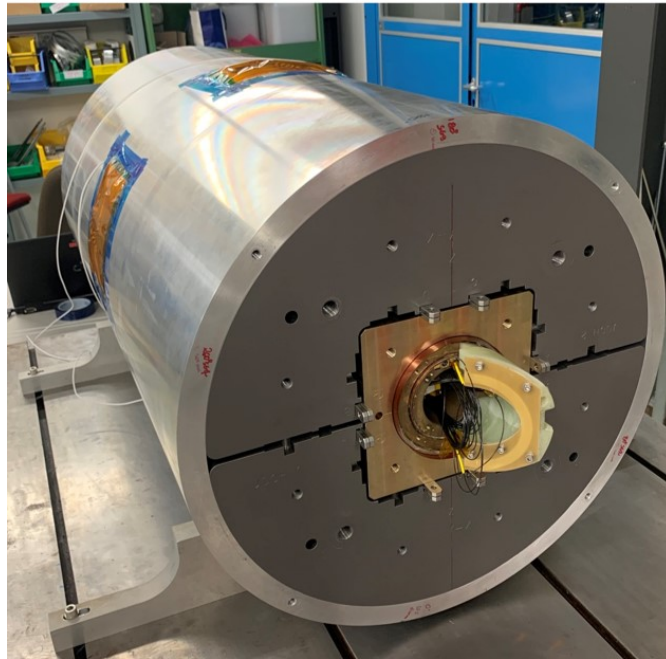


Figure 4.43 – Finished CD1 magnet assembly.



## 5 Conclusion

### 5.1 Summary

The main contribution of PSI to the FCC study is to provide key technologies for the FCC magnet development, including the magnet protection against damage from quench. In this document, I have described the thesis problem: analysis of quench detection and protection of a Nb<sub>3</sub>Sn CCT technology demonstrator dipole for FCC at the example of a two-layer model magnet CD1, built at PSI, and have presented some potential approaches to detect the quench and efficiently protect this kind of magnet.

On the detection side, three methods were studied. The implementation of the voltage detection using a co-wound copper wire and the optical detection using a co-wound optical fiber were tried out on the CD1 model magnet. The encountered difficulties are respectively the wire insulation damage after heat treatment causing short circuits to the former, and the mounting difficulties due to the thin-wire geometry for the optical fiber. The study of the current-based detection method in a subscale experiment allowed us to investigate the key technical issues. The obtained results show that it may be difficult to implement this method throughout an accelerator magnet. Nevertheless, it would be helpful if it is used for the protection of busbars between the magnets.

On the protection side, three methods were studied via simulations. It is proved that CD1 is a protectable magnet with a dump resistor and a voltage-based detection, in a combination of the quench propagation study plus a MITs-based peak-temperature estimate. The co-wound tape study for CD1 tells us that it is worth using this method only if we can reduce the total time before the current discharge, otherwise the hot-spot temperature will be too high, even though it is a more compact magnet.

The performance of the CLIQ unit is evaluated in the CD1 model magnet through a 2D electromagnetic/thermal model, using the thermal and electromagnetic User-Defined Elements. Since the magnet will soon be tested at LBNL, the study was carried out with the CLIQ parameters of the unit which is available at LBNL. In the case of the CD1, the energy-extraction

system will be added in the loop in addition to the installation of the CLIQ unit. In this way, magnet quench protection is guaranteed in different operating conditions. An optimization study of CLIQ parameters is conducted when applying a CLIQ-only protection system for a short and long magnet, i.e., a magnetic length of 0.6 m and 14.3 m respectively, using the CD1 geometry. The different possible combinations of CLIQ parameters, along with the detection requirements are proposed in the thesis. They are proved to be sufficient and efficient to protect the magnet by a CLIQ-only system.

Concerning the simulations, new ANSYS UDEs were adapted and used in the quench simulation of CCT-type magnets. The work with UDEs gave successfully the first-of-a-kind CLIQ simulation on a two-layer CCT-type magnet. The model was partially validated by the test data of CCT4, which was protected by an energy-extraction system. Unfortunately, due to the outbreak of Coronavirus Disease (COVID-19), the model and the automated model generator could not be fully validated as foreseen with measured CLIQ discharges on the CD1 magnet. However, the CD1 test campaign has been prepared through simulations.

### 5.2 Future work

The simulations presented in this thesis laid the ground for the upcoming cold test of PSI's model magnet CD1 at LBNL, in which the quench detection is performed by the traditional voltage taps, the protection by the energy extraction and CLIQ system, along with some additional diagnostics instrumentation, e.g., spot heater and acoustic emission sensors. In the test campaign, CLIQ will be fired first and then the energy extraction will be initiated with a certain delay time. The performance of the CLIQ unit will be evaluated during the cryogenic test of CD1. The test results obtained from CD1 aim to confirm the applicability of an efficient quench protection system in CCT-type high-field magnets for accelerators. With the test results of CD1, the magnet behavior will be compared to the simulation results from the coupled model, described in the thesis, to validate the generic simulation model methods. If some deviations are observed, the model has to be improved based on the current version.

The next step is to study the quench protection in a four-layer FCC CCT magnet based on the findings from the study on a two-layer CCT magnet. The automatic APDL code generator can be used to perform the same kind of numerical simulation study for a four-layer CCT magnet in the accelerator environment without the presence of the energy-extraction system, in order to predict the magnet behavior during a quench. In the next CCT-type demonstrators, the voltage detection using a co-wound copper wire and the optical detection using a co-wound optical fiber will be further investigated. On the protection side, a CLIQ-only protection system will be tested in the next CCT-type magnet prototypes when a powerful CLIQ unit is available. For the quench protection of busbars using the current-based detection method, the study described in the thesis is a good starting point, but the efficiency of this method has to be assessed in an experimental environment with real magnets.

# Bibliography

- [1] The European strategy for particle physics. [Online]. Available: <https://europeanstrategyupdate.web.cern.ch>. Accessed on: Apr. 2020.
- [2] M. Benedikt and F. Zimmermann, "The physics and technology of the Future Circular Collider," in *Nature Reviews Physics*, vol. 1, pp. 238-240, Mar. 2019.
- [3] A. Abada et al., "FCC physics opportunities: Future Circular Collider conceptual design report volume 1," in *The European Physical Journal C*, vol. 79, no. 6, pp. 474-634, July 2019.
- [4] A. Abada et al., "FCC-ee: the lepton collider. Future Circular Collider conceptual design report volume 2," in *The European Physical Journal Special Topics*, vol. 228, no. 2, pp. 261-623, July 2019.
- [5] A. Abada et al., "FCC-hh: the hadron collider. Future Circular Collider conceptual design report volume 3," in *The European Physical Journal Special Topics*, vol. 228, no. 4, pp. 755-1107, July 2019.
- [6] A. Abada et al., "HE-LHC: the high-energy Large Hadron Collider. Future Circular Collider conceptual design report volume 4," in *The European Physical Journal Special Topics*, vol. 228, no. 5, pp. 1109-1382, July 2019.
- [7] Dennis Barak, Beau Harrison and Adam Watts, "Concepts rookie book," Fermilab, accelerator handbook, Sept. 2013. [Online]. Available: <https://beamdocs.fnal.gov/AD/DocDB/0044/004444/002/concepts.pdf>.
- [8] D. Tommasini et al., "The 16 T dipole development program for FCC," in *IEEE Transactions on Applied Superconductivity*, vol. 27, no. 4, pp. 1-5, June 2017, Art no. 4000405.
- [9] D. Schoerling et al., "Considerations on a cost model for high-field dipole arc magnets for FCC," in *IEEE Transactions on Applied Superconductivity*, vol. 27, no. 4, pp. 1-5, June 2017, Art no. 4003105.
- [10] D. Tommasini et al., "Status of the 16 T dipole development program for a Future Hadron Collider," in *IEEE Transactions on Applied Superconductivity*, vol. 28, no. 3, pp. 1-5, Apr. 2018, Art no. 4001305.

## Bibliography

---

- [11] B. Auchmann et al., "Electromechanical design of a 16-T CCT twin-aperture dipole for FCC," in *IEEE Transactions on Applied Superconductivity*, vol. 28, no. 3, pp. 1-5, Apr. 2018, Art no. 4000705.
- [12] S. Prestemon, P. Ferracin and E. Todesco, "Superconducting accelerator magnets. Unit 14: Construction methods and support structures. Episode II," lecture notes at the USPAS - U.S. Particle Accelerator School, Brunswick, NJ, USA, June 2015. [Online]. Available: <https://indico.cern.ch/event/440690>.
- [13] E. Barzi and A. V. Zlobin, "Nb<sub>3</sub>Sn wires and cables for high-field accelerator magnets," in *Nb<sub>3</sub>Sn Accelerator Magnets*, Cham, Switzerland: Springer, 2019, pp. 23-51.
- [14] L. Gamperle, J. Ferradas, C. Barth, B. Bordini, D. Tommasini, and C. Senatore, "Determination of the electromechanical limits of high-performance Nb<sub>3</sub>Sn Rutherford cables under transverse stress from a single-wire experiment," in *Physical Review Research*, vol. 2, p. 013211, Feb. 2020.
- [15] S. Caspi et al., "Canted-Cosine-Theta magnet (CCT) - a concept for high field accelerator magnets," in *IEEE Transactions on Applied Superconductivity*, vol. 24, no. 3, pp. 1-4, June 2014, Art no. 4001804.
- [16] S. Prestemon, P. Ferracin and E. Todesco, "Superconducting accelerator magnets. Unit 10: Electro-magnetic forces and stresses in superconducting accelerator magnets," lecture notes at the USPAS - U.S. Particle Accelerator School, Brunswick, NJ, USA, June 2015. [Online]. Available: <https://indico.cern.ch/event/440690>.
- [17] F. Rodriguez-Mateos and F. Sonnemann, "Quench heater studies for the LHC magnets," in *Proceedings, 2001 Particle Accelerator Conference*, Chicago, IL, USA, June 2001, pp. 3451-3453.
- [18] Z. Charifouline et al., "Overview of the performance of quench heaters for high-current LHC superconducting magnets," in *IEEE Transactions on Applied Superconductivity*, vol. 27, no. 4, pp. 1-5, June 2017, Art no. 4700405.
- [19] S. A. Gourlay, S. O. Prestemon, A. V. Zlobin, L. Cooley and D. Larbalestier, "The U.S. Magnet Development Program plan," strategic document, June 2016. [Online]. Available: <https://www2.lbl.gov/LBL-Programs/atap/MagnetDevelopmentProgramPlan.pdf>.
- [20] S. Prestemon, "The U.S. Magnet Development Program for high field accelerator magnet R&D," presentation at the MT25, Amsterdam, The Netherlands, Aug. 2017. [Online]. Available: <https://indico.cern.ch/event/445667>.
- [21] B. Auchmann et al., "The PSI CCT program overview and motivation," presentation at the PSI CD1 Conceptual Design Review, Geneva, Switzerland, June 2017. [Online]. Available: <https://indico.cern.ch/event/635225>.

- 
- [22] B. Auchmann, J. Gao, R. Felder, G. Montenero, S. Sanfilippo and S. Sidorov, "FCC superconducting-magnet technology developed at PSI," presentation at the GFA Accelerator Seminar, Villigen, Switzerland, Mar. 2018. [Online]. Available: <https://indico.psi.ch/event/6362>.
- [23] G. Montenero et al., "Mechanical structure for the PSI Canted-Cosine-Theta (CCT) magnet program," in *IEEE Transactions on Applied Superconductivity*, vol. 28, no. 3, pp. 1-5, Apr. 2018, Art no. 4002805.
- [24] D. Schoerling, "Technology challenges: Superconducting accelerator magnets. Part I/II," lecture notes at the Summer Student Lecture Programme Course, Geneva, Switzerland, July 2018. [Online]. Available: <https://indico.cern.ch/event/716193>.
- [25] K. H. Mess, "Quench protection," in *CAS - CERN Accelerator School: Superconductivity in Particle Accelerators (CERN-1996-003)*, Hamburg, Germany, May 1995, pp. 143-165.
- [26] L. Bottura, "Cable Stability," in *CAS - CERN Accelerator School: Superconductivity for Accelerators (CERN-2014-005)*, Erice, Italy, Apr. 2013, pp. 401-451.
- [27] P. Ferracin, "Superconducting magnets," lecture notes at the JUAS - Joint Universities Accelerator School, Archamps, France, Feb. 2017. [Online]. Available: <https://indico.cern.ch/event/569714>.
- [28] L. Bottura, "Introduction to accelerator physics. Superconducting magnets," lecture notes at the CAS - CERN Accelerator School, Prague, Czech Republic, Sept. 2014. [Online]. Available: <https://cas.web.cern.ch/sites/cas.web.cern.ch/files/lectures/prague-2014/bottura.pdf>.
- [29] C. Barbagallo, M. Mentink and A.P. Verweij, "Inter-filament coupling currents modeling in superconducting filamentary Nb<sub>3</sub>Sn strands and magnets," CERN EDMS 2337879, 2019. [Online]. Available: <https://edms.cern.ch/document/2337879>.
- [30] M. Marchevsky, "Protection of superconducting magnet circuits," lecture notes at the USPAS - U.S. Particle Accelerator School, Rohnert Park, CA, USA, Jan. 2017. [Online]. Available: [https://uspas.fnal.gov/materials/17UCDavis/MachineProtection/uspas\\_mm.pdf](https://uspas.fnal.gov/materials/17UCDavis/MachineProtection/uspas_mm.pdf).
- [31] F. Scurti, S. Ishmael, G. Flanagan and J. Schwartz, "Quench detection for high temperature superconductor magnets: a novel technique based on Rayleigh-backscattering interrogated optical fibers," in *Superconductor Science and Technology*, vol. 29, no. 3, Jan. 2016.
- [32] F. Scurti and J. Schwartz, "Optical fiber distributed sensing for high temperature superconductor magnets," in *Proceedings, 25th International Conference on Optical Fiber Sensors*, Jeju, Korea, Apr. 2017, pp. 1-4.

## Bibliography

---

- [33] T. Ogitsu et al., "Quench antenna for superconducting particle accelerator magnets," in *IEEE Transactions on Magnetics*, vol. 30, no. 4, pp. 2273-2276, July 1994.
- [34] M. Marchevsky, "Test plan, QA, diagnostics and protection," presentation at the US-MDP CCT Program Review, Berkeley, CA, USA, May 2017. [Online]. Available: <https://conferences.lbl.gov/event/88>.
- [35] M. Marchevsky et al., "Quench performance of HQ01, a 120 mm bore LARP quadrupole for the LHC upgrade," in *IEEE Transactions on Applied Superconductivity*, vol. 22, no. 3, pp. 4702005-4702005, June 2012, Art no. 4702005.
- [36] M. Marchevsky, X. Wang, G. Sabbi and S. Prestemon, "Acoustic detection in superconducting magnets for performance characterization and diagnostics," in *Proceedings, 2013 WAMSDO Workshop on Accelerator Magnet, Superconductor, Design and Optimization*, Geneva, Switzerland, Jan. 2013, pp. 38-42.
- [37] E. Ravaioli, M. Martchevskii, G. Sabbi, T. Shen and K. Zhang, "Quench detection utilizing stray capacitances," in *IEEE Transactions on Applied Superconductivity*, vol. 28, no. 4, pp. 1-5, June 2018, Art no. 4702805.
- [38] E. Ravaioli et al., "A new quench detection method for HTS magnets: stray-capacitance change monitoring," in *Physica Scripta*, vol. 95, no. 1, p. 015002, Dec. 2019.
- [39] E. Ravaioli, V. I. Datskov, C. Giloux, G. Kirby, H. H. J. ten Kate and A. P. Verweij, "New, coupling loss induced, quench protection system for superconducting accelerator magnets," in *IEEE Transactions on Applied Superconductivity*, vol. 24, no. 3, pp. 1-5, June 2014, Art no. 0500905.
- [40] E. Ravaioli, "CLIQ. A new quench protection technology for superconducting magnets," Ph.D. dissertation, Dept. Energy, Materials and Systems, University of Twente, Enschede, The Netherlands, 2015.
- [41] A. V. Dudarev et al., "Quench propagation and detection in the superconducting bus-bars of the ATLAS magnets," in *IEEE Transactions on Applied Superconductivity*, vol. 10, no. 1, pp. 381-384, Mar. 2000.
- [42] A. Dudarev, T. Mulder, W. van de Camp, E. Ravaioli, A. Teixeira and H. H. J. ten Kate, "New fast response thin film-based superconducting quench detectors," in *IEEE Transactions on Applied Superconductivity*, vol. 24, no. 3, pp. 1-4, June 2014, Art no. 8800204.
- [43] V. Marinozzi et al., "Conceptual design of a 16 T  $\cos \theta$  bending dipole for the future circular collider," in *IEEE Transactions on Applied Superconductivity*, vol. 28, no. 3, pp. 1-5, Apr. 2018, Art no. 4004205.
- [44] C. Lorin, M. Segreti and M. Durante, "Design of a Nb<sub>3</sub>Sn 16 T block dipole for the Future Circular Collider," in *IEEE Transactions on Applied Superconductivity*, vol. 28, no. 3, pp. 1-5, Apr. 2018, Art no. 4005005.



- [45] F. Toral, J. Munilla and T. Salmi, "Magnetic and mechanical design of a 16 T common coil dipole for an FCC," in *IEEE Transactions on Applied Superconductivity*, vol. 28, no. 3, pp. 1-5, Apr. 2018, Art no. 4004305.
- [46] T. Salmi, M. Prioli, A. Stenvall and A. P. Verweij, "Quench protection of the 16 T Nb<sub>3</sub>Sn dipole magnets designed for the Future Circular Collider," in *IEEE Transactions on Applied Superconductivity*, vol. 29, no. 5, pp. 1-5, Aug. 2019, Art no. 4700905.
- [47] M. Prioli et al., "The CLIQ quench protection system applied to the 16 T FCC-hh dipole magnets," in *IEEE Transactions on Applied Superconductivity*, vol. 29, no. 8, pp. 1-9, Dec. 2019, Art no. 4703209.
- [48] M. Prioli, B. Auchmann, L. Bortot, M. Maciejewski, T. Salmi and A. Verweij, "Conceptual design of the FCC-hh dipole circuits with integrated CLIQ protection system," in *IEEE Transactions on Applied Superconductivity*, vol. 29, no. 8, pp. 1-9, Dec. 2019, Art no. 4703309.
- [49] EuroCirCol: European Circular Energy-Frontier Collider Study. [Online]. Available: <http://www.eurocircol.eu>. Accessed on: Apr. 2020.
- [50] European union's H2020 Framework Programme. [Online]. Available: <https://ec.europa.eu/programmes/horizon2020>. Accessed on: Apr. 2020.
- [51] G. Ambrosio, "Maximum allowable temperature during quench in Nb<sub>3</sub>Sn accelerator magnets," in *Proceedings, 2013 WAMSDO Workshop on Accelerator Magnet, Superconductor, Design and Optimization*, Geneva, Switzerland, Jan. 2013, pp. 43-46.
- [52] T. Salmi et al., "Quench protection analysis integrated in the design of dipoles for the Future Circular Collider," in *Physical Review Accelerators and Beams*, vol. 20, p. 032401, Mar. 2017.
- [53] ANSYS Inc. [Online]. Available: <http://www.ansys.com>. Accessed on: Apr. 2020.
- [54] L. Brouwer, D. Arbelaez, S. Caspi, M. Marchevsky and S. Prestemon, "Improved modeling of Canted-Cosine-Theta magnets," in *IEEE Transactions on Applied Superconductivity*, vol. 28, no. 3, pp. 1-6, Apr. 2018, Art no. 4001006.
- [55] L. Brouwer, D. Arbelaez, B. Auchmann, L. Bortot and E. Stubberud, "User defined elements in ANSYS for 2D multiphysics modeling of superconducting magnets," in *Superconductor Science and Technology*, vol. 32, no. 9, p. 095011, Aug. 2019.
- [56] COMSOL Multiphysics. [Online]. Available: <https://www.comsol.com>. Accessed on: Apr. 2020.
- [57] ROXIE: a computer code for the integrated design of accelerator magnets. [Online]. Available: <https://cern.ch/roxie>. Accessed on: Apr. 2020.

## Bibliography

---

- [58] Thea. [Online]. Available: <https://supermagnet.sourceforge.io/thea.html>. Accessed on: Apr. 2020.
- [59] LEDET. [Online]. Available: [https://espace.cern.ch/steam/\\_layouts/15/start.aspx#/LEDET](https://espace.cern.ch/steam/_layouts/15/start.aspx#/LEDET). Accessed on: Apr. 2020.
- [60] MATLAB. [Online]. Available: <https://www.mathworks.com/>. Accessed on: Apr. 2020.
- [61] S. Caspi et al., "Calculating quench propagation with ANSYS," in *IEEE Transactions on Applied Superconductivity*, vol. 13, no. 2, pp. 1714-1717, June 2003.
- [62] R. Yamada, S. W. Kim, A. Lee, R. Wands, J. M. Rey and M. Wake, "Quenches and resulting thermal and mechanical effects on epoxy impregnated Nb<sub>3</sub>Sn high field magnets," in *Proceedings, 2001 Particle Accelerator Conference*, Chicago, IL, USA, June 2001, pp. 3424-3426.
- [63] R. Yamada, E. Marscin, A. Lee, M. Wake and J. M. Rey, "2-D/3-D quench simulation using ANSYS for epoxy impregnated Nb<sub>3</sub>Sn high field magnets," in *IEEE Transactions on Applied Superconductivity*, vol. 13, no. 2, pp. 1696-1699, June 2003.
- [64] R. Yamada, E. Marscin, A. Lee and M. Wake, "3D ANSYS quench simulation of cosine theta Nb<sub>3</sub>Sn high field dipole magnets," in *IEEE Transactions on Applied Superconductivity*, vol. 14, no. 2, pp. 291-294, June 2004.
- [65] L. Brouwer, "Canted-Cosine-Theta superconducting accelerator magnets for high energy physics and ion beam cancer therapy," Ph.D. dissertation, Dept. Nuclear Engineering, University of California, Berkeley, CA, USA, 2015.
- [66] Wolfram Mathematica. [Online]. Available: <https://www.wolfram.com/mathematica>. Accessed on: Apr. 2020.
- [67] B. J. Maddock and G. B. James, "Protection and stabilisation of large superconducting coils," in *Proceedings of the Institution of Electrical Engineers*, vol. 115, no. 4, pp. 543-547, Apr. 1968.
- [68] G. Manfreda, "Review of ROXIE's material properties database for quench simulation," CERN, TE-MSD internal note 2011-24, Dec. 2011.
- [69] The WP5 contributors, "16 T dipole design options: input parameters and evaluation criteria," EuroCirCol, technical report, EuroCirCol-P1-WP5, June 2016.
- [70] M. Turqueti, private communication, 2019.
- [71] E. Ravaioli et al., "Towards an optimized Coupling-loss Induced Quench protection system (CLIQ) for quadrupole magnets," in *Physics Procedia*, vol. 67, pp. 215-220, 2015.
- [72] L. Rossi and M. Sorbi, "MATPRO: a computer library of material property at cryogenic temperature," University of Milan and INFN, technical report, CARE-NOTE-2005-018-HHH, Apr. 2005.

- 
- [73] NIST: National Institute of Standards and Technology. [Online]. Available: <https://www.nist.gov>. Accessed on: Apr. 2020.
- [74] CUDI. [Online]. Available: <http://cern-verweij.web.cern.ch>. Accessed on: Apr. 2020.
- [75] CryoComp. Eckels Engineering. [Online]. Available: <http://www.eckelsengineering.com>. Accessed on: Apr. 2020.
- [76] J. E. Jensen, R. B. Stewart, W. A. Tuttle, H. Brechna and A. G. Prodell, *Bubble Chamber Group: selected cryogenic data notebook*. Upton, NY, USA: Brookhaven National Laboratory, 1980. [Online]. Available: <https://www.bnl.gov/magnets/Staff/Gupta/cryogenic-data-handbook>.
- [77] P. Bauer, H. Rajainmaki and E. Salpietro, "EFDA material data compilation for superconductor simulation," EFDA, technical report, Apr. 2007.
- [78] J. Ferradas, L. Gamperle, C. Barth, and C. Senatore, "Electromechanical characterization of Nb<sub>3</sub>Sn conductors at University of Geneva," presentation at the Workshop on Nb<sub>3</sub>Sn technology for accelerator magnets, Paris, France, Oct. 2018. [Online]. Available: <https://conferences.lbl.gov/event/88>.
- [79] L. T. Summers, M. W. Guinan, J. R. Miller and P. A. Hahn, "A model for the prediction of Nb<sub>3</sub>Sn critical current as a function of field, temperature, strain, and radiation damage," in *IEEE Transactions on Magnetics*, vol. 27, no. 2, pp. 2041-2044, Mar. 1991.
- [80] A. Verweij, "QP3, users manual," CERN EDMS 1150045, 2011. [Online]. Available: [https://edms.cern.ch/ui/file/1150045/1/Manual\\_QP3.pdf](https://edms.cern.ch/ui/file/1150045/1/Manual_QP3.pdf).
- [81] Opera. [Online]. Available: <https://www.3ds.com/products-services/simulia/products/opera>. Accessed on: Apr. 2020.
- [82] G. H. Morgan, "Theoretical behavior of twisted multicore superconducting wire in a time-varying uniform magnetic field," in *Journal of Applied Physics*, vol. 41, no. 9, pp. 3673-3679, 1970.
- [83] M. N. Wilson, *Superconducting Magnets*. Oxford, UK: Oxford University Press, 1987.
- [84] E. Ravaioli, B. Auchmann, M. Maciejewski, H. H. J. ten Kate and A. P. Verweij, "Lumped-element dynamic electro-thermal model of a superconducting magnet," in *Cryogenics*, vol. 80, pp. 346-356, Dec. 2016.
- [85] L. Bortot et al., "A 2-D finite-element model for electrothermal transients in accelerator magnets," in *IEEE Transactions on Magnetics*, vol. 54, no. 3, pp. 1-4, Mar. 2018, Art no. 7000404.
- [86] L. Brouwer, "CCT magnet development at LBNL," presentation at the MDP-FCC-EuroCirCol coordination meeting 03, Geneva, Switzerland, Apr. 2017. [Online]. Available: <https://indico.cern.ch/event/616977>.

## Bibliography

---

- [87] S. Prestemon, "Status update from LBNL," presentation at the MDP-FCC-EuroCirCol coordination meeting 06, Geneva, Switzerland, Dec. 2018. [Online]. Available: <https://indico.cern.ch/event/776591>.
- [88] S. Prestemon, "CCT magnet development: results and next steps," presentation at the International Meeting on High Field Accelerator Magnet, Gaithersburg, MD, USA, Dec. 2019. [Online]. Available: <https://conferences.lbl.gov/event/264>.
- [89] J. Gao, B. Auchmann, L. Brouwer, A. Pautz and S. Sanfilippo, "Modeling of quench protection concepts for Canted-Cosine-Theta type high-field magnets," in *IEEE Transactions on Applied Superconductivity*, vol. 30, no. 4, pp. 1-5, June 2020, Art no. 4701505.
- [90] S. Prestemon, P. Ferracin and E. Todesco, "Superconducting accelerator magnets. Unit 6: Flux jumps and motion in superconductors," lecture notes at the USPAS - U.S. Particle Accelerator School, Brunswick, NJ, USA, June 2015. [Online]. Available: <https://indico.cern.ch/event/440690>.
- [91] R. Denz et al., "Quench detection and diagnostic systems for the superconducting circuits for the HL-LHC," in *Proceedings, 10th International Particle Accelerator Conference (IPAC'19)*, Melbourne, Australia, May 2019, pp. 4183-4186.
- [92] V. Marinozzi, "Quench protection and design of high-field superconducting accelerator magnets: the role of dynamic effects on the differential inductance," Ph.D. dissertation, Dept. Physics, University of Milan, Milan, Italy, 2017.
- [93] A. K. Ghosh, M. Garber, K. E. Robins and W. B. Sampson, "Training in test samples of superconducting cables for accelerator magnets," in *IEEE Transactions on Magnetics*, vol. 25, no. 2, pp. 1831-1834, Mar. 1989.
- [94] W.V. Hassenzahl, "Study of the effects of copper to superconductor ratio on stability," in *Cryogenics*, vol. 29, no. 6, pp. 637-641, June 1989.
- [95] Supercon Inc. [Online]. Available: <http://www.supercon-wire.com>. Accessed on: Apr. 2020.
- [96] Sumitomo Heavy Industries. [Online]. Available: <https://www.shi.co.jp>. Accessed on: Apr. 2020.
- [97] Lake Shore Cryotronics. [Online]. Available: <https://www.lakeshore.com>. Accessed on: Apr. 2020.
- [98] R. Wesche and A. M. Fuchs, "Design of superconducting current leads," in *Cryogenics*, vol. 34, no. 2, pp. 145-154, 1994.
- [99] N. Peray, "Nb<sub>3</sub>Sn vs Nb-Ti," presentation at the EN-MME-EDS Extended Section Meeting, Geneva, Switzerland, Mar. 2017. [Online]. Available: <https://indico.cern.ch/event/624538>.

- 
- [100] L. Rossi, "Superconducting cable and magnets for the Large Hadron Collider," CERN, LHC project report 694, Mar. 2004.
- [101] D. Larbalestier, A. Gurevich, D. Feldmann and A. Polyanskii, "High Tc superconducting materials for electric power applications," in *Nature*, vol. 414, pp. 368-377, 2001.
- [102] L. A. Hall, *Survey of Electrical Resistivity. Measurements on 16 Pure Metals In the Temperature Range 0 to 273 K*. Washington, DC, USA: U.S. Government Publishing Office, 1968. [Online]. Available: <https://nvlpubs.nist.gov/nistpubs/Legacy/TN/nbstechnicalnote365.pdf>.
- [103] Crydom. [Online]. Available: <http://www.crydom.com>. Accessed on: Apr. 2020.
- [104] A. Brem, B. Gold, T. Tervoort, B. Auchmann and D. Tommasini, "Epoxy systems for the impregnation of high-field superconducting magnets," presentation at the CERN TE-MSM Magnet Seminar, Geneva, Switzerland, Oct. 2019. [Online]. Available: <https://indico.cern.ch/event/856041>.
- [105] E. De Matteis, D. Calcoen, R. Denz, A. Siemko, J. Steckert and M. B. Storkensen, "New method for magnet protection systems based on a direct current derivative sensor," in *IEEE Transactions on Applied Superconductivity*, vol. 28, no. 3, pp. 1-5, Apr. 2018, Art no. 4700505.
- [106] Magnetic Shield Corporation. [Online]. Available: <http://www.magnetic-shield.com>. Accessed on: Apr. 2020.
- [107] National Instruments. [Online]. Available: <https://www.ni.com>. Accessed on: Apr. 2020.
- [108] M. Bonura and C. Senatore, "Thermal conductivity of industrial Nb<sub>3</sub>Sn wires fabricated by various techniques," in *IEEE Transactions on Applied Superconductivity*, vol. 23, no. 3, p. 6000404, June 2013, Art no. 6000404.
- [109] W. M. de Rapper, "Thermal stability of Nb<sub>3</sub>Sn Rutherford cables for accelerator magnets," Ph.D. dissertation, Dept. Energy, Materials and Systems, University of Twente, Enschede, The Netherlands, 2014.
- [110] M. Marchevsky et al., "CCT5 Test Results," presentation at the US-MDP Third Collaboration Meeting, Batavia, IL, USA, Jan. 2019. [Online]. Available: <https://indico.fnal.gov/event/18806>.
- [111] CGP: Cables for Global Performance. [Online]. Available: <http://www.cables-cgp.com>. Accessed on: Apr. 2020.
- [112] CERAFIL miniature ceramic wires for very high temperatures. [Online]. Available: <http://www.cables-cgp.com/en/categories/fils-electriques-miniature-haute-temperature-ceramique>. Accessed on: Apr. 2020.



# A Appendix

## A.1 Circuit coupling technical details

There are several different commands to couple or uncouple the voltage degrees of freedom between nodes in ANSYS APDL for controlling the circuit behavior.

- To build the electric connection by coupling the nodes:

CE defines a constraint equation relating degrees of freedom on selected nodes.

CP defines a set of coupled degrees of freedom on selected nodes. It is a simple way to enforce constraint equations and is equivalent to using "CE". Both "CE" and "CP" relate the degree of freedom between nodes. Usually, they force the degree of freedom to be the same, but not necessarily a specific value.

D defines degree-of-freedom constraints on selected nodes. It forces the degree of freedom of the selected nodes to be a specific value.

- To break the electric connection by uncoupling the nodes:

CPDELE deletes coupled degree of freedom sets with the numbers of the set defined by "CP".

DDELE deletes degree-of-freedom constraints with the node number.

In principle, a circular usage of "CP" always causes issues in ANSYS. If one wants to couple the degree of freedom for a group of nodes, it is recommended to do it for all of them at once, instead of using several commands to link them. For example, one should use "CP,NEXT,VOLT,N1,N2,N3" rather than "CP,NEXT,VOLT,N1,N2" then "CP,NEXT,VOLT,N2,N3" because ANSYS reports this as an error. Besides, if one wants to couple a node, which has a constraint "D" placed on it, with other nodes using "CP". This node must be first in the list. For example, one should write "CP,NEXT,VOLT,N3,N1,N2" and "D,N3,VOLT,0".

To avoid any unexpected errors in ANSYS, we decide to couple the most right nodes with "D" and force them to have  $V = 0$  for a consistent way of modeling. In this way, we only ground one location of the circuit. For the rest part of the circuits, "CP" and "CE" are used.

### A.2 Coupled model generation steps

There are several steps to build a coupled electromagnetic-thermal quench model:

- Generate 2D coil cross-section geometry with the appropriate spatial discretization.
- Generate the mechanical structure and a large air background for electromagnetic analysis.
- Build an electromagnetic model:
  - Define material properties, electromagnetic elements, and corresponding key options.
  - Set cable parameters.
  - Set a real constant for each conductor section with its own data (e.g., FEA area, physical length).
  - Set up an electrical circuit:
    - \* Define circuit elements and corresponding key options.
    - \* Set circuit parameters and real constants.
    - \* Create circuit. A normal electric element is placed between two nodes in the circuit. In addition to that, an FEA circuit coupled element has to be connected in a node in the FEA domain.
    - \* Couple the degrees of freedom for each conductor piece (e.g., electromotive force drop, current).
  - Define outer boundary conditions and couple all coincident nodes in z-vector magnetic potentials within a tolerance.
- Build a thermal model:
  - Define material properties, thermal elements, and corresponding key options.
  - Duplicate thermal areas from the electromagnetic model.



### A.3. Peak temperature estimation with EE for different voltage thresholds

- The real constants of the conductor are mapped from electromagnetic to thermal elements with a constant shift when the key option of "transfer with EMAG/Thermal" is activated.
- Couple all coincident nodes in temperatures within a tolerance.
- Define interfaces for load transfer between EM and TH fields.
- Define MFS settings for two fields.
- Solve problem.

### A.3 Peak temperature estimation with EE for different voltage thresholds

In Subsection 3.2.3, we investigated the peak temperature in the CD1 coil after a quench through a MITTs adiabatic calculation for a voltage threshold of 500 mV at different current levels. Here the cases for three different thresholds, i.e., 100, 250 and 500 mV, are studied to provide further insights on these quantities. Table A.1 shows the time needed to reach the pre-set voltage threshold  $\Delta t_{\text{thres}}$  while Table A.2 presents the peak temperature after a quench, when the magnet is protected by a dump resistor of 40 m $\Omega$ . It is worth noting that the total detection time is still computed as  $t_d = \Delta t_{\text{thres}} + \Delta t_{\text{switch}}$ , where  $t_{\text{switch}} = 5$  ms. Nevertheless, one can add the necessary validation time. By using the last column of temperature increase rate in Table A.2, the corresponding temperature increase due to this additional time can be added to the value listed in Table A.2 for obtaining a final peak temperature estimation.

Table A.1 – Time needed to reach different voltage thresholds  $\Delta t_{\text{thres}}$  for CD1.

| $\Delta t_{\text{thres}}$ [ms] | $V_{\text{thres}} = 100$ mV | $V_{\text{thres}} = 250$ mV | $V_{\text{thres}} = 500$ mV |
|--------------------------------|-----------------------------|-----------------------------|-----------------------------|
| I = 16.3 kA                    | 6.0                         | 10.2                        | 13.5                        |
| I = 15.5 kA                    | 7.2                         | 11.6                        | 15.0                        |
| I = 10.8 kA                    | 26.6                        | 38.0                        | 48.7                        |

Table A.2 – CD1 peak temperature estimation after a quench, when the magnet is protected by a dump resistor of 40 m $\Omega$ , for different voltage thresholds.

| $\Delta t_{\text{thres}}$ [ms] | $V_{\text{thres}} = 100$ mV | $V_{\text{thres}} = 250$ mV | $V_{\text{thres}} = 500$ mV | $\Delta T/\text{ms}$ [K/ms] |
|--------------------------------|-----------------------------|-----------------------------|-----------------------------|-----------------------------|
| I = 16.3 kA                    | 201                         | 260                         | 316                         | 14-17                       |
| I = 15.5 kA                    | 180                         | 231                         | 278                         | 12-14                       |
| I = 10.8 kA                    | 108                         | 147                         | 197                         | 3-5                         |



## B Glossary

**Accelerator:** Device used to produce high-energy beams of charged particles such as electrons, protons, or heavy ions for research in high-energy and nuclear physics, synchrotron radiation research, medical therapies, and some industrial applications.

**AI:** Analog Input of the data acquisition system.

**APDL:** ANSYS Parametric Design Language, a scripting language to build models and analyses in terms of parameters.

**CCT:** Canted-Cosine-Theta. A CCT-type magnet superposes fields of nested and tilted solenoids that are oppositely canted. The current distribution of a canted layer generates a pure dipole field as well as a solenoid field that can be canceled with an oppositely canted layer.

**CCT4:** The fourth CCT-type model magnet constructed at LBNL.

**CD:** Canted Dipole. Name of the model magnets at PSI.

**CERN:** European Organization for Nuclear Research.

**CLIQ:** Coupling-Loss Induced Quench. Once a quench is detected, the CLIQ system starts working by inducing current oscillations in the coil, resulting in a change in the local magnetic field, which introduces high inter-filament and inter-strand coupling losses (IFCLs and ISCLs). Hence the varying magnetic field heats a large portion of the coil.

**Collider:** Particle accelerator to accelerate charged particles to collisions of them.

**Critical surface:** Critical surface is the boundary between the superconducting state and normal state in the current density  $J$ , magnetic field  $B$ , temperature  $T$  space.

**CryoComp:** The software is a collection of properties for a lot of materials commonly present in superconducting magnets.

## Appendix B. Glossary

---

**CUDI:** The software computes some material properties useful for quench simulation for Rutherford cable modeling.

**DAQ:** Data acquisition system.

**Dipole:** A magnet with a north and south pole, typically used to bend or steer a beam.

**EE:** Energy extraction. A system to extract the stored magnetic energy on an external dump resistor.

**EPFL:** École Polytechnique Fédérale de Lausanne.

**EuroCirCol:** European Commission funded European Circular.

**FCC:** Future Circular Collider.

**FEA:** Finite Element Analysis.

**FEM:** Finite Element Method.

**Fermilab:** Fermi National Accelerator Laboratory.

**G10:** A fiberglass laminate. It is created by stacking multiple layers of glass cloth, soaking in epoxy resin, and compressing the resulting material under heat until the epoxy cures. G10 is the toughest of the glass fiber resin laminates and therefore the most commonly used.

**Heat treatment:** Reaction process to form  $\text{Nb}_3\text{Sn}$  phase.

**HL-LHC:** High-Luminosity LHC. It is an upgrade of the LHC to achieve a high luminosity of a factor of five times larger than the LHC nominal value.

**Hot-spot temperature:** Hottest spot after a quench in a superconducting coil.

**HTS:** High-Temperature Superconductors. Temperature here refers to the temperature below which the superconductor must be cooled for it to become superconducting; for HTS superconductors that temperature is usually well above 30 K.

**IFCC:** Inter-Filament Coupling Current. Two parallel superconducting filaments in the metallic matrix form large loops with large currents.

**IFCL:** Inter-Filament Coupling Losses. Losses due to IFCC.

**ISCC:** Inter-Strand Coupling Current. Two parallel superconducting strands in the metallic matrix form large loops with large currents.

**ISCL:** Inter-Strand Coupling Losses. Losses due to ISCC.

**LBNL:** Lawrence Berkeley National Laboratory.

---

**LHC:** Large Hadron Collider. It is the world's largest and most powerful particle collider, most complex experimental facility ever built, and the largest single machine in the world.

**Load line:** It shows the peak magnetic field on the windings versus the current in the magnet.

**LTS:** Low-Temperature Superconductors. It typically refers to Nb-based alloys (most commonly Nb-Ti) and A15 (Nb<sub>3</sub>Sn and Nb<sub>3</sub>Al) superconductors. Temperature here refers to the temperature below which the superconductor must be cooled for it to become superconducting; for LTS superconductors that temperature is usually well below 30 K.

**Luminosity:** The quantity that measures the ability of a particle accelerator to produce the required number of interactions.

**Magnets:** Devices that produce magnetic fields that are applied to charged particles to bend, focus, or correct the trajectory.

**Magnet training:** Typical process in which a progressive improvement of the reached field level is observed after a series of repeated quenching events.

**MATPRO:** A computer library of material property at cryogenic temperature.

**Mica:** A lightweight material that offers high thermal resistance. Thin mica sheets allow for rapid heat transfer and heating element cooling.

**MIITs:** M (Mega) I (current) I (current) T (time) s (plural). This term is used to link a current profile during a quench (from the current plateau or ramp after a quench initiation to the end of the current decay) to a peak temperature for a given cable type under adiabatic conditions

**MPZ:** The minimum propagating zone MPZ is the minimum zone that produces enough heat at a given current, magnetic field and cooling condition.

**MQE:** The minimum quench energy MQE is the amount of energy needed to put into a given zone over a given time interval at a given temperature, magnetic field, and current to produce thermal runaway.

**Nb<sub>3</sub>Sn:** Niobium-tin is a metallic chemical compound of niobium (Nb) and tin (Sn), used as a superconductor. It remains superconducting up to a magnetic flux density of 30 T, compared to a limit of roughly 15 T for Nb-Ti.

**Nb-Ti:** An alloy of niobium and titanium, used industrially as a type II superconductor wire for superconducting magnets.

**NCSU:** North Carolina State University.

**NIST:** National Institute of Standard and Technology. Its official website contains a database of cryogenic material properties.

**Opera:** Opera electromagnetic FEA simulation software.

## Appendix B. Glossary

---

**PSI:** Paul Scherrer Institut.

**Quadrupole:** A four-pole magnet used to focus beams.

**Quench:** Quench is the sudden transition from the superconducting to the normal-conducting state.

**Quench protection:** Protection of the superconducting magnet in case of a quench.

**QPS:** Quench protection system.

**Ramping:** A process in which the magnetic field changes over some time.

**RRR:** Residual Resistivity Ratio.

**Rutherford cable:** A Rutherford cable is a type of superconducting electrical cable used to generate magnetic fields in particle accelerators. The cable is named after the Rutherford Laboratory where the cable design was developed.

**SS:** Short Sample. It is considered as the perfect magnet's physical performance limit.

**Strand:** Composite wire containing superconducting filaments dispersed in a matrix.

**Superconductor:** An element, inter-metallic alloy, or compound that will conduct electricity without resistance below a certain temperature.

**Thermal cycle:** Temperature cycling between room temperature (293 K) and cryogenic temperature (4.2 K or 1.9 K).

**Twin-aperture magnet:** A magnet housing two apertures in the same yoke.

**UDE:** User Defined Element. One of ANSYS capabilities to write user's elements.

**US-MDP:** US Magnet Development Program.

# Jiani Gao

19.09.1992, Chinese nationality

## Contact

jiani.gao@icloud.com

## Languages

English ★★★★★☆  
French ★★★★★☆  
German ★★☆☆☆  
Japanese ★★☆☆☆  
Chinese ★★★★★

## Education

- 01.2017 - 07.2020 **PhD of Energy** EPFL, Switzerland
- 09.2014 - 09.2016 **Master of Engineering Sciences** Grenoble INP - Phelma, France  
Engineer's degree, rank top 25% in graduating year.
- 09.2013 - 06.2014 **Bachelor of Engineering Sciences** Grenoble INP - Phelma, France  
Rank top 25% in a grade of 379.
- 09.2011 - 06.2013 **DUT of Electrical Engineering & Industrial Informatics** Université d'Artois, France  
Undergraduate technical degree, rank 3<sup>rd</sup> in a class of 36.

## Work experience

- 12.2016 - 07.2020 **Doctoral student at Paul Scherrer Institut** Villigen, Switzerland  
Analysis of quench detection and protection of a Nb<sub>3</sub>Sn CCT technology demonstrator dipole for FCC - a project of CERN, in collaboration with LBNL.
- 03.2016 - 08.2016 **Nuclear engineer at Texas A&M University** (Internship) College Station, TX, USA  
Implementation and validation of a time-dependent thermal conduction module within Texas A&M's code PDT.
- 05.2015 - 08.2015 **Nuclear engineer at AREVA NP** (Internship) Paris la Défense, France  
Benchmark study between AREVA's new calculation chain ARCADIA and the present official one SCIENCE.

## Publications

### Reviewed articles

- J. Gao, B. Auchmann, L. Brouwer, A. Pautz and S. Sanfilippo, "Modeling of quench protection concepts for Canted-Cosine-Theta type high-field magnets," in *IEEE Transactions on Applied Superconductivity*, vol. 30, no. 4, pp. 1-5, June 2020, Art no. 4701505.
- B. Auchmann, L. Brouwer, S. Caspi, J. Gao, G. Montenero, M. Negrazus, G. Rolando and S. Sanfilippo, "Electromechanical design of a 16-T CCT twin-aperture dipole for FCC," in *IEEE Transactions on Applied Superconductivity*, vol. 28, no. 3, pp. 1-5, Apr. 2018, Art no. 4000705.
- A. Abada *et al.*, "FCC physics opportunities: Future Circular Collider conceptual design report volume 1," in *The European Physical Journal C*, vol. 79, no. 6, pp. 474-634, July 2019.
- A. Abada *et al.*, "FCC-ee: the lepton collider. Future Circular Collider conceptual design report volume 2," in *The European Physical Journal Special Topics*, vol. 228, no. 2, pp. 261-623, July 2019.
- A. Abada *et al.*, "FCC-hh: the hadron collider. Future Circular Collider conceptual design report volume 3," in *The European Physical Journal Special Topics*, vol. 228, no. 4, pp. 755-1107, July 2019.
- A. Abada *et al.*, "HE-LHC: the high-energy Large Hadron Collider. Future Circular Collider conceptual design report volume 4," in *The European Physical Journal Special Topics*, vol. 228, no. 5, pp. 1109-1382, July 2019.